# SOLAR RACKING FOR THE SPARTAN SUPERWAY: AN AUTOMATED TRANSIT NETWORK

A Project Report

Presented to

The Faculty of the Department of Mechanical Engineering

San José State University

In Partial Fulfillment

of the Requirements for the Degree

Master of Science

by

Sumeet Shastri

December 2020

The Designated Project Committee Approves the Project Report Titled

SOLAR RACKING FOR AN AUTOMATED TRANSIT NETWORK: THE
SPARTAN SUPERWAY

by

Sumeet Shastri

APPROVED FOR THE DEPARTMENT OF MECHANICAL ENGINEERING

SAN JOSÉ STATE UNIVERSITY

December 2020

| | |
|---|---|
| Burford Furman, Ph.D. | Department of Mechanical Engineering |
| Raymond Yee, Ph.D. | Department of Mechanical Engineering |
| Ron Swenson | INIST & Swenson Solar |

## ABSTRACT

A structure to mount photovoltaic (PV) modules onto the guideway of the automated transit network (ATN) Spartan Superway has been proposed. The design's foundation consists of trussing adapted to accommodate a canopy slope of 15 degrees. Brackets designed to interface with the bottom chord of the trusses secure the canopy onto the guideway along with diagonal bracing. Z-purlin profiles attached atop the trussing provide an interface to mount 6 framed solar panels. C-clamps customized to secure framed modules to the upper surface of the purlin efficiently secure PV panels onto the racking. Wire management is conducted through a closed channel with a profile adopted from an existing racking solution and is mounted onto holes along the purlin's channel. Rainwater harvesting is facilitated by a gutter attached to the trussing at the lower edge of the array.

Existing solar racking for rooftop, carport, and ground arrays were explored to understand the fundamental geometries and mechanisms employed in structures with proven viability. Elements considered adaptable for a canopy to be mounted on an elevated ATN were distinguished including Z-purlins, C-clamps, and mounting brackets. Trussing schemes used in roofing supports and footbridges were studied to create a profile for the canopy that would reliably endure wind loading, which will impart the most critical loads on the modules and support structure. Design wind pressures were calculated in accordance with procedures specified by ASCE.

These pressures were used to simulate wind loading on the canopy to assess its structural integrity and to determine reactions imparted onto the guideway. Resultant pressures from CFD simulations were compared with ASCE's pressure value for two reasons: to ensure that appropriate forces were being accounted for and geometrical approximations made to use ASCE's procedure were reasonable. Static simulations with the pressures corresponding to a range of wind speeds from 20 to 150mph and a worst case pressure of 55 psf were conducted to assess the design's behavior and whether it met a prescribed factor of safety of 2 against yield. Simulation results indicate that a majority of the members' lengths meet this factor of safety, but high stresses present at the connection points mean modifications to the current sizing of steel angle sections used to construct the trusses is required to meet the factor of safety of two for the 55psf loading case.

TABLE OF CONTENTS

# LIST OF TABLES

# LIST OF FIGURES

# LIST OF SYMBOLS AND ABBREVIATIONS

| Symbol | Units | Description |
|---|---|---|
| ° | degrees | Unit of measurement for angles |
| °C | Celsius | Unit of measurement for temperature |
| $C_f$ | none | Force coefficient used in ASCE calculation |
| $G$ | none | Gust effect factor used in ASCE calculation |
| $ft^2$ | Square feet | Unit of measurement for area |
| $F_x$ | Pounds | Reaction force in the x-direction |
| $F_y$ | Pounds | Reaction force in the y-direction |
| $GC_{rn}$ | none | Net pressure coefficient |
| $(GC_{rn})_{nom}$ | none | Nominal net pressure coefficient |
| $h$ | feet | Mean roof height of building or other structure used in ASCE calculation |
| $h_1$ | feet | Height of solar panel above roof at lower edge of panel |
| $h_2$ | feet | Height of solar panel above roof at upper edge of panel |
| $h_{pt}$ | feet | Mean parapet height used in ASCE calculation |
| $I$ | none | Importance factor used in ASCE calculation |
| '' | inches | Dimensions in inches |
| $K_d$ | none | Wind Directionality factor used in ASCE calculation |
| $K_z$ | none | Velocity pressure coefficient at a height z used in ASCE calculation |
| $K_{zt}$ | none | Topographical factor used in ASCE calculation |
| $L_p$ | inches/feet | Panel chord length used in ASCE calculation |
| $M_x$ | lb.ft | Reaction moment at a certain location $x$ |
| $p$ | Pounds/sq. ft. | Total wind pressure from ASCE calculation |
| $q_h$ | Pounds/sq. ft. | Velocity pressure used in ASCE calculation |
| $V$ | mph | velocity |
| $z$ | inches or feet | Elevation of various structures used in ASCE calculation |
| $\sigma$ | Psf or $\dfrac{N}{m^2}$ | Symbol for mechanical stress |

| Abbreviation | Full Spelling |
|---|---|
| ASCE | American Society of Civil Engineers |
| ATN | Automated Transit Network |
| CAD | Computer-aided design |
| Ft. | Feet |
| GPa | Gigapascal |
| In. | Inches |
| lbs | Pounds |
| m | Meters |
| MPa | Megapascal |
| $\dfrac{N}{m^2}$ | Newtons/square meter |
| psf | Pounds per square foot |
| PV | Photovoltaic |

## 1. INTRODUCTION

Automated Transit Networks (ATN) are emerging as an efficient means of transportation throughout the world. These systems utilize automated vehicles suspended from a network of elevated guideways to provide transportation on demand to individuals or small groups (Fabian et al., 2014). A majority of current ATNs are powered by utility electric grids. However, previous research has shown that ATNs can feasibly be powered using solar arrays even at extreme locations such as Anchorage, Alaska (Furman, 2016). The Spartan Superway, a network under development to connect the North and South campuses of San Jose State University and the Tamein Caltrain/Light Rail stations, aims to be fully powered by solar energy as shown in Figure 1.

Previous studies estimate that a two to three-meter-wide photovoltaic canopy above the guideway could power daily operation of the network for a conservative average of 1,440 passengers per hour (Furman, 2016). The implementation of a solar array on the Superway requires a reliable and streamlined racking structure to mount photovoltaic panels. Most existing racking structures are customized for installations on rooftops, carports, and other similar structures. These applications are less constrained than the racking required for the Superway, which has specific space, aesthetic, and installation requirements. The racking needs to install in a minimalist fashion on the multi-mile stretch of the Superway's guideway. Studies on critical factors such as loading, modeling, and material choice combined with concepts from existing designs for rooftop and ground-mounted arrays were used to design practical mounting customized for the Spartan Superway.
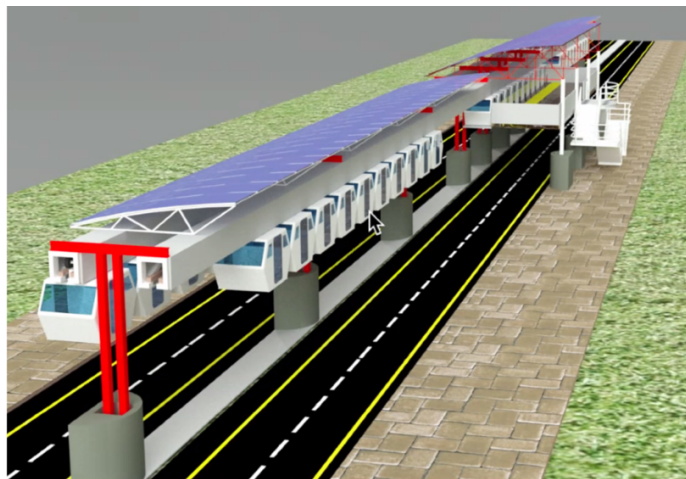


**Figure 1: A Rendering of the Solar Canopy for the Spartan Superway.** This rendering ideated by Futran shows a canopy supported by a straight section of two guideways (Spartan Superway, from (Futran, n.d.)).

## 2. OBJECTIVES

The objective of this project is to design, create a CAD documentation set, and perform loading simulations on a reliable solar racking structure for the Spartan Superway. The racking will need

to withstand wind loads, secure panels using a streamlined approach, install in a minimalistic yet secure manner to the guideway, and provide accessibility for maintenance.

## 3. METHODOLOGY

Racking was designed for a designated straight segment of the guideway. Key parameters to be satisfied by the design were identified first. The solar canopy would need to be installable on the guideway before elevation onto vertical supports to follow the installation sequence of existing monorails such as HBAHN21, which fully assembled its guideways before elevation (Hbahn, 2020). Furthermore, the racking would need to be modular to facilitate efficient transport of components to the installation site where a majority of assembly could occur. Trussing profiles used in roofs, bridges, and other structures were adapted into the mounting to create a reliable foundation to hold the solar canopy. Members used in ground-mounted and rooftop racking with proven dependability were also implemented in the design. In terms of durability, solar mounting needs to reliably resist wind loads, which impart significant loadings onto the modules and their support system. Design wind loads were calculated in accordance with procedures specified by ASCE for rooftop arrays. These loads were verified with CFD simulations to ensure that approximations made were reasonable, followed by static simulations on the structure to assess its viability under critical loads and determine whether a factor of safety against yield of two was satisfied.

## 4. LITERATURE REVIEW

Existing designs, design guides, and previous studies pertaining to solar mounting were consulted to develop solar racking for the Superway. This information has been classified into the subsequent sections concerning design, wind loading, and simulation.

### 4.1 Design

A guide on steel construction for the United Kingdom specified the design principles employed in various trussing profiles. The arrangement of members in triangular patterns helps stabilize the truss. Warren or Modified Warren trusses, which solely use diagonals or a combination of diagonals with vertical supports as pictured in Figure 2, are commonly used trussing arrangements in structures such as bridges ("Design of Steel Footbridges," n.d.). Circular or rectangular hollow sections welded together at joints are used to construct the trussing profile. Stiff joints are achieved by keeping bracing members the same width as the chord member. Upper and lower chords intersect the diagonals of the truss where possible. The guide clarifies that although joints in trusses are hardly pinned in reality, design standards encourage this assumption for analysis. Members are typically verified for axial loads only ("Trusses," n.d.). Racking designed for the Spartan Superway incorporates a Warren truss to form a reliable foundation to support the upper components of the solar canopy. A Warren truss is considered a starting point for the canopy's trussing; if additional stiffness or support is needed, alternate profiles with more members such as a Pratt truss will be incorporated instead.
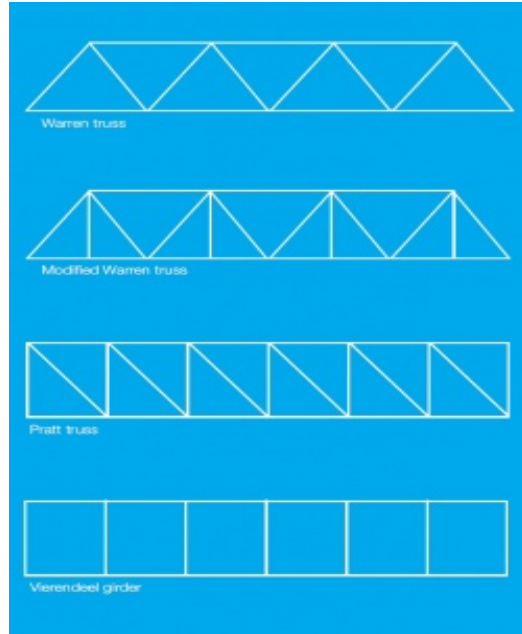
**Figure 2. Commonly used Trussing Profiles.** Several geometries of trussing are used in different structures. The most basic of these arrangements is the Warren Truss (first) with room for added verticals as in the Modified Warren Truss (second) (Types of Truss and Vierendeel Girder, from ("Design of Steel Footbridges", n.d.)).

Polygonal top chords were incorporated in the trusses of bridges with Warren trusses to extend the span length as shown in Figure 3 (Griggs, 2015). Using this adaptation, a polygonal upper chord is used to incrementally slope each PV module to accomplish the overall canopy slope of fifteen degrees while also providing a stiff foundation for the canopy.



**Figure 3. Polygonal Upper Chord.** A polygonal upper chord on a Warren Truss with verticals used on a railroad bridge over the Verdigris River, Oklahoma (Steel Bridge for BNSF Railroad, from (Griggs, 2015)).

Truss bridge information from the North Carolina Department of Transportation confirms that modifications to the upper chord of the truss to make it polygonal are possible by showing adaptations used in truss bridges as seen in Figure 4. The article also specifies that diagonals of a Warren truss act in tension or compression ("Truss Bridges," 2019). The ability to withstand tension and compression is crucial for members that form solar mounting for the Spartan Superway since wind loading from above and on the underside can impart a combination of these loads onto the canopy.
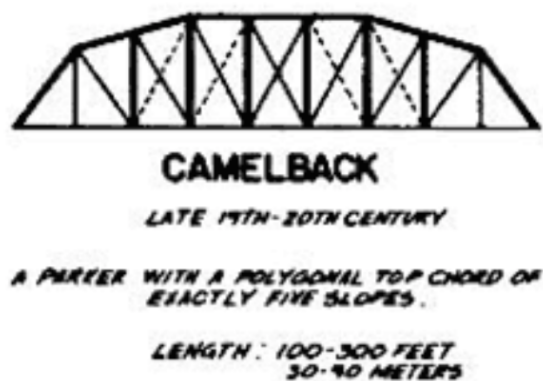


**Figure 4. Confirmation of A Polygonal Upper Chord.** Profiles of truss bridges incorporate a polygonal upper chord that is considered applicable to the upper chord of the Superway's canopy (Camelback Truss, from ("Truss Bridges," 2019)).

A design manual on trussing for single-story steel buildings based on Eurocode 3 detailed several considerations for truss design. These guidelines specified that diagonal members should be inclined between 35 and 55 degrees relative to the upper or lower chords. In addition, point loads should be applied at the nodes. Next, the orientation of diagonals should be such that the longest members are subject to tension and shorter members are subject to compression. Furthermore, lateral stability is needed at both the top and bottom chords to prevent buckling out of the plane of the truss. The upper chord of trusses used in roofing are stabilized by purlins that run normal to plane of the trussing. Adding members normal to the plane of the truss at the bottom chord can help utilize corresponding verticals on either side for stability as shown in Figure 4. This acts similar in manner to a longitudinal wind girder, which use chords formed from two lines of purlins in small buildings ("Steel Buildings in Europe", 2008). These guidelines were incorporated into the mounting designed for the Superway within the dimensions and sloping specified for the canopy.
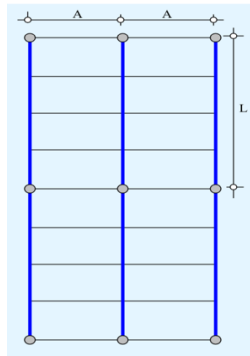
**Figure 5. Secondary Trussing.** An arrangement of secondary trussing in between primary trussing segments shown in blue (Secondary Trussing Arrangement, from ("Steel Buildings in Europe", 2008)). A similar scheme was incorporated for members added for lateral stability at the bottom chord of the solar mounting.

The Federal Highway Administration of the U.S. Department of Transportation postulates that gusset plates can provide an efficient means to connect the members of a truss at a joint. Vertical, diagonal, and cross members are directly connected to the plate allowing for modularity as shown in Figure 6. Gusset plates can also be used stack trusses on top of each other (Federal Highway Administration, 2018). Gusset plates provide an alternative to welding the members of the trussing designed for the solar racking. This would facilitate the assembly of various components of the racking at the installation site, eliminating the need for pre-welded parts.
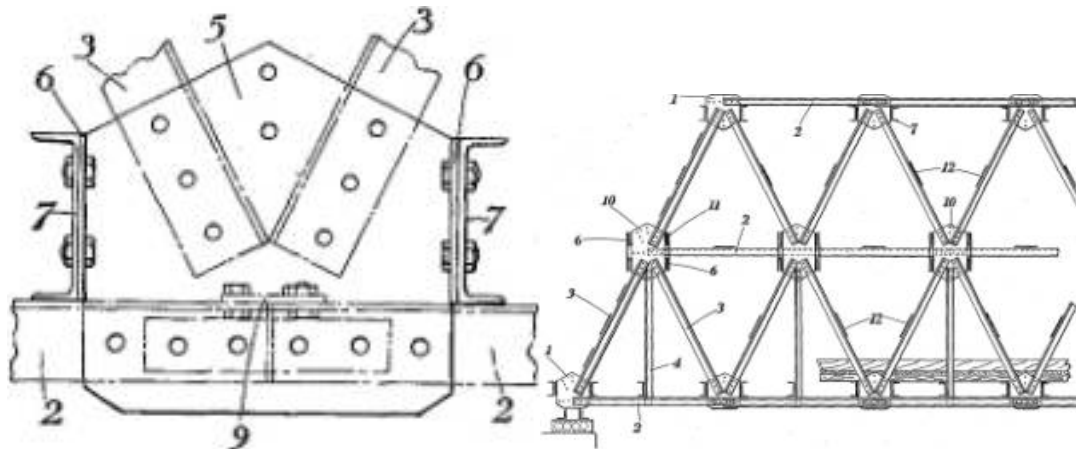


**Figure 6. Gusset Plates used at Truss Joints.** Prefabricated plates can be used bolt the members of a truss together. These plates can also be used to stack units of the truss on top of each other (Gusset Plates, from (Federal Highway Administration, 2018)).

EnergySage, a company specialized in the installation of solar arrays throughout the United States, specifies the sizes, weights, and dimensions of residential and commercial solar panels. Residential solar panels are roughly 65" x 39" x 2," and commercial solar panels are roughly 78"x 39"x 2". An additional 12 cells in commercial solar panels account for their additional

length; these panels weigh about 50lbs total (Matasci, 2018). Commercial panels are considered the most appropriate for the Superway's canopy; these specifications were used to ensure the mounting is designed to accommodate commercial modules.

HBAHN21, a monorail similar to the Spartan Superway in Dortmund, Germany, clarifies the installation sequence used in its construction. Fully equipped beams (guideways) are mounted onto the vertical support columns in the last step of the installation ("HBAHN21", 2020). For the Spartan Superway, this means that the solar canopy will ideally need to be installed onto the ribs or other structures on the guideway before elevation onto the columns. This necessitates a streamlined interface between the racking and the designated mounting surface on the guideway; the connection needs to securely hold the racking but allow for ease of installation. Hardware that satisfies these criteria are needed to create this interface. Furthermore, the HBAHN's cabin dimensions were used to determine an approximate dimension for spacing of ribs employed in this monorail as shown in Figure 7. The spacing of ribs on the guideway is an important parameter in ensuring the racking is dimensioned to be mountable.



Cabin Length: 8.232m (excludes coupling)
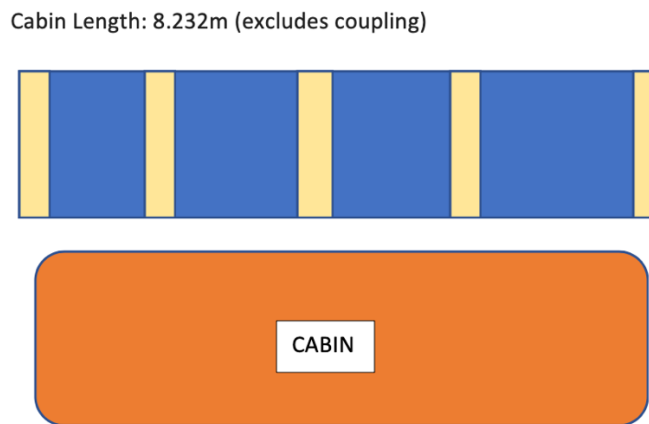
CABIN

8.232 / 4 = 2.058m = 6.751 ft ; Approximate spacing between ribs on HBAHN guideway

**Figure 7. Rib Spacing on Existing Guideway.** An approximation of the rib spacing used on the HBAHN guideway in Germany was determined using cabin dimensions from the system's technical data webpage.

Genmounts describes the dimensions, components, and installation instructions for its post driven solar racking for ground mounted arrays. This design consists of Z-purlin bolted to the upper surface of a slanted girder, which is mounted on a vertical post driven into the ground as seen in Figure 8. Panels are affixed to the purlin using two types of top-down compression clamps depending on whether the module is at an edge or middle of the structure. Wire management is accomplished through pre-punched holes at regular intervals along the Z-purlin as seen in Figure 9 with cable ties to secure the wires to the channel of the purlin (Genmounts, n.d.). An analogous arrangement of Z-purlin secured to upper surface of the trussing foundation is used in the Superway's racking design. The purlins provide for simple installation of modules without compromising sturdiness. Additionally, a similar means of wire management will be incorporated in the canopy design since the addition of extra bulk is avoided by this method.
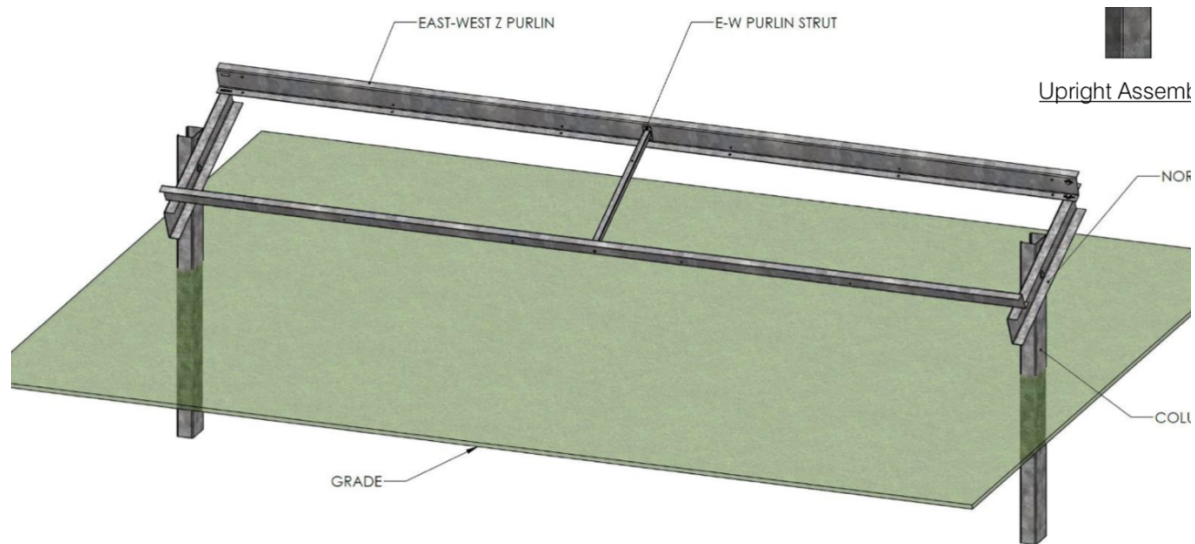
**Figure 8. Z-Purlin Racking from Genmounts**. An arrangement of vertical posts, side supports, and Z-purlins is shown for a ground mounted racking design from Genmounts (Vector 1.0 Post Driven Ground Mount Racking System, from (Genmounts, n.d)).
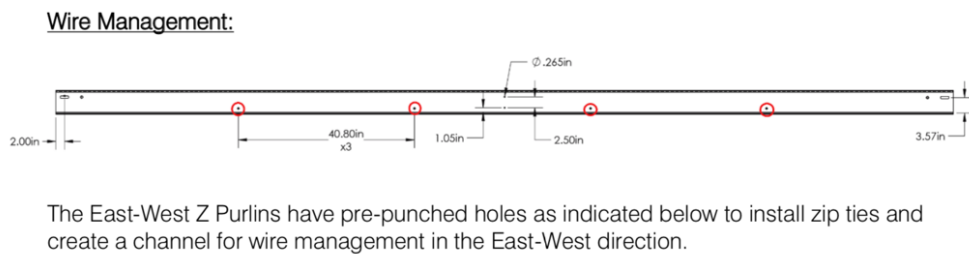


**Figure 9. Wire Management Method.** An arrangement of pre-punched holes on the Z-purlin channel to route wires using cable ties is shown from the Genmounts ground mounted racking design (Vector 1.0 Post Driven Ground Mount Racking System, from (Genmounts, n.d.)).

Powers Solar Frames describes a patented purlin that eliminates additional hardware typically required to mount modules on a purlin. The purlin has a channel along its face that allows for framed solar panels to slide in as shown in Figure 10 (Powers Solar Frames, 2020). Although initially considered in-line with the goal of streamlined panel installation for the Superway's canopy, careful consideration revealed that maintenance of out-of-service panels would be difficult with a slide-in mechanism since removal of all panels adjacent to the target module would be required. The emphasized the efficiency of using Z-purlin in the design.
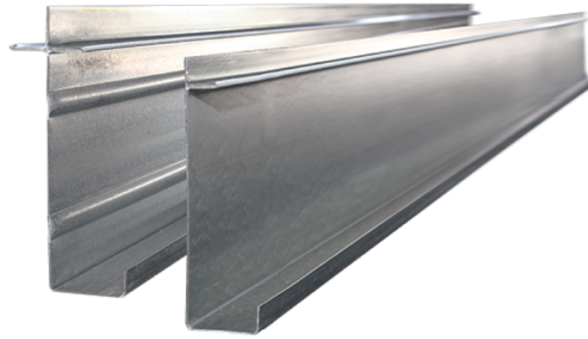
**Figure 10. Slide-In Mounting Purlin.** This patented purlin allows for framed solar panels to be installed by sliding in the modules (Super Purlin, from (Powers Solar Frames, 2020)). Although efficient in terms of panel installation, these purlins were not implemented in the design because they do not facilitate efficient maintenance of individual panels.

Mechatron elaborates on efficient panel installation achievable through its product PV-CLAMP, which has been used in several installations conducted by the company throughout Europe. These clamps mimic the behavior of a C-clamp but have been modified to secure the frame of a solar panel to a C or Z profile purlin as shown in Figure 11. Four clamps are required for each module and efficiently secure panels to mounting; these specific clamps or other similar products provide a reliable means of securing panels to Z-purlins on the Superway's canopy (Mechatron, 2020).
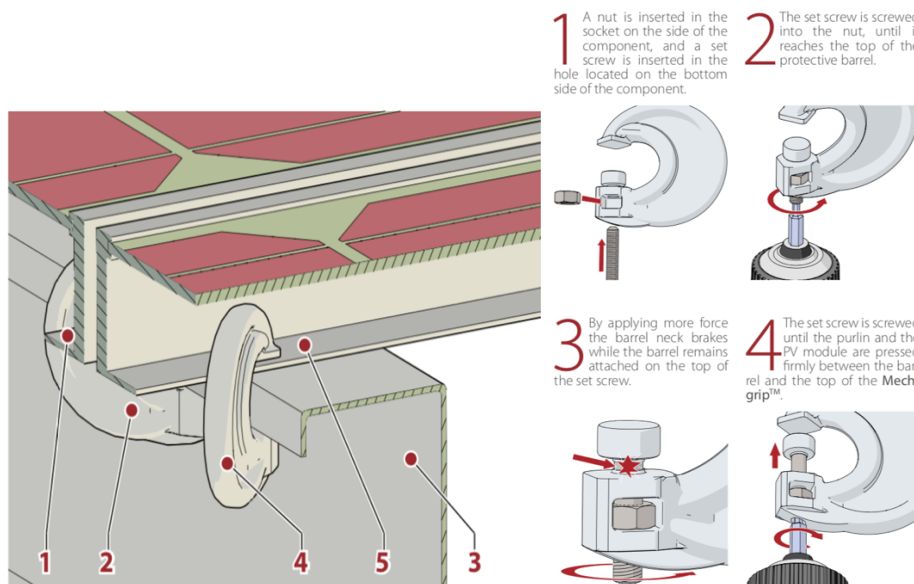


**Figure 11. Clamps to Secure Modules.** C-clamps secure the frame of a module to the purlin using a set screw that holds the two frames together (PV-CLAMP, from (Mechatron, 2020)).

A racking for elevated photovoltaic applications patented by Nitzko et al. is intended for modules elevated above ground level and pictured in Figure 12. The design employs a vertical support which holds up a grooved inclined member. The groove serves two purposes: as a bolting site for a U-shaped bracket that connects it to the vertical support and as an attachment site for modules. Each member has stable, torsion resistant cross sections that can be manufactured through processes such as rolling, drawing, and bending. An adaptation of the U-

shaped bracket from this design is correspondingly used in the Superway's mounting to secure the racking to supporting structures on the guideway.
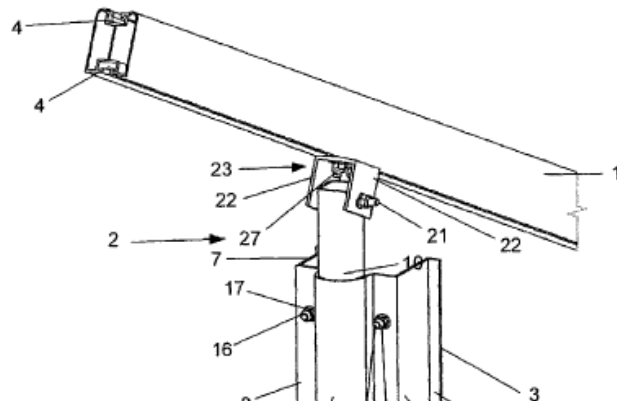


**Figure 12. Elevated PV Racking Solution.** Patented elevated photovoltaic racking structure with U-bracket connection (System for Mounting an Elevated Solar Installation, from (Nitzko, 2011))

Quest Renewables manufactures solar canopies for carports that satisfy a number of the challenges posed by the Superway's installation site. The company claims that 90% of assembly is at ground level and that the canopy design is modular (Quest Renewables, 2018). Inspection of photos of this canopy reveals that a key contributor to the design's modularity is the use of C-purlin, which is mounted in perpendicular arrangements at the top of the mounting to create a frame for the panels to rest on, indicated by the orange arrows in Figure 13. Channeled purlins are therefore considered a key cross-section to be used in the design of the Superway's canopy.



**Figure 13: An underside view of Quest Renewables' QuadPod Long Span Canopy design.** Elements of this design can potentially be customized for the Superway since it satisfies a number of the installation challenges present (QuadPod Long Span Canopy, from (Quest Renewables, 2018))

Perfection Architectural Systems, LLC describes various types of canopy profiles that can be manufactured; a shape that best strikes a balance between function and aesthetics can be selected. Flat canopies, trellises, carports, and inclined frames are among several profiles offered by the company. These options can be customized to run along straight or curved sections. The understructure can be selected from a variety of profiles including flat, curved, or slanted sections. The flexibility of Perfection Architectural's solar canopy profiles depends largely on having independent verticals supporting the upper canopy, which is shown throughout the company's website. Although the Superway's canopy will be mounted directly onto the guideways, concepts from Perfection Architectural System's design such as accommodation of curves through the gradual angling of supports as shown in Figure 14 below are considered applicable to the Superway's canopy. The canopy can potentially be mounted to accommodate a similar curved path by gradually slanting units of the trussing base. A curved understructure could accomplish the required sloping.



**Figure 14. Profiles from Perfection Architectural Systems.** A curved section of a flat canopy from Perfection Architectural Systems, LLC that could be used as a model to curve the Superway's canopy on the left and a curved understructure is shown on the right (Flat Canopy and Solar Framing, from (Perfection Architectural Systems, 2013)).

Messenger and Ventre (2003) specify several important considerations to account for in the design of a solar mounting system. Structural members need to be selected and sized so that maximum stresses are well below material limits; a minimum factor of safety of two for all components is recommended. Steel is recommended over aluminum to construct the support structure since steel has a well-defined fatigue limit of half its tensile strength. Aluminum's fatigue limit is vaguely defined as a stress level for which the material can handle a high number of cycles. More specifically, low-carbon steel is typically used to construct solar mounting components.  A minimum gap of 0.25in. (6.4mm) between panels is recommended. Dead loads are considered to act uniformly over the mounting structure and are usually expressed in units of pounds per square foot (psf). Other forces to take into account are the weight of array installation and maintenance people, seismic effects, and forces due to rain, wind, and ice. Messenger and Ventre then emphasize that among these forces, aerodynamic wind loading presents the most concern (Messenger & Ventre, 2003). Therefore, for the Superway's racking design, mechanical

behavior under a range of wind loads were carefully analyzed to ensure the design could safely withstand these forces and maintain the recommended factor of safety of two at the highest wind speed.

Cano et al. postulated a relationship between soiling losses from dust accumulation on PV modules with their tilt angle. The first module in the Superway's canopy is angled at five degrees; each subsequent module increases in slope by two degrees for the remaining five panels for a total slope of 15 degrees. In the tilt angle range of 5 to 15 degrees, soiling losses are about 1.17% as seen in Figure 15 below (Cano et al., 2014). This soiling loss is considered minimal and can be further reduced by a panel cleaning strategy.
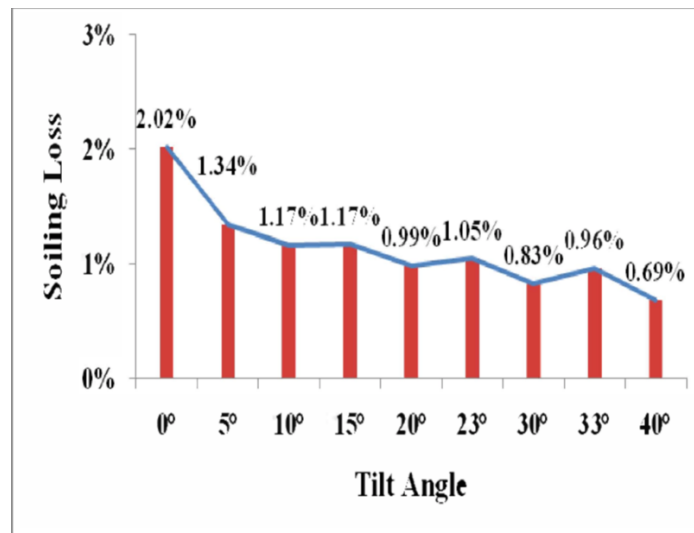


**Figure 15. Soiling losses vs. Tilt Angle.** The soiling loss for the 5-15 degree slope of the Superway's PV modules would be about 1.17% (Average Soiling Losses for each tilt angle for first three months of 2011, from (Cano et al, 2014)).


### 4.1.1 Design using Single Angle Struts

Woolcock et al. specifies that trusses constructed of single angle members can be constructed in two different arrangements: one where the angle members are all face the same direction and the other where the angle members alternate on opposite sides of the truss. In tests on trusses made of angle members, the dominant direction of deflection was perpendicular to the plane of each member. To reduce eccentricity and these out-of-plane deflections, it is recommended that web members of single angle trusses be connected on one side of the truss instead of the alternating arrangement. The single-side arrangement was found to have a higher theoretical capacity than the alternating arrangement (Woolcock et al., 1986). To ensure the reliability of the trussing designed for the Superway's canopy, the same side arrangement of the members will be employed.
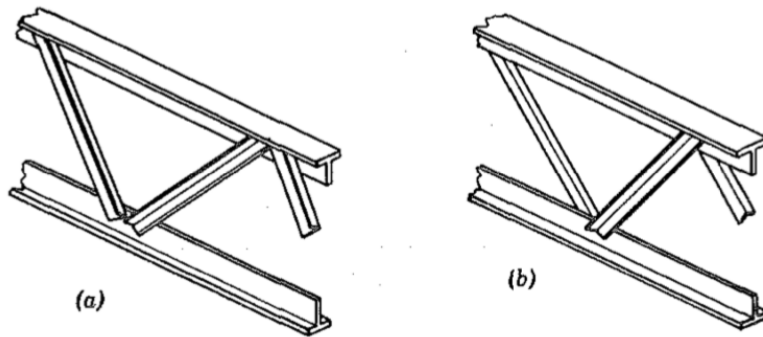
FIG. 1.—Web Members on Trusses: (*a*) Same Sides; (*b*) Opposite Sides

Figure XX. Two Arrangements of Single Angle Members. The single-side arrangement shown in (a) has more capacity since eccentric loads are minimized. The single-sided arrangement was therefore selected for the Superway's canopy.

Fong et al. confirms that the strength of trusses constructed with web members on one side of the truss could take considerably greater load than trusses with members connected on opposite sides. Furthermore, experiments found that the failure loads of specimens with double bolted end connections is 16.7% to 25.4% higher than those with single bolted end connections. The load resistance with double bolted connections were also found to be 8.7% to 16.9% higher than with single-bolted connections under identical loading conditions. Therefore, test results confirmed that double bolted connections provide more secure connections overall. Double-bolted connections will therefore be used at connections of the single angle members for the Superway's canopy.

The Steel Institute specifies that three types of connections are commonly used in steel structures: welds, bolts, and rivets. Rivets are described as having relatively low strength compared to bolts, somewhat outdated in that they are gradually being replaced by bolts, and are considered less efficient connections for higher installation costs compared to bolts. Welds are described as difficult to make in the field and can crack under cyclic loads such as trains passing over a bridge, which is analogous to the Superway's cars riding through the guideway. High strength fiction grip (HSFG) bolts are recommended for reliable connections over black bolts where dynamic loads are involved; the basis for this recommendation is that the nuts of black bolts may become loose or the connection plate may shift until it is firmly pushing on the bolt, causing shear. HSFG bolts provide efficient connections by using the tension in the bolt to ensure against this slip; these are recommended for use with a washer under the bolt head. These bolts are typically fastened using a calibrated wrench or the turn-of-the-nut tightening method. Lastly, since ideal concentric connections with one bolt connecting all members are usually not possible in the field, the centroidal axes of the truss members at a connection need to meet at a point as show in Figure XX, which will be used at the connections of the main truss members in the racking designed for the Superway.
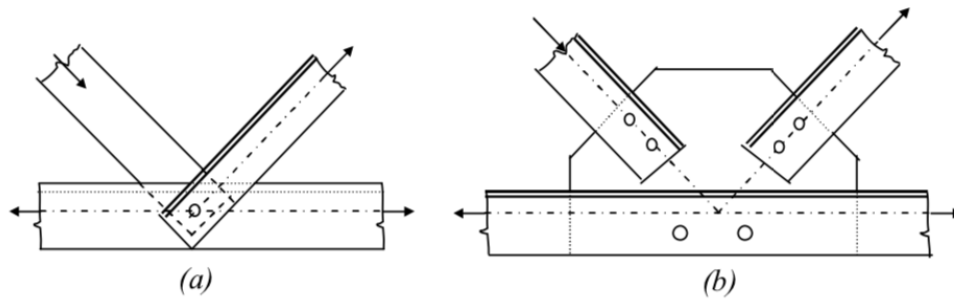
**Fig. 1 Concentric Connections**

Figure XX. Connections for Single Angle Struts. The ideal concentric one-bolt connection is shown on the left. The more realistic connection used in practice is with the centroidal axes of the members meeting at a point on the gusset plate as shown on the right. This type of centroidal connection will be used at connections between the main members of the truss; bolts will be aligned on the centroidal axis of the members. (CITE SOURCE FOR THIS FIGURE)



| ITEM NO. | DESCRIPTION | QTY. |
|---|---|---|
| 1 | N-S GIRDER | 1 |
| 2 | E/W Z PURLIN | 1 |
| 3 | 1/2" HEX BOLT | 1 |
| 4 | 1/2" FLAT WHASER | 2 |
| 5 | 1/2" SPRING LOCK WASHER | 1 |
| 6 | 1/2" HEX NUT | 1 |

DETAIL A
SCALE 1 : 4
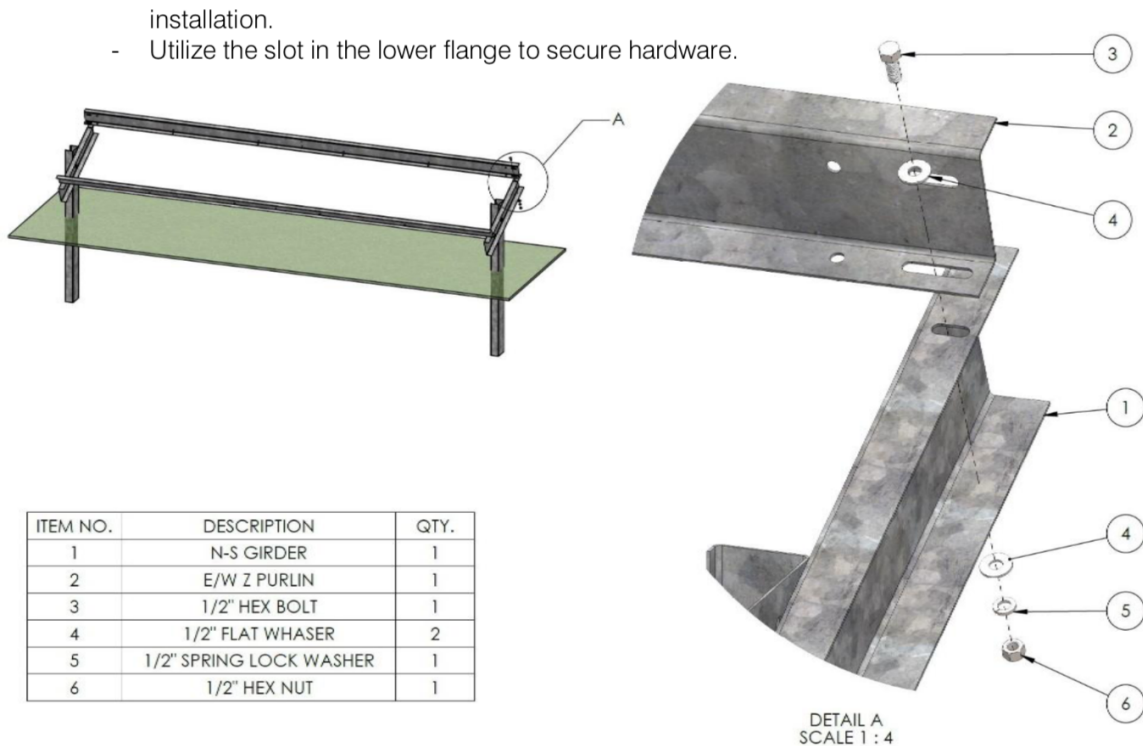
Figure XX. Hardware Used in Genmounts Ground Mounted Racking. This ground-mounted racking solution is constructed of C-channels with Z-purlin mounted on top. An arrangement of a bolt, washers, and nut are shown. This type of hardware is considered viable to work into the connections of the steel angle model.

G.H.S Fasteners, a company specializing in the manufacture of HSFG bolts, clarifies that this particular bolt type is commonly used in construction and structural steelwork. The bolts are typically made from medium carbon steel and obtain their high level of strength at a microscopic level from treatments such as tempering and quenching. HSFG bolts are uniformly pre-tensioned to proof loads to prevent the loosening of nuts. Frictional resistance between these bolts and the corresponding hole to which they are mounted ensure that the connection does not shift under various types of loads. HSFG bolts are available in a variety of sizes from M6 to M64 and of various grades from 8.8 to 10.9, which specify the strength of the bolt. This type of bolt is therefore considered a viable to connect the members of the racking.



Figure XX. HSFG Bolts. Typical finishes, parts, and finished used in HSFG bolts are shown. A complete assembly of a bolt consists of the bolt coupled with washers and nuts.

The Steel Institute details a procedure to compute the tension capacity required for the bolts selected for a connection as well as the minimum plate thickness. The geometry detailed in this procedure was analogously applied to the gusseted connections connecting the members of the racking together to establish the bolt size and reasonable plate thickness for the gusset plates. The calculation procedure involves the loading and several geometrical parameters listed in the procedure. A general diagram of the geometrical parameters as shown in the guide is shown below, and the detailed calculation is included in Appendix XX.
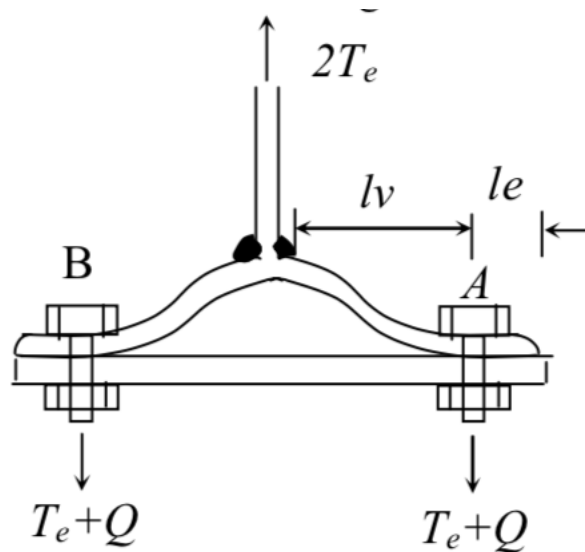
**Figure XX. A Schematic of the Parameters Used to Calculate the Tension to be Safely Resisted by the Selected Bolt and Determination of Minimum Plate Thickness.** Corresponding quantities from this diagram made by the Steel Institute for bolted connections with plates were designated for corresponding structures on the racking. The detailed calculation is described in Appendix G.

The recommended FOS used for bolts is 8.5, which leads to the selection of Grade 10.9 M12 bolts to resist the tension requirement calculated using the methodology above, which is detailed in Appendix G.

The American Iron and Steel Institute enumerates specific parameters for the spacing of bolts and the distance at which bolts should be placed from the edge of a member in structures composed of light gage steel members. It specifies that the spacing of bolts and the distance from the center of any bolt to the end or boundary of the connecting member cannot be less than either 1.5d or $\frac{P}{f_b t}$, where

d = diameter of bolt, in
P = force transmitted by bolt, lb
t = thickness of thinnest connected sheet, in
$f_b$ = basic design stress, psi

This calculation was carried out to figure out the minimum spacing of the bolts and distance from the edges of the L-channels and is detailed in Appendix H.

## 4.2 Wind Loading

Stathopoulos et al. validated that the effects of building height and specific panel location on a roof do not significantly affect wind loading by testing panels equipped with pressure taps at different elevations and arrangements. Small but insignificant differences in the wind pressure coefficients were observed, and it was concluded that these small differences could be considered negligible (Stathopoulos et al., 2013). This information makes it reasonable to designate corresponding structures between roof mounted arrays and the Superway's canopy. Structural code developed for the design of rooftop arrays can therefore be used to design the canopy.

Axinte et al. determined that installations of photovoltaic panels on parking structures were subject to regions of high turbulence created by streamline separation. The eave of the roof becomes a separation point for air flow (Axinte et al., 2013). ASCE design code prescribes local pressure coefficients for canopies and other plane surfaces, which result in conservative values for design loads that take turbulence, geographic, and several other factors into account. Using these coefficients to calculate design wind loads the mounting will need to withstand will help account for the turbulence from flow separation.

Maffei et al. postulated that upward wind forces are usually the most critical to consider for the panel's racking. The support structure needs to withstand reactions at the attachment points, and individual members need to clear calculated internal forces. The racking should distribute uplift forces throughout the solar array to avoid locally overloaded components; the entire system of ballasts and system's overall weight contribute to resisting uplift. Furthermore, wind forces need to move from panels to racking to the supporting structure, forming a complete load path (Maffei, 2014). It will be critical to ensure that loads on the Superway's canopy follow a similar distribution of loads.

Messenger and Ventre enumerate procedures to properly characterize wind loading on solar arrays. Most PV arrays can be approximated as large flat plates tilted at various angles to the direction of wind flow. These flows create stresses and forces in the structural members holding up the array. Wind loading on a canopy can induce cyclic tension and compression in the members, making it important to account for fatigue. To establish design wind pressures the mounting will need to withstand, standards and procedures developed by ASCE are recommended. Maps indicating basic wind speeds are provided, along with formulas, tables, and charts for computing the velocity pressure. Equations to compute the gust effect factor for various terrains, force coefficients, and wind loads to be accounted for in the calculation are also detailed. The equation for final design pressure on an array is given by Equation 1:

$$p = q \, G \, C_f \qquad\qquad (1)$$

where q, the velocity pressure, is found using Equation 2:

$$q = 0.00256(K_z)(K_{zt})(K_d)(V^2)(I) \qquad (2)$$

Where

$K_z$ is the velocity pressure coefficient at a height z
$K_{zt}$ is the topographical factor
$K_d$ is the wind directionality factor
$V$ is the basic wind speed in mph
$I$ is the importance factor
$G$ is the gust effect factor
$C_f$ is the force coefficient

Messenger and Ventre then state that off-the-shelf solar racking components are typically designed with a factor of safety of two against the highest wind pressure obtainable from ASCE's calculation procedure: 55psf (Messenger and Ventre, 2003).  The wind pressure calculated specifically for the Superway's array is 24.56psf; the detailed calculation is shown in Appendix A. To follow common industry practice, the components have been designed to safely withstand the maximum pressure of 55psf
Updates to ASCE 7 (2016) introduce a more specific version of equation 1 to calculate the design wind pressure on a rooftop array ("Wind Loads: General Requirements", 2016)

$$p = q_h G C_{rn} \hspace{3cm} (3)$$

where $q_h$ is calculated using Equation 2 above and $GC_{rn}$ is determined using Equation 4:

$$GC_{rn} = (\gamma_p)(\gamma_c)(\gamma_e)(GC_{rn})_{nom} \hspace{1.5cm} (4)$$

ASCE Figures with definitions of each variable and assumptions made to approximate the Superway's canopy are shown in Appendix A.


## 4.3 Simulation

### 4.3.1 Wind Loading Simulation

Baetu et al. specify several steps in the procedure to analyze wind loading effects on a ground mounted solar array using ANSYS CFX software. The study was conducted on a twelve-panel array arranged in three rows and four columns, with an overall inclination of 30 degrees. The arrays dimensions are specified as 5.828 by 2.976m with a thickness of 0.04m. Dimensions of the flow domain are defined in terms of the height H from the ground to the highest point of the upper panel: 5H above the top of the array (total 6H),  a distance of 5H from the inlet to the object, 5H on the sides of the array, and a distance of 15H from the array to the outlet as pictured in Figure 16. Turbulence intensity is set to 1%, and a wind velocity of 18 m/s with zero-degree angle of attack normal to the array are specified. (Baetu et al., 2013). The geometry and conditions were recreated in SOLIDWORKS Flow simulation, and a similar pressure distribution to the study as shown in Figure 17 was obtained.
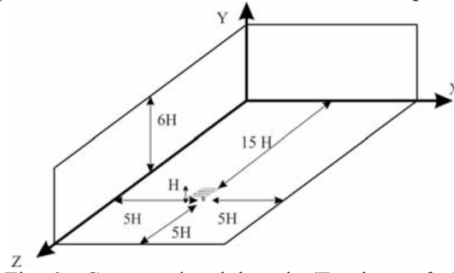
**Figure 16. Dimensions of the Flow Domain.** Recommended dimensions of the flow domain (Computational Domain, from (Baetu et al., 2013)).
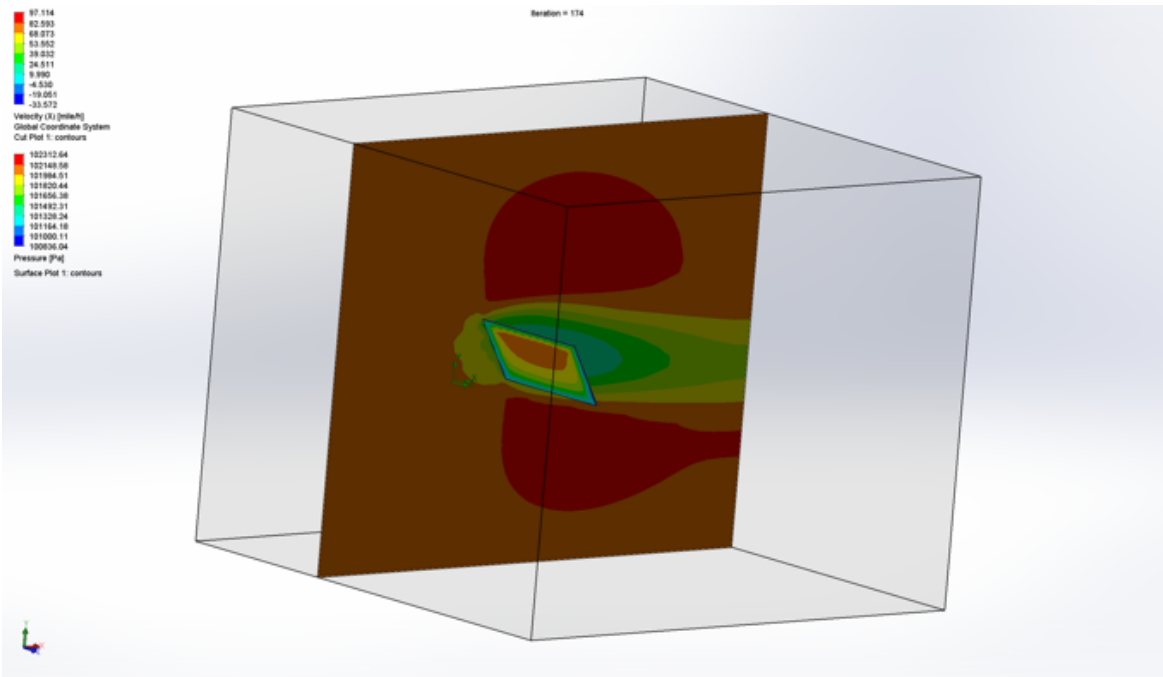


**Figure 17. Recreated flow simulation from the study conducted by Baetu et al. (2013).** Reproduced simulation results for the wind pressure acting on a sloped 12-panel canopy.

Shademan and Hangan define a similar set of flow simulation criteria as Baetu et al. in a study focused on the effects of various wind directions and inclination angles on ground mounted solar panels. A flow domain is defined in terms of the length, width, and height of the array, with the flow domain extending further downstream of the canopy than upstream. A refined mesh is used for a small flow domain around the panels, and a coarse unstructured mesh is used for the rest of the flow domain (Shademan & Hangan, 2009).

As mentioned in section 4.2 above, common practice the solar industry is to design racking components to withstand a worst case ASCE wind loading pressure of 55psf. In alignment with this practice, the integrity of the racking was assessed using carefully defined static simulation studies in Solidworks with a pressure of 55psf applied to the underside of the panels. The steps taken to complete these simulations are detailed in section 6.

Solidworks documentation and a simulation guide devoted to the assessment of structures using Solidworks static studies were heavily consulted to overcome several errors encountered during

the process of running the simulations. A general summary of these tips is listed as follows; specific information on recommended settings are discussed in Section 6.

- Simplification is recommended and crucial in getting simulations to run successfully; including all components of a design on a spectrum from large to small may lead to unreasonably long simulation times
- Simplifying the model can drastically increase the chances of obtaining reasonable results that can be used to assess the model. Defining connections accurately to closely mimic the behavior of the actual connections leads to more feasible simulation times and reduces errors as opposed to including every miniscule piece of hardware or parts in the model during simulation.
- A comparison of a series of simulations completed on a simple model of two plates bolted together showed that with all connection hardware included vs. hardware removed but connections accurately defined showed a difference in displacement of 0.279mm, which could be considered insignificant for most applications. The simplest simulation case involved the globally bonded contact definition, which essentially assumes that the intersecting sections of the plates are glued together. There was a more drastic difference in the resulting stress values (161.4 MPa for both the globally bonded and pin connector studies vs. 516.4 MPa for the study with locally bonded and no penetration contact sets). The latter maximum stress appeared at the bonded edges of the bolts. This aligns with expectations since the study now assumes the two plates are held together at the bolt holes instead of being glued together across their entire intersection. These higher stresses and corresponding change in location were expected in the study with local contact sets since the bond is now specifically between the edges of the bolt holes, which closely mimics the actual bolted connection without introducing the actual connectors into the study. The reported difference in time was drastic: an increase of 25x the completion time of the simplest all bonded study was observed for the final study including bolt connectors.
- Using the information from this guide, the simulations conducted on the racking were also be simplified to work around several errors encountered when the entire model including all hardware was analyzed. A progression from simplest to more complicated study was created using the settings described as above. The details of these simulations are described in section 6.
- Pieces of Solidworks documentation and help forums pointed towards manually adjusting mesh size to overcome meshing errors when attempting to run a simulation study rather than choosing to generate a global mesh. Additionally, a curvature based mesh could be generated on parts where the standard meshing operation failed so the discretization more accurately followed the profile of the part. Mesh sizes for smaller parts would need to be specified to ensure they meshed properly
- For the case of disappearing members in simulation results, documentation pointed to meshing failures that the software fails to recognize and still computes the desired result. These members will not appear in the stress or displacement contours. To avoid this occurrence, meshing should be performed manually before running the study rather than automatically by the solver to ensure that all parts display a mesh before the study is run.

Sun et al. compare several methodologies used to assess and design structures composed of single-angle members. Finite element analysis is said to provide good results when used to assess the strength of structures composed of single-angle struts such as trusses. FEA can be used to determine the load-carrying capacity of angle struts and accurately captures the effect of eccentric end loads as long as end restraints are clearly defined. To properly assess the strength of the Superway's racking design, carefully prescribed connections at the ends of the members will need to be defined to produce meaningful results.

Sun et al. also emphasize that second-order analysis of such structures provides the best benchmark to assess the viability of the structure in comparison to approaches based on prescribed formulae. Numerical approaches are recommended to capture the effects of eccentric connections and other realistic conditions in the structure; most deformation was found to be out of the plane of the members rather than in plane. Plate elements or beam-column elements are recommended to capture the effects of buckling and cross-sectional distortion.

The American Institute of Steel Construction (AISC), which focuses on the design of steel structures for stability, confirms that FEA can be used to characterize second-order effects in structures through either an iterative approach or geometric-stiffness-based method. For the iterative approach, the iterations continue until convergence is reached, which means the calculated deformations level out around a certain value. Geometric stiffness methods do not require iteration since they effectively change the stiffness matrix to simulate the effects of the loads. Both methods have drawbacks: the iterative approach is computationally demanding, but the geometric stiffness approach requires that a very reasonable load is used for the adjustment of the stiffness matrix.

### 4.3.2 Seismic Simulations

The Structural Engineers Association of California (SEAOC) enumerates some guidelines on seismic considerations for rooftop arrays. As of 2012, the International Building Code (IBC) and California Building Code (CBC) did not have explicit seismic requirements for rooftop arrays. SEAOC cites ASCE 7 specifying that friction cannot be depended on for lateral resistance. This is interpreted to mean that the mounting structure holding the panels needs to be able to resist movement during a seismic event. Dynamic analysis is used to compute the displacement of a PV array during a seismic event. The paper then explicitly states that the supporting structure is considered to behave linear-elastically during seismic vibrations. The array's displacements are the most important result to consider in this type of study. From this information, it is assumed that a linear dynamic simulation in Solidworks will be able to properly characterize the movement of the array designed for the Superway under a prescribed seismic excitation.

Response spectrum analysis is used to apply data of accelerations, velocities, or displacements to simulate seismic events. Response spectrum data from actual earthquakes is used in several applications, but can be hard to obtain. Justification in the use of response spectrum analysis to

assess seismic integrity lies in the underlying assumption that these spectra contain the maximum response for several single degree of systems to an earthquake. Although the timing of the maximum responses differ between an actual seismic event and the simplified model of single degree of freedom systems shown below, the response spectra for the model and its real-world counterpart both record maximum responses to some type of excitation. A complete response spectrum has several peaks and troughs and can involve a large amount of data; a conservative approach involves the selection of an envelope of peaks to use in a given simulation as shown in Figure XX.
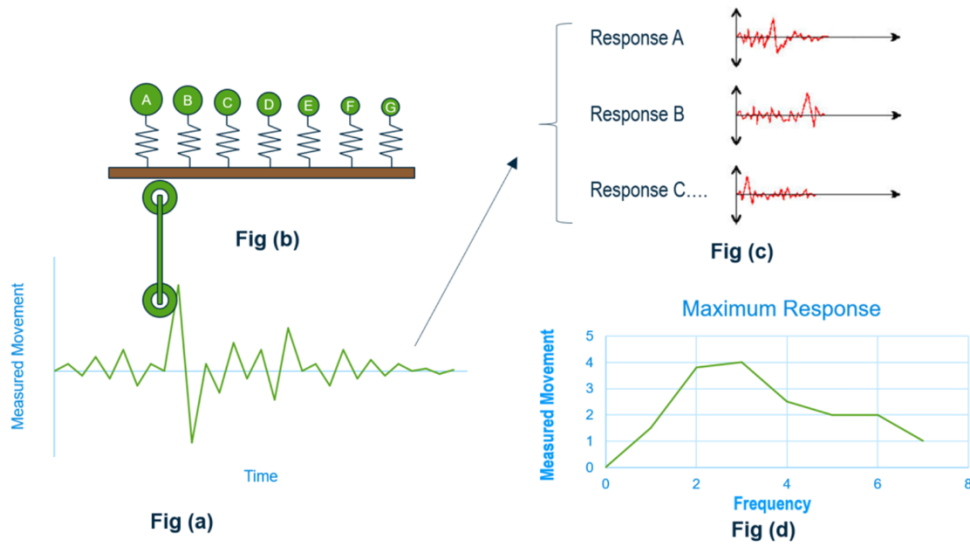


**Figure XX. The Basis Behind Response Spectrum Analysis and Why it is Considered a Conservative approach for Seismic Analysis.** The maximum responses from several single degree-of-freedom systems can be used to create a spectrum with an envelope of the maximum values as shown in (a) through (c). The resulting spectrum shown in (d) can be used to conservatively assess the response of structures to seismic excitation.

Mass participation plays an important role in a linear dynamic study with response spectrum analysis. Before solving the study as a whole, the frequency is run to ensure that the model will be adequately excited by the response spectrum in the direction of excitation. Effective mass participation factor (EMPF) represents the percentage of a system's mass that participates in a particular mode; a mode with a large EMPF is considered to be a significant contributor to the dynamic response of the system. A general rule of thumb set forth for response spectrum analysis is that the cumulative mass participation factor, which is the sum of the effective mass participation factor in each considered mode, in the direction of excitation needs to meet a threshold of 0.8 or 80%. Enough modes need to be included in the study to meet this threshold to ensure adequate excitation of the model.

# 5. DESIGN CONCEPT

## 5.1 Functional Requirements

Identifying key parameters the racking would need to satisfy was an important first step used to drive the brainstorm for a design. A list of the most important parameters considered is as follows:
- Mountable on top of the guideway's ribs or horizontal bridges between the ribs before guideway placed on vertical supports (on-ground assembly)
- Design for a representative straight section of guideway
- Aesthetical
- Modular
- Three panel span with an overall slope of 15 degrees for a single guideway; Six panel span with an overall slope of 15 degrees
- Reliably withstand critical wind and seismic loads; associated dead loads of the canopy would be accommodated by the guideway design
- Streamlined panel and mounting structure installation
- Accessible for maintenance of individual panels
- Minimize material use

## 5.2 Materials Selection

Material selection was based on a compromise between reliability, cost, and manufacturability. Materials commonly used to construct structural members include aluminum and steel; these materials offer durability against several types of degradation. Solar mounting is prone to corrosion, UV radiation, static forces, and dynamic forces. Although aluminum offers benefits such as lower mass and corrosion resistant alloys, steel was chosen to construct the racking. Low-carbon steel is already used in existing mounting structures for various types of photovoltaic installations, proving its reliability. Steel structural members can be armed against corrosion through treatments such as hot-dip galvanizing, which coats the structure with a layer of molten zinc. Consequently, lower cost steel can be made corrosion resistant like aluminum, which is significantly more expensive. In addition, steel alloys have a well-defined endurance limit compared to aluminum alloys, which do not have a concrete quantity defined (Messenger & Ventre, 2003). Lastly, material properties such as thermal conductivity and coefficient of thermal expansion make welding steel more favorable than welding aluminum. Steel has a lower thermal conductivity than aluminum, making it easier to concentrate the temperature at the site of the weld. The coefficient of thermal expansion for steel is lower than that of aluminum, making it less prone to the formation of gaps and cracks during solidification since it expands less. Oxide layers form rapidly when aluminum is welded and can make the weld less homogenous (Hickey, 2018). Steel therefore collectively satisfies more criteria for this application and makes it the material of choice to construct the racking. A comparison of several material properties is included in Table 1.

| | A36 Carbon Steel angle | 6061 Aluminum |
|---|---|---|
| **Corrosion Resistance** | Galvanization | Inherent in alloy |
| **Yield Strength** | 250 MPa | 48 MPa |
| **Tensile Strength** | 400-550 MPa | 115 MPa |
| **Fatigue Limit** | 212.5 MPa | Arbitrary Definition |
| **Coefficient of Thermal Expansion** | $\dfrac{12.1 \times 10^{-6}}{°C}$ | $\dfrac{23.4 \times 10^{-6}}{°C}$ |
| **Thermal Conductivity** | $51.2 \dfrac{W}{m \times K}$ | $180 \dfrac{W}{m \times K}$ |
| **Density** | $7.858 \times 10^3 \dfrac{kg}{m^3}$ | $2.7 \times 10^3 \dfrac{kg}{m^3}$ |
| **Elastic Modulus** | 190-210 GPa | 70-80 GPa |
| **Cost** | Low | High |

**Table 1: Comparison of the Material Properties of Steel and Aluminum.** A summary of the properties of low carbon steel and aluminum used to determine the material best suited for this application ("Steels, General Properties", 2020) and (Messenger & Ventre, 2003).

A specific type of structural steel widely used in the construction industry is ASTM A36 steel angle. This material is available at an economical cost and is considered very workable in terms of weldability and machineability (CITATION). Treatments such as galvanization can make these channels durable for outdoor applications. Additionally, these L-channels are available in a variety of equal and unequal leg dimensions. Iterations of the racking's trussing have led to the selection of this material to construct the trussing since it satisfies manufacturability, durability, and cost requirements enumerated for the Superway's racking.

## 5.3 Geometric Design

### 5.3.1 Overview

The main body of the mounting structure is comprised of two components: trussing constructed of A36 steel angle and Z-purlin. L-shaped brackets secure the bottom face of the trussing onto bridges the guideway. Three units of the racking placed adjacently to each fit on a representative 12 meter section of the guideway. Bridges between the ribs are required every third rib on the current guideway design. General specifications of the complete assembly are detailed in Table 2 for the HSS model and in Table 3 for the current steel angle model.

| | |
|---|---|
| **Length** | 241.90in (6.14m) |
| **Width** | 42.65in (1.08m) |
| **Weight of Racking** | 1,446.7lbs |

| | |
|---|---|
| **Weight of 12 Commercial PV Panels** | 600lbs |
| **Total Weight** | 2,046.7lbs |
| **Dead Weight (Following convention of assuming weight acts uniformly over canopy area of $253ft^2$)** | 8.1psf |

**Table 2:** Specifications including dimensions and weight for each unit of the HSS mounting design.

| | |
|---|---|
| **Length** | 121.25in (3.08m) |
| **Height** | 26in (1.08m) |
| **Width** | 157.5in (4m) |
| **Weight of Racking** | 528.21lbs |
| **Weight of 6 Commercial PV Panels** | 300lbs |
| **Total Weight** | 828.21lb |
| **Dead Weight (Following convention of assuming weight acts uniformly over canopy area of $126.5ft^2$)** | 6.547psf |

**Table 3:** Specifications including dimensions and weight for each unit of the current steel angle mounting design.

## 5.3.2 Trussing

Trussing dependably supports a variety of critical structures including roofs and bridges; it is therefore deemed appropriate to construct the foundation of the canopy. A simple Warren truss was designated as a starting point since it employs the fewest number of members, satisfying the goal to minimize overall material use. Following the profile of Warren trusses, diagonals were introduced into the dimensions specified for the canopy, oriented so that diagonals act in tension and compression under critical uplift loading on the upper chord of the truss. The lengths of these members were modified to fit under the polygonal upper chord, which follows an incrementally angled profile to a achieve a total slope of 15 degrees within the dimensions specified in Figure 18. Lateral stability at the bottom chord is achieved by members perpendicular to the plane of the truss at regular intervals as shown in Figure 20, which also add sturdiness throughout the structure by incorporating the verticals. Other trussing schemes with vertical members such as Modified Warren and Pratt were kept in consideration in case the canopy required more stiffness than achievable through a Warren truss.
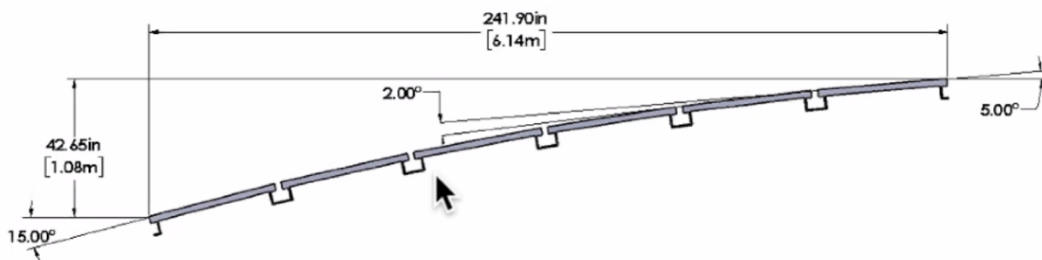


**Figure 18. Specified Dimensions and Sloping for a Double Guideway Canopy** (Spartan Superway, from (Futran, n.d.)). These dimensions and sloping of a 6-panel canopy wide customized for the Superway were used as driving parameters in the design. A 3-panel width canopy with these dimensions cut in half were adopted to design the racking for a single guideway, which can also be used on double-guideway sections without having to reduce the total number of installed panels. This eliminates a region of exposed canopy in between two guideways, which may be considered aesthetically displeasing to a pedestrian from street level.

The first iteration of the trussing was constructed of standard 4" x 2"x $\frac{1}{8}$" hollow rectangular sections that have been welded together. Structural advantages of using hollow rectangular sections include their high weight to capacity ratio along with good compressive and tensile strength ("Hollow Sections for Structural and Mechanical Application", 2013). Furthermore, flat outer faces allow for full contact between faces of the truss base and critical attachment points at both the guideway and Z-purlin. Manufacturing benefits in using hollow rectangular beams include availability in a variety of dimensions and allowability for the angled cuts at edges

required to accomplish the slope of the canopy. Lastly, exposed trusses are typically constructed of hollow sections with closed outer surfaces for aesthetic purposes ("Trusses", n.d.).
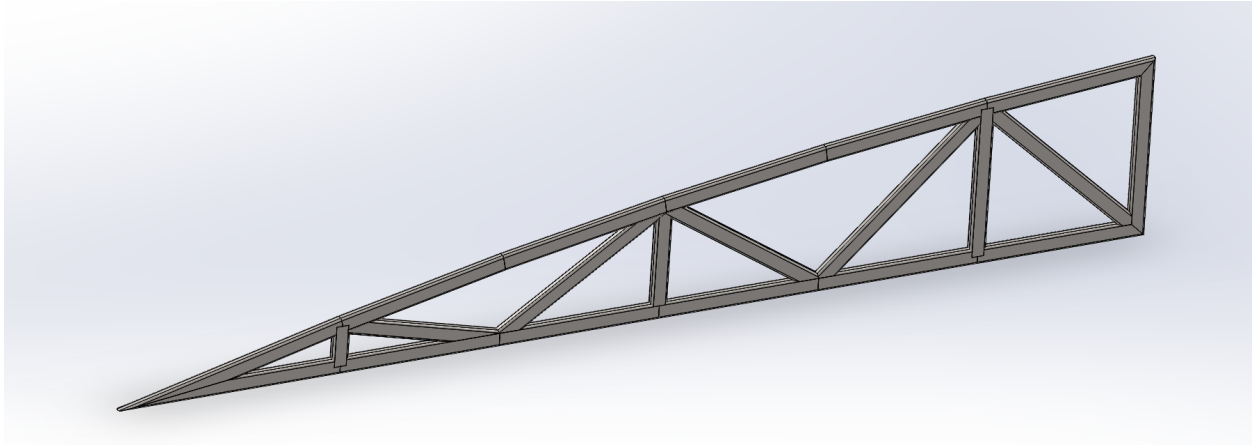


**Figure 19: A Unit of the Initial Trussing Constructed of Hollow Rectangular Sections for a Double Guideway.** The trussing consists of a Modified Warren Truss constructed of hollow rectangular sections adapted to fit under the slope of the canopy. A truss holds the racking at opposite sides of each unit.
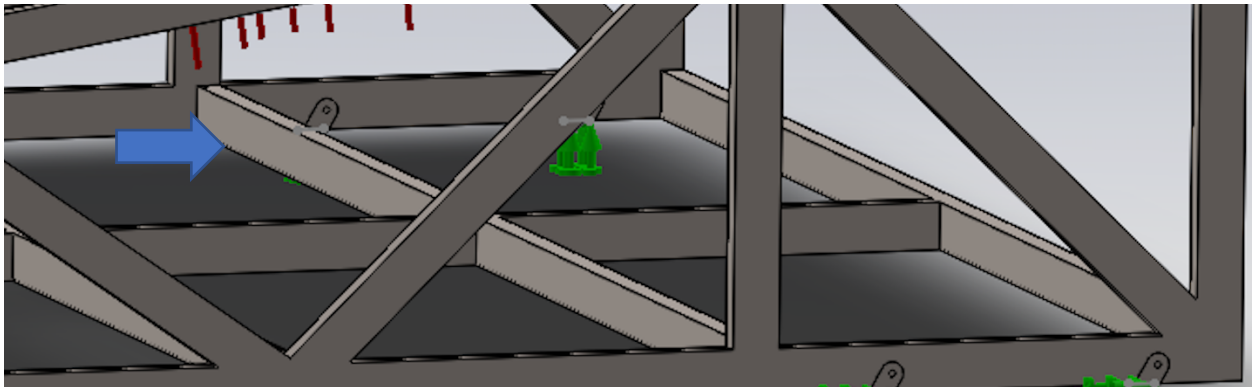


**Figure 20. Members for Stability at Base.** Members perpendicular to the plane of the truss indicated by the blue arrow at regular intervals along the bottom chord provide lateral stability.

A modified version of the pointed edge of the truss was designed to accommodate the minimum angle of 35 degrees recommended for the diagonals at the lower end of the trussing. The middle diagonals are angled at 48 degrees, and the diagonals on the left edge are angled at 55 degrees as shown in Figure 21. This arrangement of diagonals allows for the canopy's 15 degree slope and diagonal angling within the specified length of 241.9 inches. These changes were made to the trussing and incorporated into the design. However, the final design reverted back to the pointed edge for the trussing since this minimizes the overall height of the canopy.
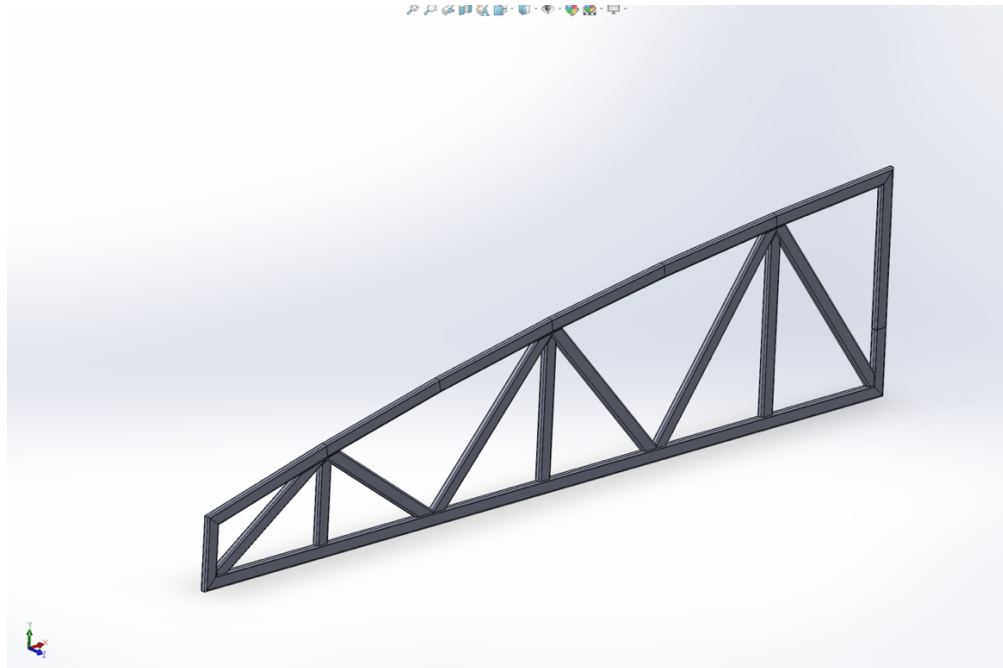
**Figure 21: Modifications to Trussing.** Proposed modifications to lower end of trussing to ensure all diagonals meet the recommended 35-55 degree angling requirement. These changes were not adopted in the steel angle design to compromise between the angling of the diagonals at the lower end of the canopy and the overall height of the canopy.

The second and current iteration of the trussing design is constructed using 2" x 2"x $\frac{1}{8}$" A36 steel angle channels to facilitate manufacturability while keeping costs within a realistic limit. Critical wind loading simulation results from the initial rectangular HSS model pointed towards using L-channels close in dimensions to the hollow rectangular sections to maintain structural integrity under critical wind loading. The 2" x 2" equal angle size was selected as a reasonable starting point; 4" sizes of the angle members start at a width of 3", and the goal was to reduce overall material use. Larger sizes of the angle could be selected instead if the simulation results indicated the selected size of 2" did not provide satisfactory durability.
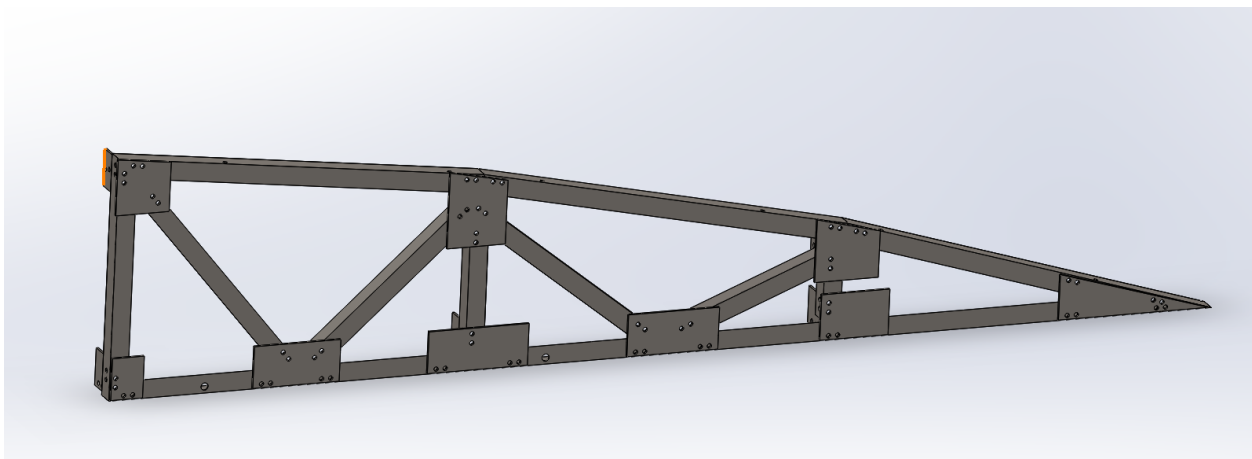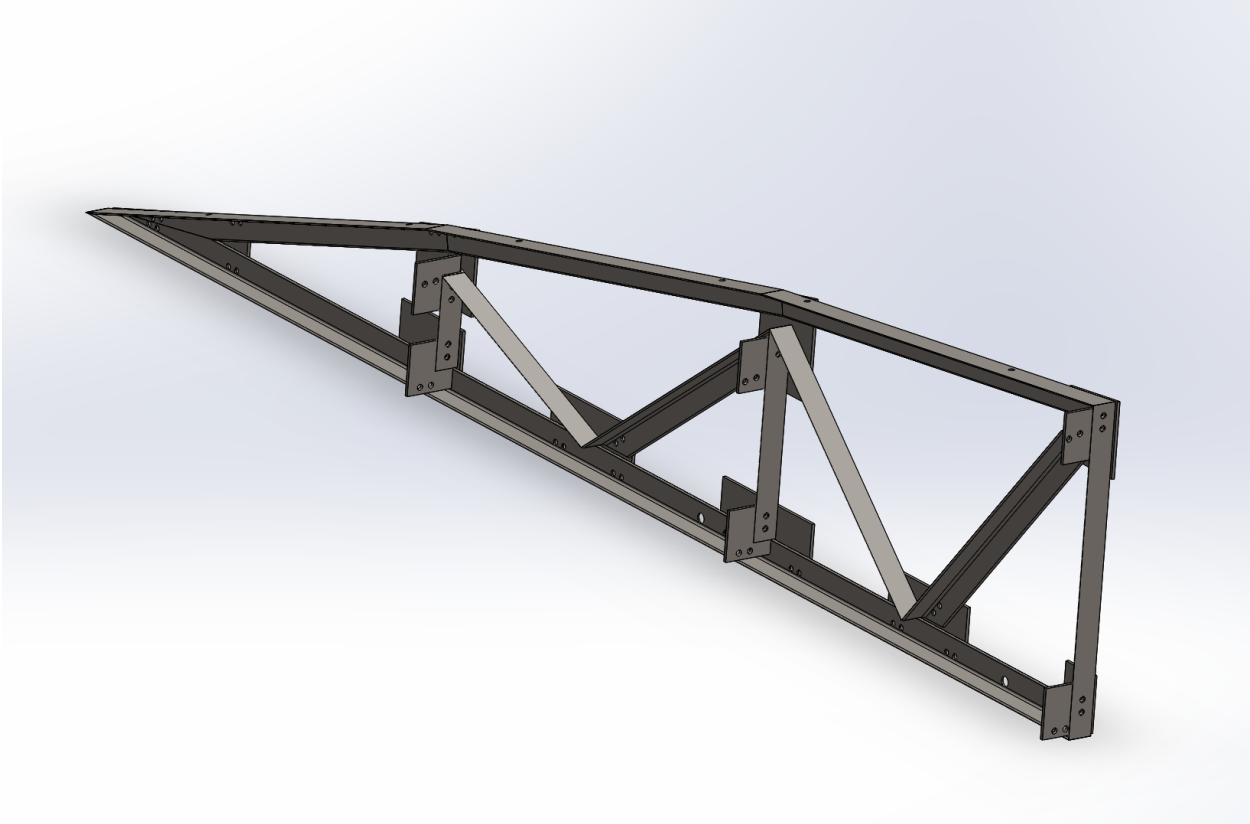
**Figure 22:** Steel Angle Trussing Designed for a Single Guideway. The second iteration of the trussing design is constructed of steel angle channels connected together using gusset plates. The gusseted connections have been designed to ensure that the centroidal axes of the members meet at a point as described by guidelines from the Steel Institute (see Section 4.1.1) used to design the bolted connections.

### 5.3.3 Z-Purlin and Clamps

For modularity, Z-purlins are bolted along the sloped profile of the upper chord of the truss. Framed commercial PV modules can be mounted on the Z-purlins using C-clamps customized to secure the two together, allowing for rapid and streamlined module installation. Four clamps are required to properly secure each panel, necessitating two purlins on each segment of the slope. These purlins are spaced to ensure the recommended panel gap of 0.25in. Furthermore, the Z-purlins provide lateral stability at the upper chord of the truss through an arrangement analogous to purlins running perpendicular to the plane of roofing trusses.
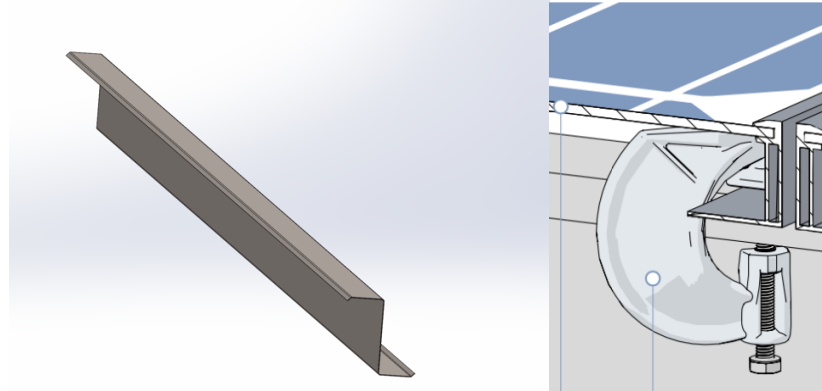
**Figure 22: Z-Purlin and C-Clamps**. Z-purlin (left) were modeled using dimensions from suppliers of the structural member. Clamps (right) to secure framed modules onto these Z-purlin are from the Mechatron, which manufactures several components of solar mounting (PV-CLAMP, from (Mechatron, 2020)).

Alternative clamps that can interface with purlins have also been considered including alligator clamps. These clamps may be more readily available locally in the United States than the C-clamps initially proposed, and do not require any significant changes to the design.

### 5.3.4 Brackets

Brackets designed to accommodate the two-inch width of the steel angle trussing are attached to bridges between the guideway's ribs. Units of the trussing will be placed in these brackets and bolted into place by a bolt running through the bracket and channel member. Two brackets are positioned on opposite sides of each trussing base, for a total of four brackets on each unit of the racking.
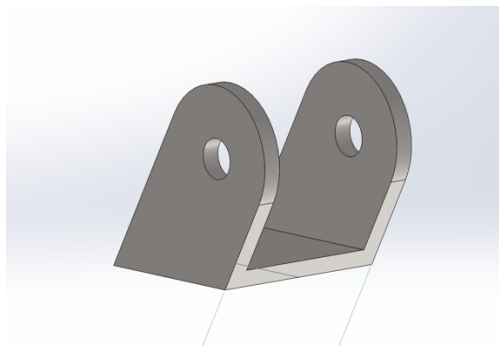


**Figure 23. Brackets to Secure onto Guideway.** An adaptation of U-brackets used in other elevated designs customized to secure the bottom chord of the racking to bridges on the guideway. The brackets will likely be welded to the bridges; the racking will be placed into the brackets and subsequently bolted in place.

### 5.3.5 Diagonal Bracing

Diagonal bracing helps stabilize the lower front end of the canopy by securing it to the guideway. Perforated Unistrut channels and brackets were assembled to create this bracing and

secure the pointed edge of the canopy to the guideway. This provides additional stability under critical wind loads and an added layer of security to increase the overall reliability of the canopy.
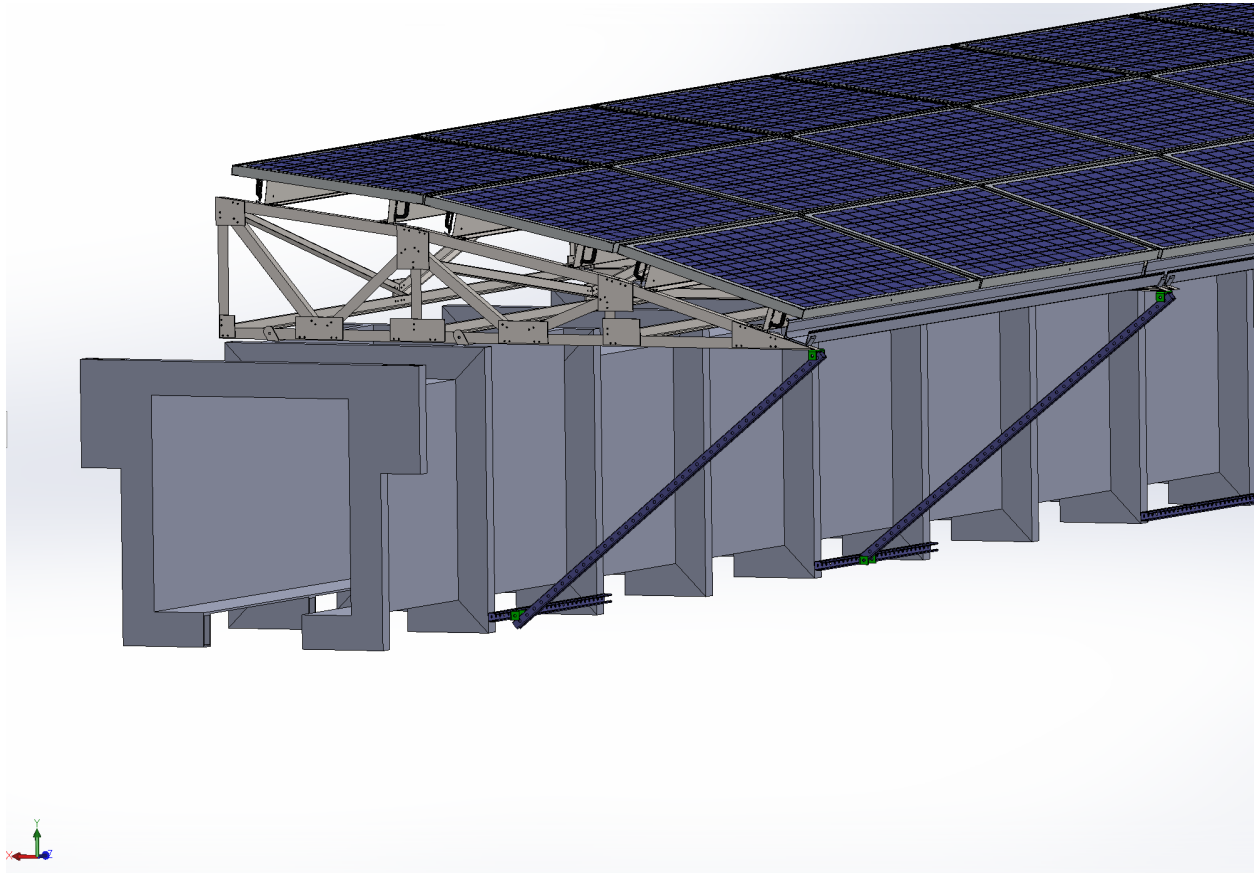


### 5.3.6 Panel Spacing and Gutter

Z-purlins have been mounted to accomplish the recommended panel spacing of 0.25in (6.4mm). This spacing will allow for sealing in between the modules to facilitate rainwater harvesting through a gutter mounted at the lower end of the array. Existing L-shaped gutter mounting brackets can be secured near the pointed edge of the canopy to provide an interface to hold sections of gutters. The selected gutter profile accommodates screens customized to fit in its upper bend to minimize debris entrance and buildup in the gutter channel as shown in Figure XX.
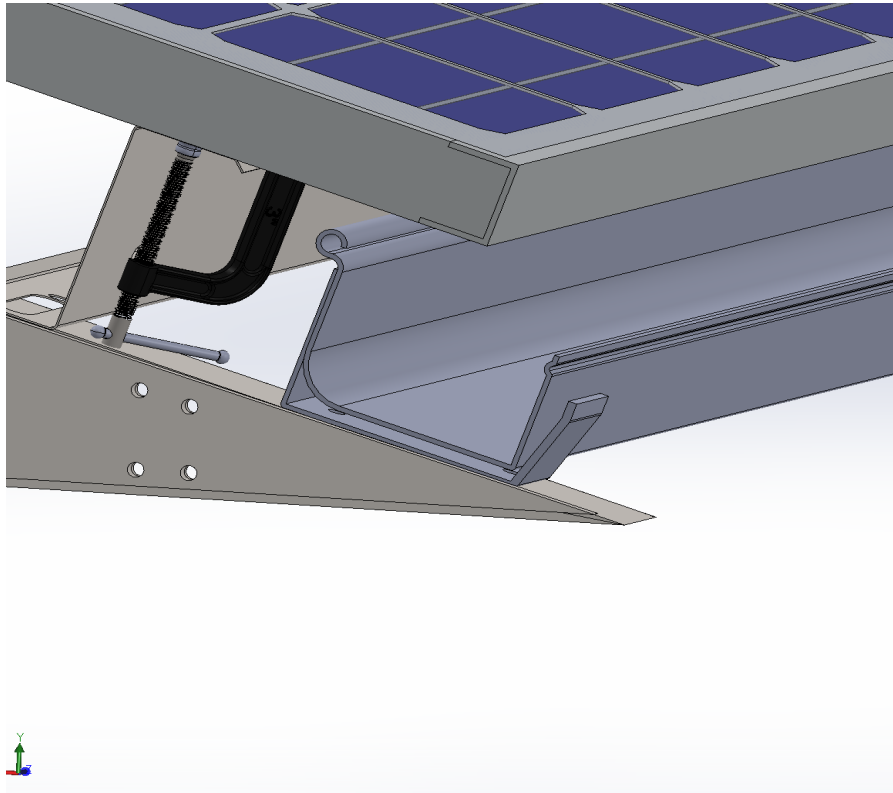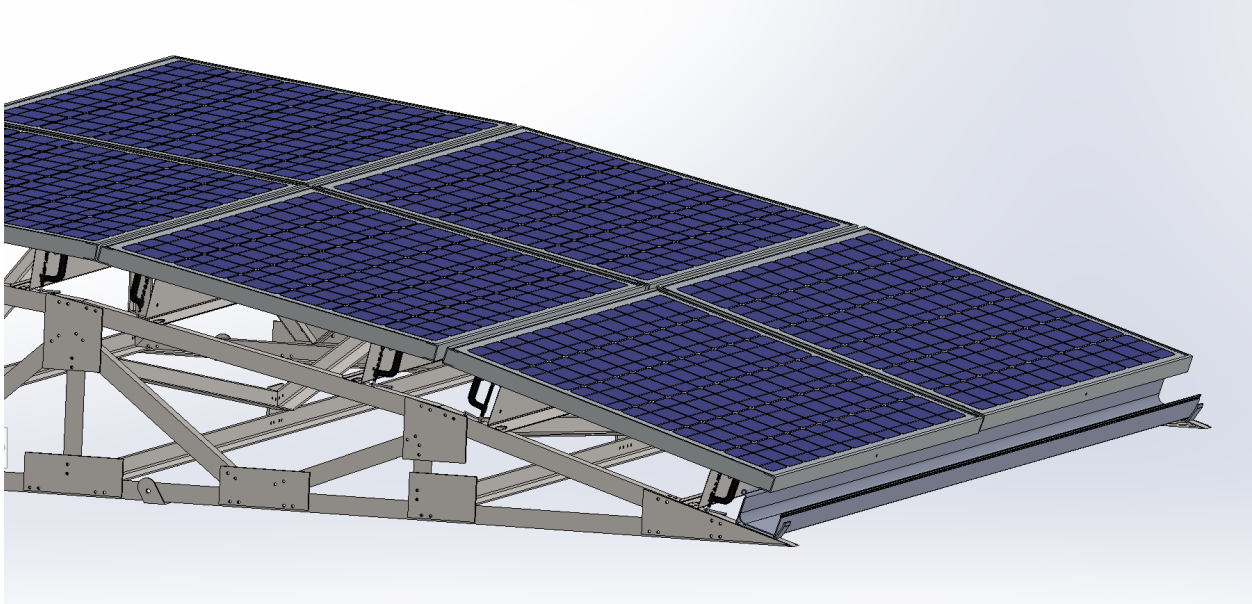
**Figure XX. Gutter for Rainwater Harvesting.** A simple gutter profile is mounted at the lower end of the array to create a channel to catch and route rainwater. The individual gutter sections can be mounted onto the racking using existing gutter mounting hardware as shown; L-brackets to hold the gutter sections can be screwed into the upper chord of the racking.

**Figure XX. Prevention of Debris Accumulation in Gutters.** Perforated profiles that can snap into the profile of the gutter can be used to prevent the accumulation of leaves and other matter in the gutters for rainwater harvesting.

### 5.3.7 Adjustability for Added Panels

For regions of the guideway where it is desired to have a larger canopy than the three-panel wide canopy designed, larger gusset plates can be attached to the higher end of the racking to accommodate additional steel angle members to hold more modules on a unit of the racking.

Figure XX. Adjustability for Added Panels. A concept for the accommodation of additional panels at desired locations is feasible by adding steel angle members at the upper end of the canopy. To accommodate these members, larger gusset plates at the corners where these members would interface with the main trussing unit would be required.
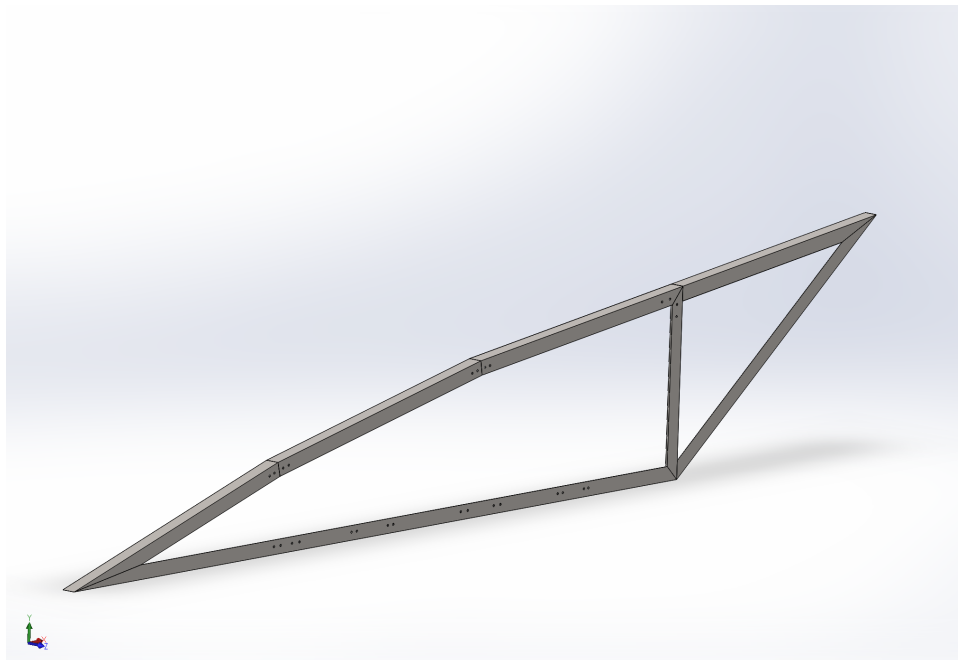
### 5.3.8 Wire Routing

The initial concept for wire routing involved a combination of holes along the center and bottom face of the Z-purlin and cable ties. The cable ties would be laced through the holes on the purlin, around the wires, and through the corresponding hole on the bottom face of the purlin to harness and direct the wires coming down from the modules. Subsequent refinement to this concept has lead to the introduction of closed channels to be mounted onto the holes on the Z-purlin to manage wires instead as indicated in Figure XX. This type of wire routing solution is used in Unirac and is specifically called "Solar Tray,"; it is deemed applicable to satisfy the requirement for closed channel wire routing.
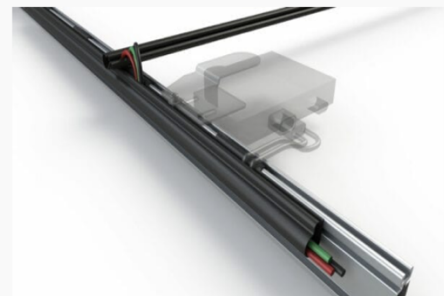




**Figure XX. Closed-Channel Wire Routing Solution from Unirac.** The SolarTray from Unirac can be used with the design for the Superway's racking to route wires through a closed channel.

These channels can be mounted onto the notch on the lower face of the Z-purlin in a manner similar to the Unirac renderings shown above. Alternatively, these channels can be mounted on the center face of the Z-purlin using the holes originally created for the cable ties.
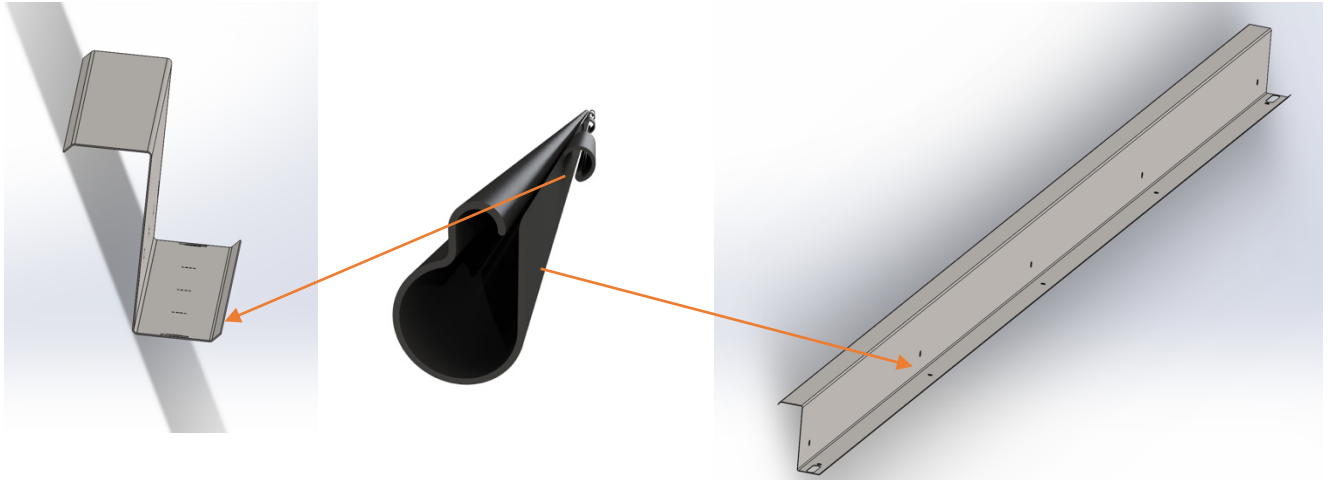


**Figure XX. Wire Routing Mounting on the Z-Purlin.** As mentioned above, the Unirac SolarTray can be mounted onto the notch on the lower face of the Z-purlin as shown on the left or alternatively screwed onto the center of the purlins using the holes originally created to run cable ties as indicated on the right

### 5.3.9 Connection Hardware

Bolts, nuts, and washers were introduced into the model with inspiration from the hardware used in the Genmounts ground-mounted racking described in section 4.1. The calculation used to determine the size of these bolts in included in Appendix XX. To withstand the tension value calculated for the bolts with a recommended factor of safety of 8.5, M12 bolts were selected along with their corresponding washers and nuts. The calculation of this sizing is included in Appendix XX. The calculation for the required spacing between these bolts and from the edge of the angle members is detailed in Appendix XX. These bolts were introduced into connections in the model as shown in Figure XX below. The recommended preload was chosen based on the recommendations from Reuss, which states that a maximum preload value for bolts should be selected for protection from joint separation due to overload conditions, shear, and thread loosening (Reuss, 2018). The chart used to determine this preload value is also included in Appendix XX.

Figure XX. Model with Connection Hardware. M12 Bolts with corresponding nuts and washers were introduced into the model at connection points based on calculations detailed in Appendix XX. The preload value for these bolts was selected as the maximum value for a M12 bolt from
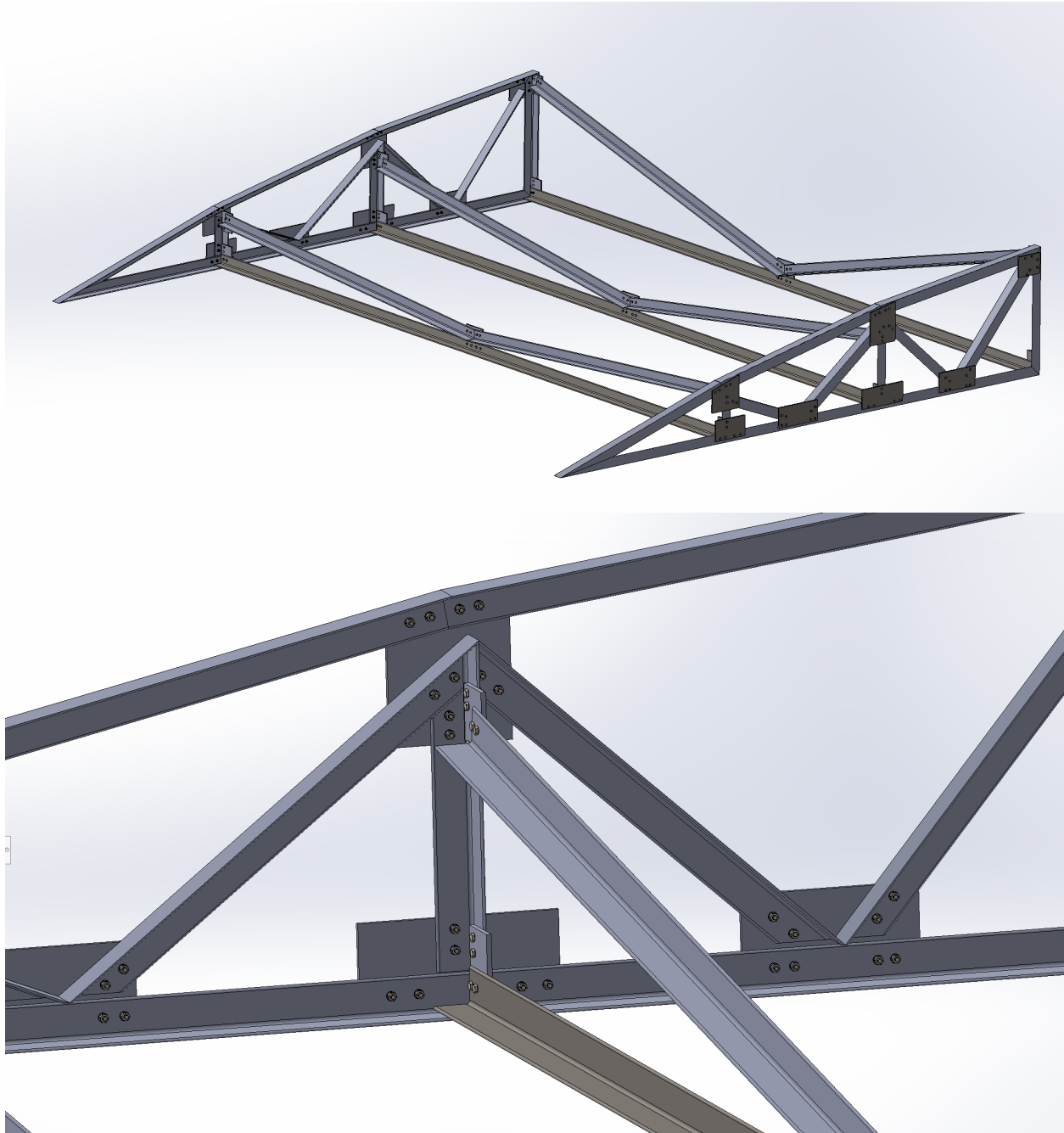
## 6.  Analysis of the Design

### 6.1 Wind Loading Simulation

CFD and static simulations were conducted on a fully assembled unit of the racking in separate studies using SOLIDWORKS simulation. The initial model was made of hollow steel section (HSS) rectangular tubing and the current design model is made of steel angle L-channels. The subsequent sections describe the setup of the simulation studies pertaining to these two models.

### 6.1.1 Geometry and Material Inputs

### 6.1.1.1 Hollow Rectangular Section Model

For the initial concept made of hollow rectangular sections 1023 Carbon steel, a low carbon alloy, was selected as the construction material. The assembly consisted of a unit of the truss foundation at each end made of hollow rectangular sections, two Z-purlin mounted on each slope increment of the truss, and simplified solar panels. The U-brackets to secure the racking onto the guideway were attached along the bottom chord of both trusses. These brackets will be attached to the guideway during actual installation and were attached to the mounting oriented as such to provide geometries to accurately apply fixtures.

To navigate around meshing errors on the original model created from hollow beam elements, a simplified solid model created from projections of the racking's geometry onto sketch planes was used to run simulations. This model adhered to the cross-sectional dimensions of the original model; hollow sections of $\frac{1}{8}$" thickness were created using the SOLIDWORKS shell feature. Z-purlins were simplified as rectangular prisms.

### 6.1.1.2 A36 Steel Angle Model

As described in section 5, the current version of the racking's trussing was redesigned using ASTM A36 steel angle members. The cross-sectional dimensions of the L-channels used to construct the trussing are 2" x 2" x $\frac{1}{8}$". The assembly consisted of a unit of the new truss foundation at each end made of the L-channels, two Z-purlin mounted on each slope increment of the truss, and simplified solar panels. The U-brackets to secure the racking onto the guideway were attached along the bottom chord of both trusses. SOLIDWORKS material library allowed the selection of A36 steel for the simulations, which were applied to the units of trussing. Plain carbon steel was specified as the material for other components of the racking such as brackets and Z-purlin. Z-purlins were simplified to rectangular prisms as done previously with the hollow rectangular section model to work around meshing errors from the software about generating a solid mesh on a thin part.

### 6.1.2 Boundary Conditions and Applied Loads

### 6.1.2.1 Simulations on the Hollow Rectangular Section Model

For the CFD simulations, air at a temperature of 298K was defined as the fluid. Turbulence intensity was defined at 1% based on guidance from the study by Baetu et al. consulted in the simulation section of the literature review. A wind velocity of 103mph in the x-direction was defined based on the maximum wind velocity specified by ASCE for San Jose.

For the static simulations, two pressures to apply on the panels were considered. Using ASCE 7-16's methodology a wind pressure of 24.6psf is obtained; the details of this calculation are included in Appendix A. However, common practice in the photovoltaic industry is to design solar array components to withstand ASCE's worst case design pressure of 55psf of uplift on the panels. Static simulations were therefore conducted with a uniform pressure of 55psf applied to the underside of each module to analyze if the structure would be capable of withstanding this force. Fixtures were applied at the bottom surface of the bracket and the inner edge of the bolting hole as seen in Figure 27 to mimic the behavior of attachments between the guideway, brackets, and mounting.

### 6.1.2.2 Simulations on A36 Steel Angle Model

ASCE's worst case design pressure of 55psf was also used to assess the strength of the racking constructed of steel angle. To resolve errors involving the meshing of the L-channels, the mesh size was adjusted to relatively fine elements to get the software to successfully generate a mesh on the model; specific sizes are detailed in Table 3. Fixtures were applied at the lower face of the brackets to mimic the racking's attachment to the guideway. Initial attempts of the simulation with the redesigned trussing included simple solar panels created from hollowed rectangular prisms to mimic the weight of actual solar panels; a pressure of 55psf was applied to the underside of these panels to assess the structure under ASCE's worst case wind loading. Although the simulation would begin to run, very little progress towards the simulation completing was achieved after several hours of letting the software run; the software would freeze at establishing the element stiffness matrices. Subsequent runs of the simulation were simplified in accordance with guidance from the simulation guide described in section 4.3.1. Since the L-channels required a fine mesh for the software to generate the mesh without errors, also including the solar panels in the study would mean unrealistically long computation times and require more robust computing hardware. To follow suggested simplification procedures, the equivalent point load from 55psf acting on the face of each solar panel was calculated and applied to the face of the purlins instead. This calculation is detailed below in Appendix A. An equivalent force in the opposite direction was defined on the purlins to assess the structure under compression.

Contact sets were refined for subsequent runs of the simulation as suggested in the guide described in section 4.3.1. Initial runs of the simulation were conducted with the global bonded contact, which essentially assumes all intersecting faces of the parts are glued together. This simulation did produce results, which are shown in Figure XX of Section 7 on discussion of results. However, these contact sets were refined for subsequent runs of the simulation to more

closely mimic bolted connections as detailed by the simulation guide. Local no penetration and bonded contact sets were manually defined at each bolt hole throughout the model; this makes the simulation assume that the parts are only connected at the bolt holes, which more realistically mimics the behavior of bolted connections. A representative graphic of this process is shown in Figure XX, which was repeated at each bolt hole in the model. A contact visualization plot showing the local contact sets throughout the model is shown in Figure XX. Results from these refined simulations showed a more realistic stress distribution at the bolted connections as shown in Figure XX of section 7.
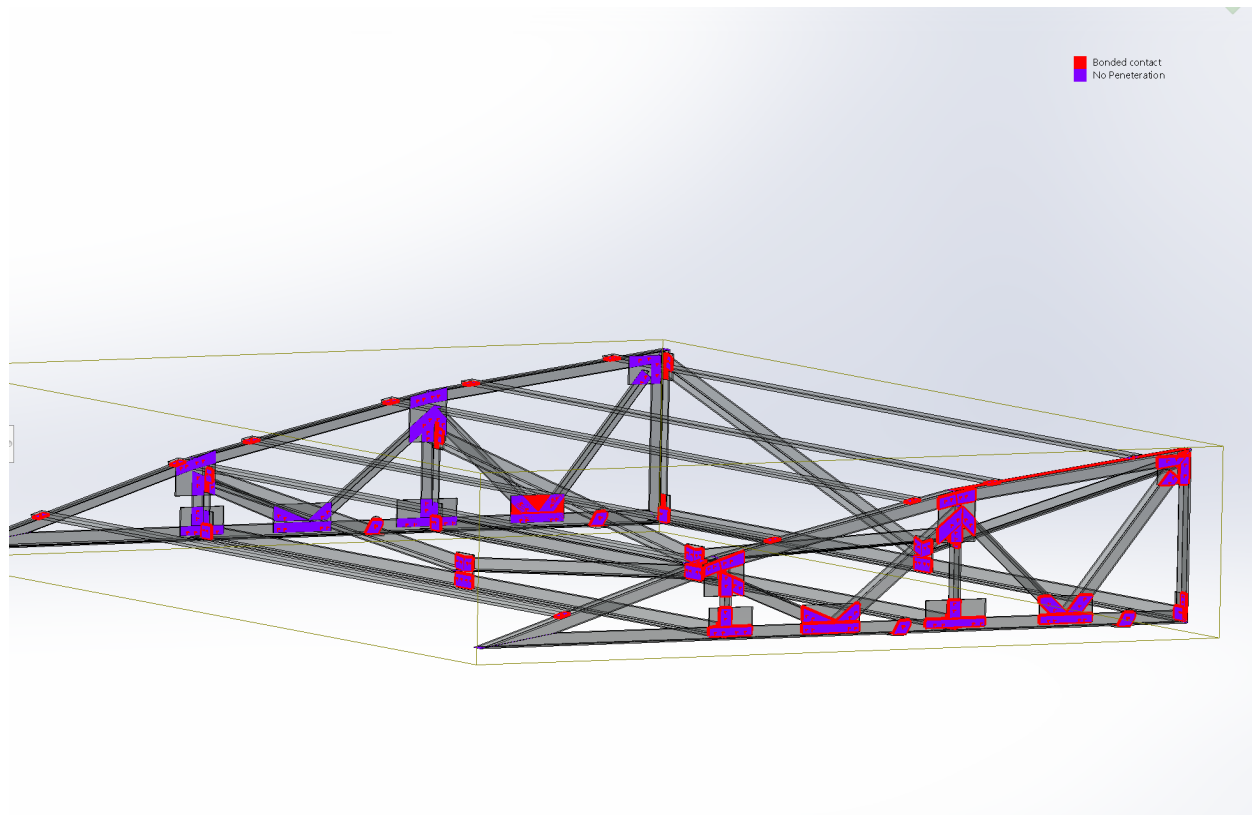


Figure XX. Contact Visualization Plot. Once the process of defining bonded and no penetration contacts at the bolt holes was completed, a generalized contact visualization plot of the model was generated to ensure proper sets were defined at each bolt hole. Bonded contacts are shown in red and were created between corresponding bolt holes on the parts; No penetration contact sets are shown in purple.

### 6.1.3 Discretization and Convergence

For the CFD simulations, initial runs used a global coarse mesh automatically generated by SOLIDWORKS. Both global and surface goals were defined within the simulation to monitor the solution and ensure that values converged for these criteria. These goals were defined as follows: a surface goal for force in the y-direction on the underside of the panels to monitor uplift, a global goal for total pressure, and a global goal for average turbulence intensity. Iterations continued until the values leveled out. The resulting pressure distribution was less

distinct using the coarse mesh as shown in Figure 25. Subsequent runs involved fine tuning the fluid zone mesh close to the racking's surface, and both upstream and downstream of the racking. Level of refining cells was changed from an initial value of three to six, seven, then eight; this made the cell size near the surfaces progressively thinner. Having these centroids closer together leads to a more accurate result. Advanced refinement options were applied in the regions between the solar panels to increase the number of cells to five, six, then seven in these channels. The setting to close thin slots was set below the five millimeter gap between panels to make the software recognize these slots as open. A more distinct distribution of pressures was obtained after these adjustments as shown in Figure 26.
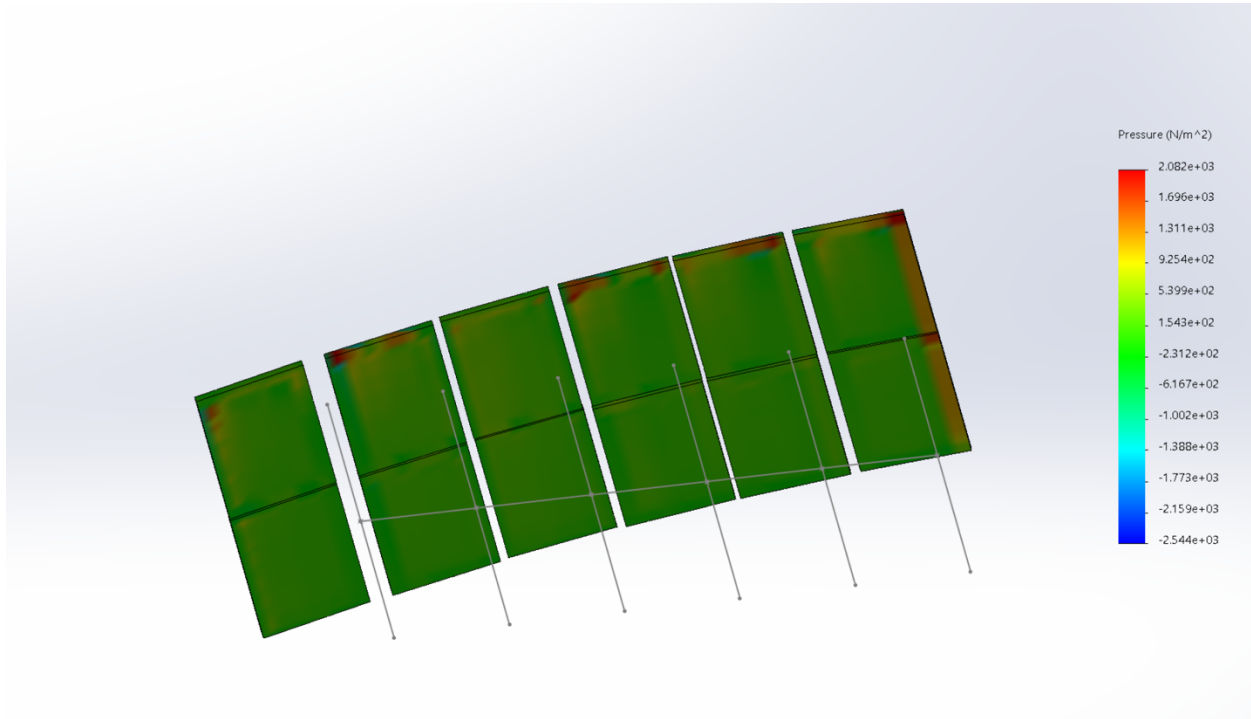


**Figure 25. Pressure Distribution on the underside of the panels using the automatic coarse mesh generated by SOLIDWORKS flow simulation.** A less pronounced pressure distribution resulted from simulations with the coarse mesh.
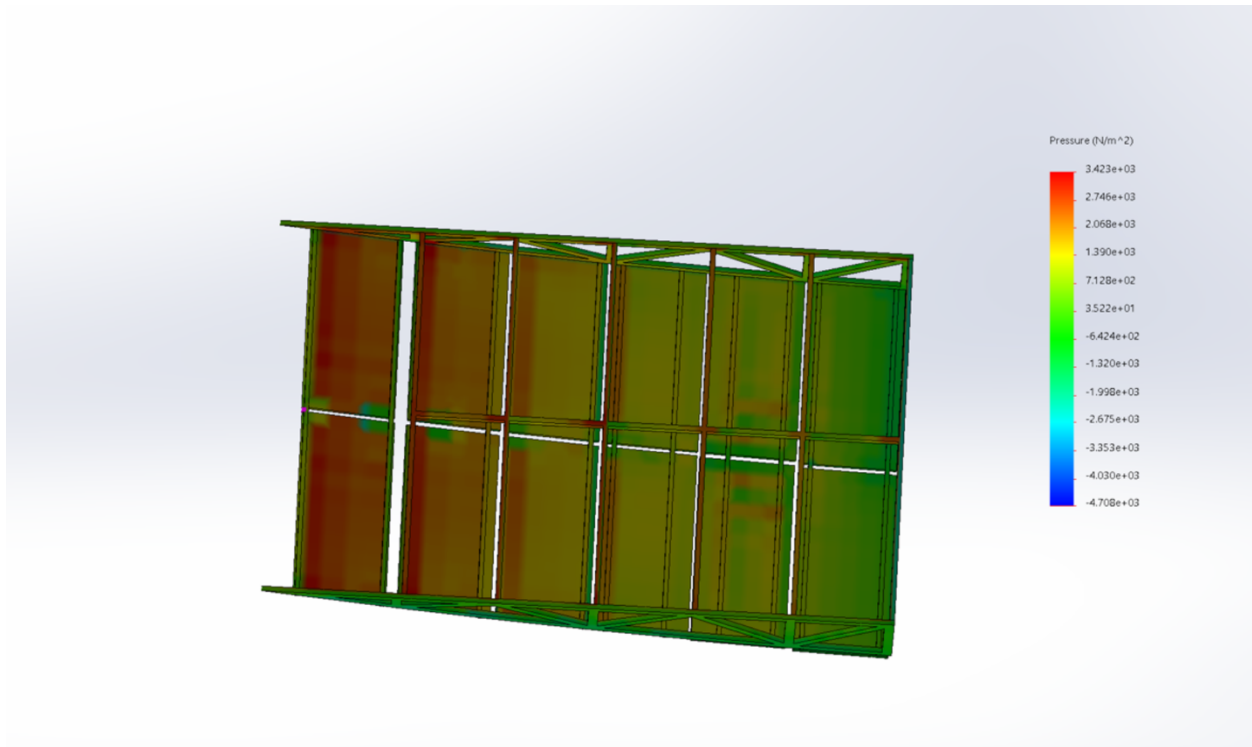
**Figure 26. Pressure Distribution on the underside of the panels after mesh refinement introduced on the fluid zone near the surfaces of the racking.** A more distinct pressure distribution is seen.

For the static simulations on the hollow rectangular section model, a solid mesh consisting of tetrahedral elements was generated on all components. This initial mesh was coarse for all components but was refined for subsequent runs. Smaller parts such as the brackets and the simplified purlins were individually meshed with gradually finer elements for each run of the simulation to ensure accurate results at these critical connection points as shown in Figure 27. Larger elements were used on the racking members and solar panels to avoid freezes in the software. Mesh sizes used for various components in the last run are detailed in Table 3.
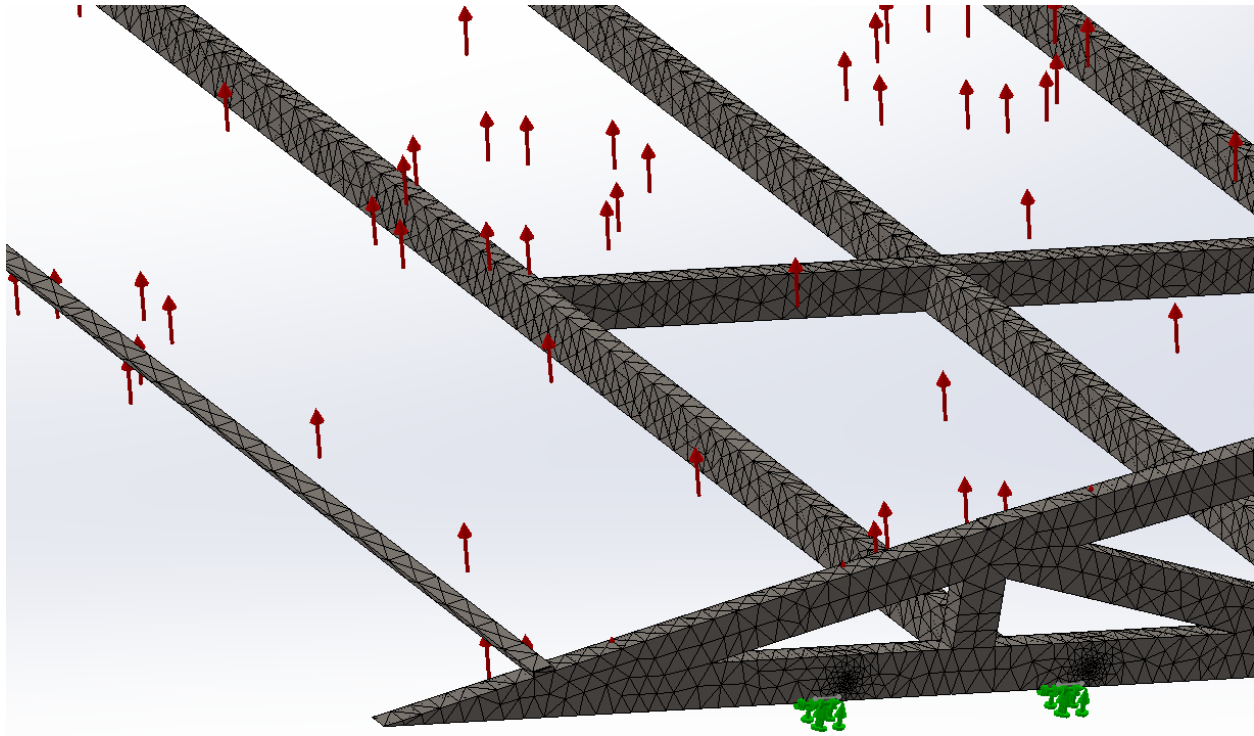
**Figure 27. Fixtures and Mesh Sizes.** Fixtures (indicated by the green arrows) were applied at the inner hole on the brackets and to the bottom face where attachment to the guideway would occur. Finer mesh sizes, seen at the fixtures in green, were used for the brackets compared to the purlins and trussing.

| Component | Mesh Size |
|-----------|-----------|
| Trussing | 1.0in |
| Purlins | 0.7in |
| Brackets | 0.17in |

**Table 4. Final Mesh Sizes for Each Component in Static Simulation.**

A similar process was used in the static simulations conducted on the L-channel model. A finer mesh than the hollow section model was needed for the trussing members to resolve meshing issues. The smaller parts such as the brackets were individually meshed with finer elements as previously done with the hollow section model to ensure accurate results at these critical connection points as seen in Figure XX. These mesh sizes are detailed in Table 5 below.

| Component | Mesh Size |
|-----------|-----------|
| Trussing | 0.6in |
| Purlins | 0.7in |
| Brackets | 0.17in |

**Table 5. Final Mesh Sizes for Each Component for L-Channel Model in Static Simulation.**
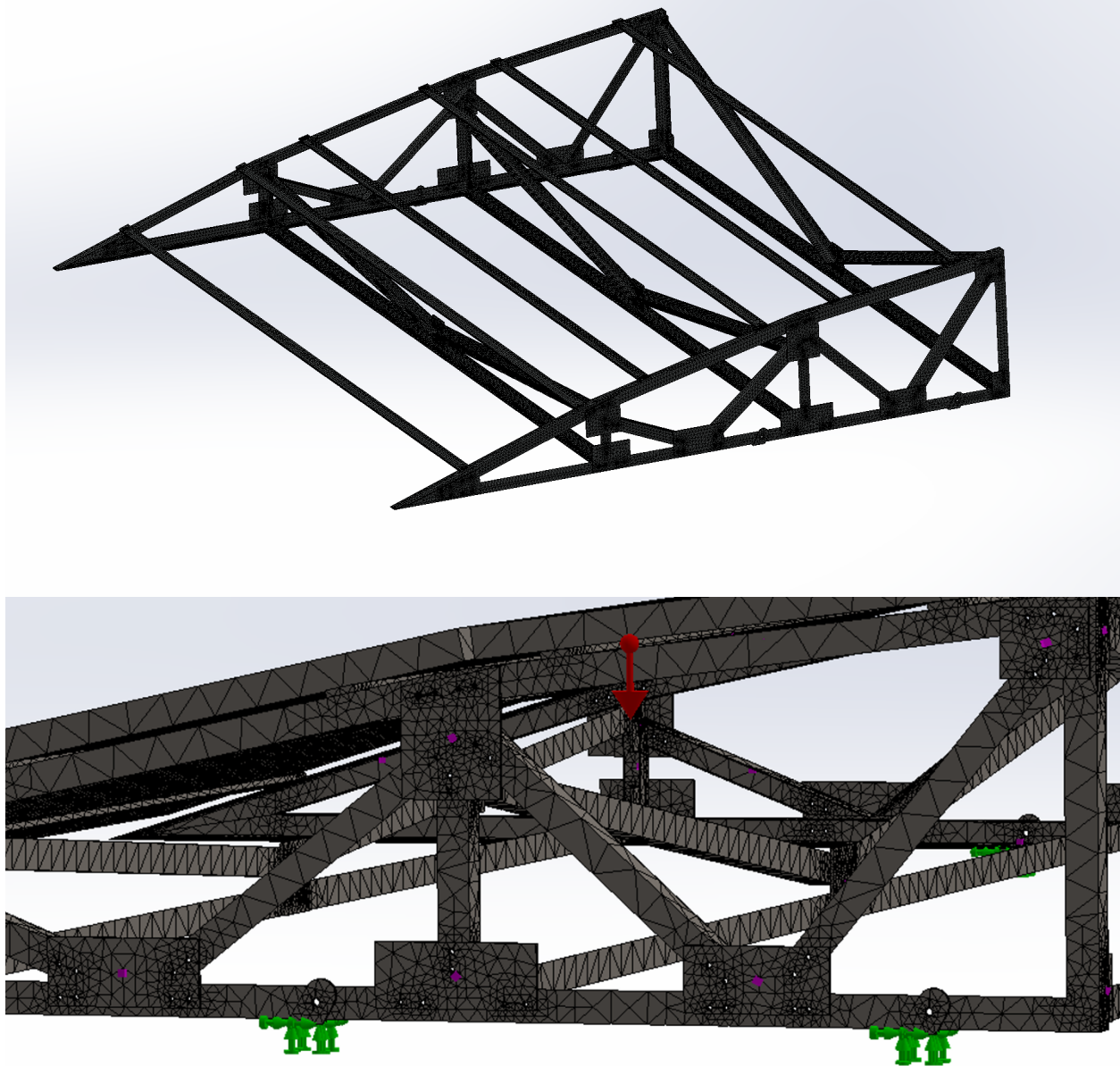
**Figure XX. Mesh Generated on the Steel Angle Model.** The upper rendering shows a general view of the mesh generated on a unit of the steel angle racking design. The mesh refinements near the bolt holes and on the brackets can be seen in the lower rendering.

In accordance with recommendations from a simulation guide focused on the convergence of simulation results in Solidworks, the p-adaptive method was defined for both simulations for uplift and compression. It was recommended that the criteria for convergence should be defined with respect to strain energy as opposed to the Von Mises stress or displacement to ensure a more accurate solution was obtained. The maximum order of the polynomials was left at a default value of 5 as recommended by the manual; the maximum number of loops was also left at a default value of 4. Representative convergence plots from the uplift and compression directions are shown below in Figures XX-XX; the studies continued to iterate until the specified

42

strain energy change of less than 1% was achieved for both studies. The plots for stress and displacement are included in Appendix XX.

**Uplift Loading at 55psf Plots**

**Figure XX.** **Total Number of Iterations to Achieve the Strain Energy Change Parameter Defined for the Uplift Simulation Study**. This plot was shows the total number of iterations completed by the solver before the defined strain energy criteria was met in the p-adaptive simulation study used to assess the racking under uplift.
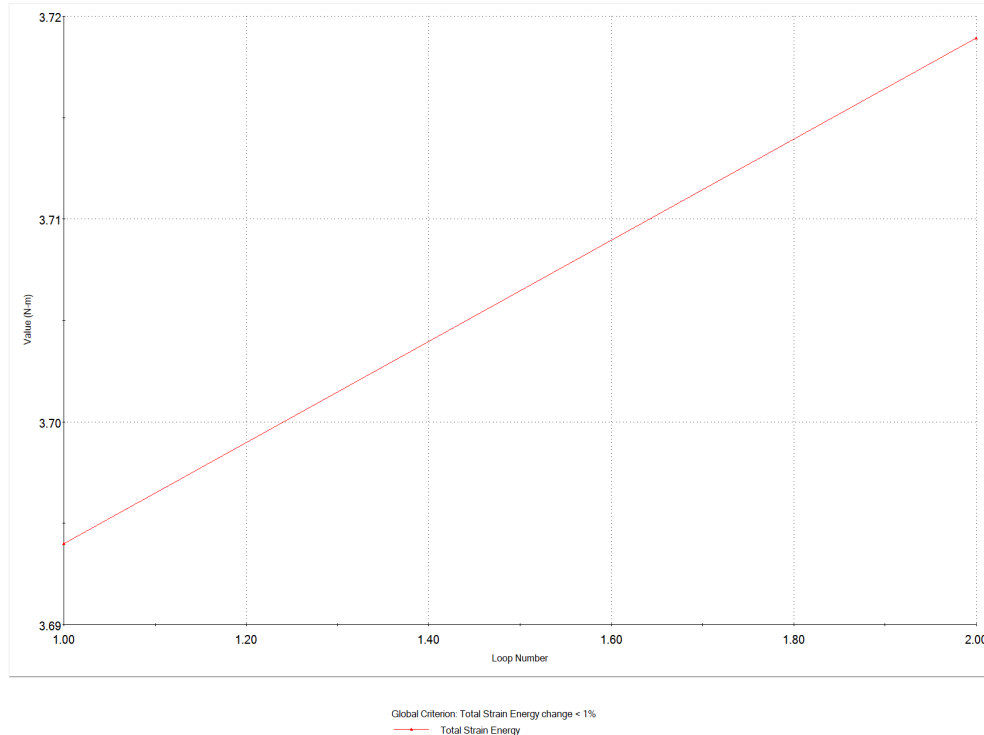


**Figure XX. Strain Energy vs. Loop Number from P-Adaptive Study Results.** This plot was obtained from the p-adaptive study results used to assess the structure under uplift loading. The

plot shows that the global criterion for total strain energy change of less than 1% was achieved at the second loop.
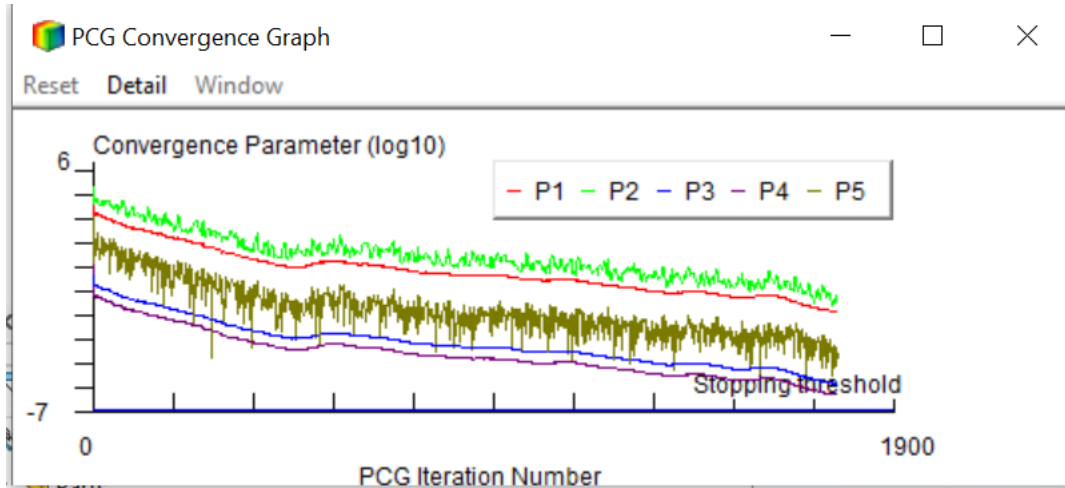
**Compression Loading at 55psf Plots**



**Figure XX. Total Number of Iterations to Achieve the Strain Energy Change Parameter Defined for the Compressive Loading Study.** This plot shows the total number of iterations conducted by the solver for the p-adaptive study used to assess the racking under compression.
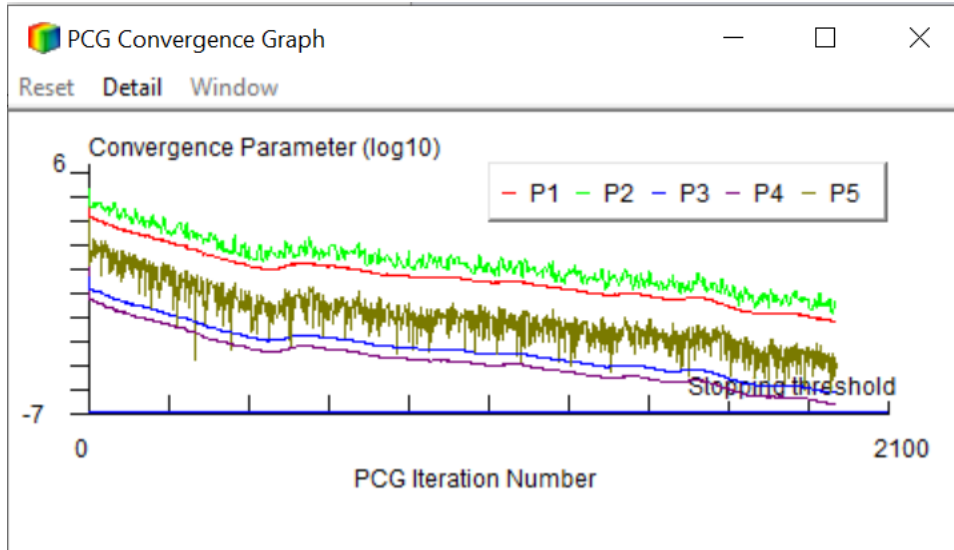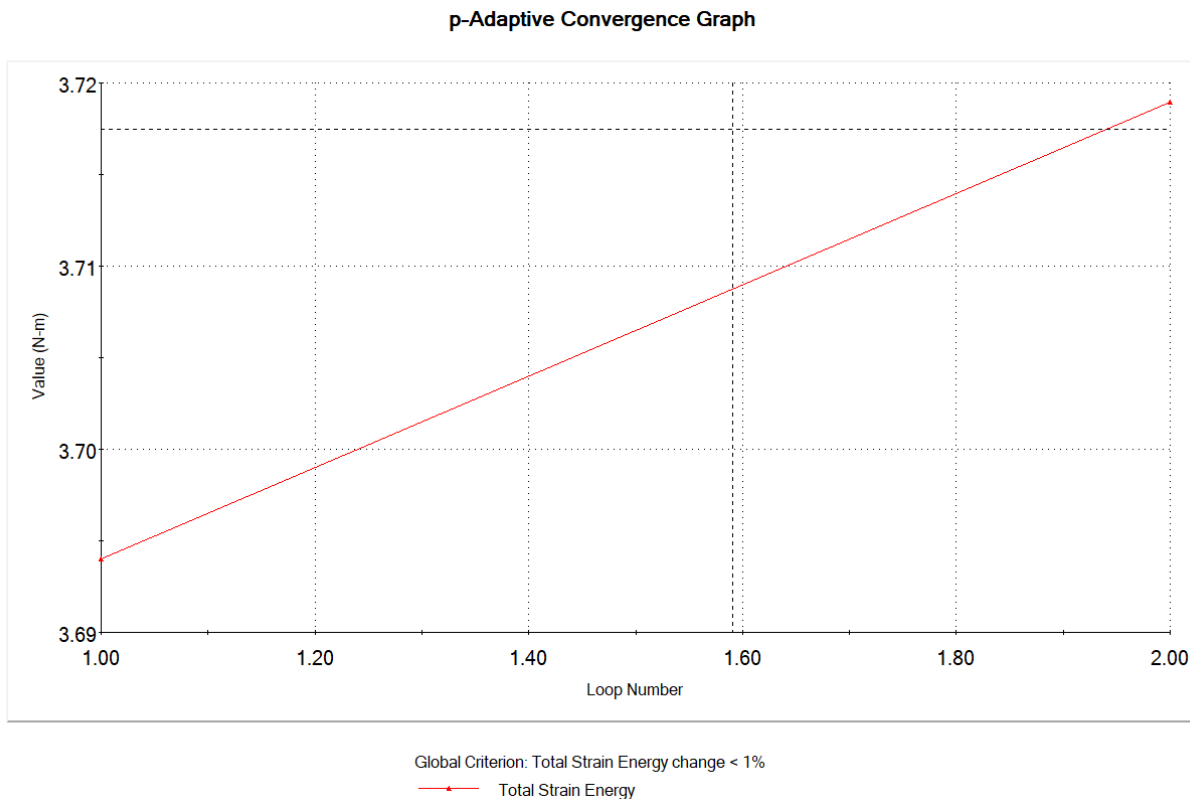
**Figure XX. Strain Energy vs. Loop Number.** This plot from the p-adaptive study used to assess the structure under compressive loading. The plot shows that the global criterion for total strain energy change of less than 1% was also achieved at the start of the second loop for this study.

### 6.1.4 Verification and Validation

CFD simulations were used to characterize the effects of wind flow on the canopy and mounting structure. Resultant pressures on the canopy were compared with calculated pressures from the methodology specified by ASCE for rooftop arrays. The maximum pressure of 20.6psf obtained from the CFD simulations (shown in Figure 28) was less than the resultant value from ASCE's method of 24.56psf. Therefore, designing with ASCE's wind pressure was considered the more conservative approach; differences are likely due to ASCE's incorporation of several real-world factors that affect the behavior of wind around an array through various coefficients. However, comparing these pressures confirmed that approximations in geometries made to utilize ASCE code did not lead to unrealistic quantities for pressure on the canopy; the geometrical analogies made between the Superway's array and a rooftop array were relatively reasonable approximations.
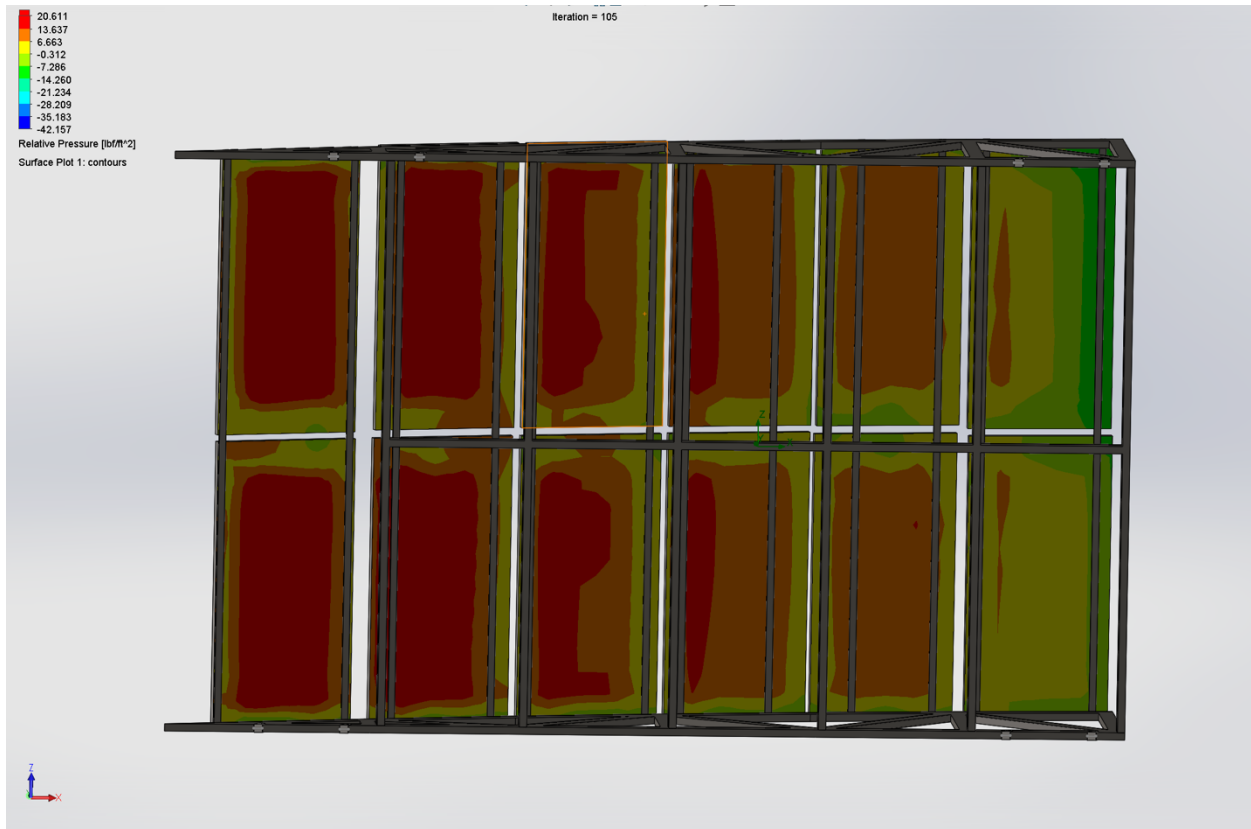


**Figure 28. Contour of pressures from CFD.** Pressure distribution on the underside of the panels from wind at 103mph in the X-direction. The maximum pressure, shown in red, is about 20.6psf.

A static analysis of the structure through hand calculations was carried out to validate the results of the static simulation, and is detailed in Appendix B. For the 55psf wind loading case, a contour of the normal stresses in the y-direction is shown in Figure 29 below. The resulting stress on this contour was compared with the value of normal stress obtained from the statics calculations, and were close: $1.14 \times 10^8 \frac{N}{m^2}$ (2,380,943psf) was the resultant calculation value and $-1.149 \times 10^8 \frac{N}{m^2}$ (-2,380,943psf) was shown in blue in regions near the purlins in the simulation. Opposite signs are likely due to differences in sign conventions used in the calculations and by the simulation software. Normal stress calculations for the remaining members that form the upper chord of the truss are expected to produce similar stresses since the procedure used in the hand calculations assumes equivalent loads from the purlins acting at the nodes of the truss, and the cross-sectional area of the members is the same. This is in agreement with the pattern of the blue regions on the contour in Figure 29 below.

This process was repeated to validate the results of the static simulations conducted on the steel angle model, and is also detailed in Appendix B. The order of magnitude for the normal stress shown on the contour in Figure 30 is $10^8$, which is in the same order of magnitude as the calculated value for normal stress detailed in Appendix B.
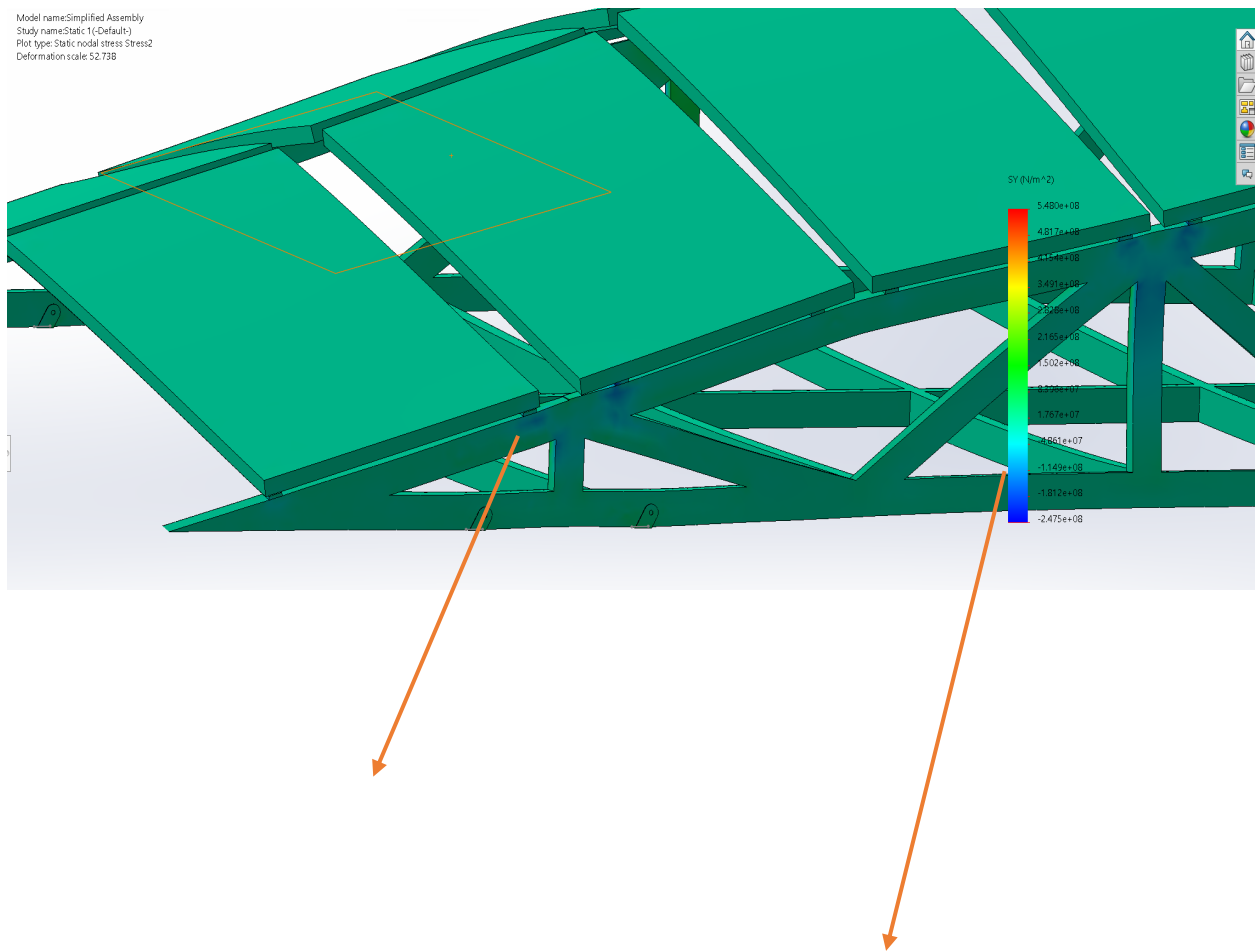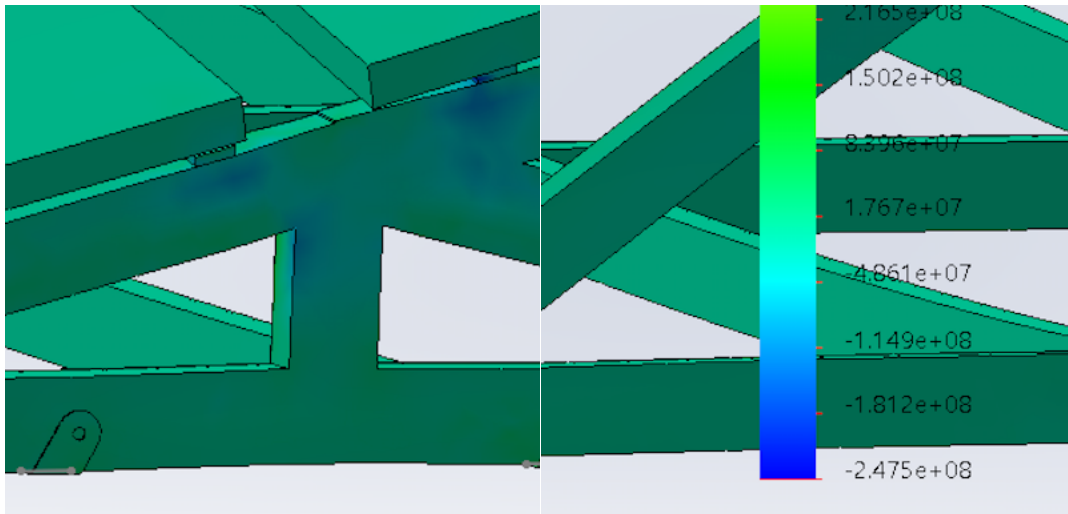
**Figure 29. Contour of normal stresses in the y-direction for the 55psf wind loading case.** Regions of the trussing constructed of hollow rectangular sections in close proximity to the purlins' contact points show areas of stresses with values close to $-1.149 \times 10^8 \, \frac{N}{m^2}$.
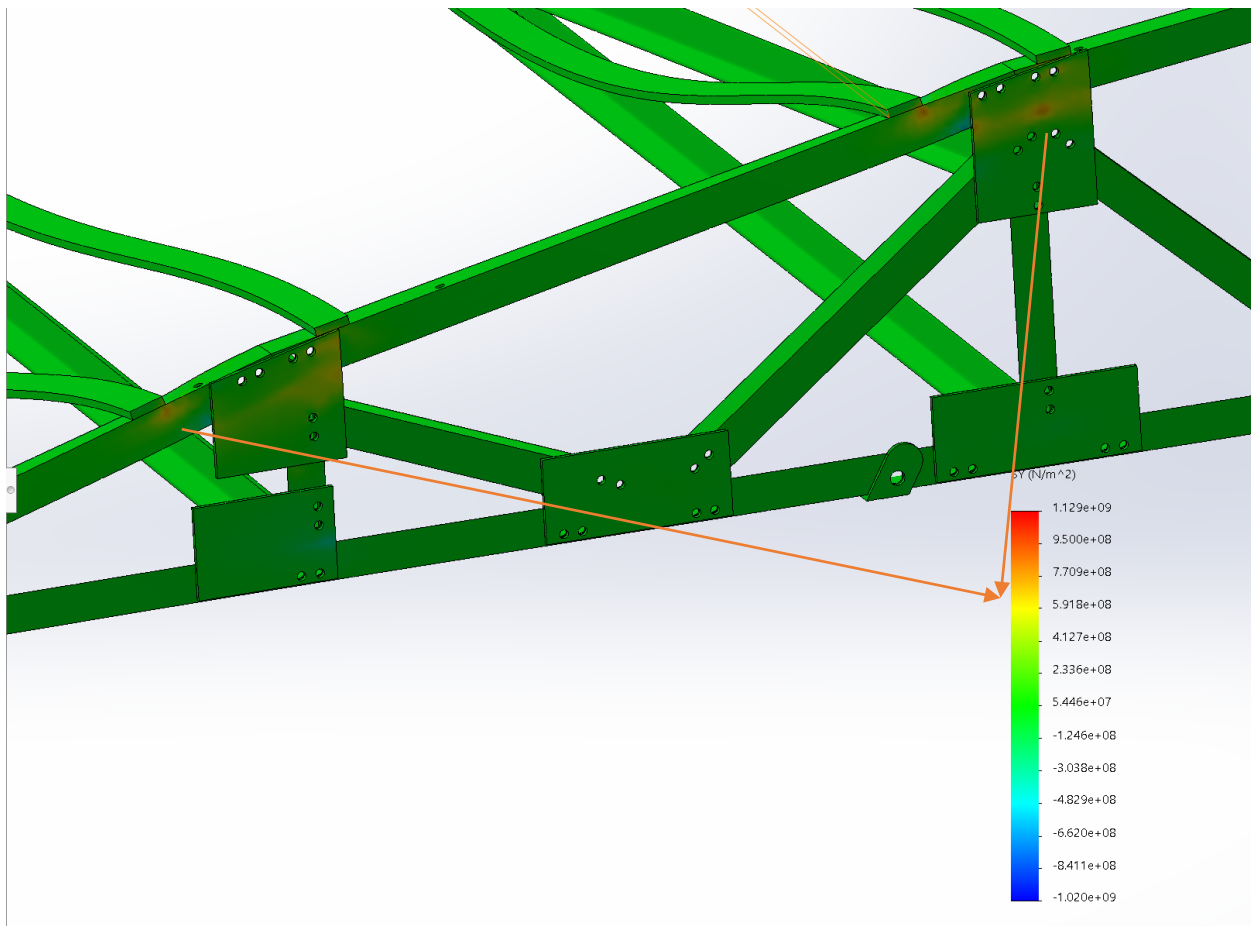
**55psf wind loading case.** Regions of orange indicated by the arrows in Figure 9 show stresses in with values in the $10^8$ order of magnitude on the trussing constructed of steel angle. This is in the same order of magnitude as the resultant value from the statics calculation detailed in Appendix B.

## 6.2 Seismic Simulation

Response spectrum analysis within a linear dynamic study in SOLIDWORKS was used to assess the durability of the racking under seismic vibrations. This type of study is used in seismic simulations used to assess buildings and other structures; it was therefore deemed appropriate to use with for the seismic analysis for the Superway's racking.

### 6.2.1 Boundary Conditions and Applied Loads

Fixtures were applied on the lower face of the brackets to mimic the racking's connections on the guideway. A base excitation was defined in the loads; this particular type of load was selected since it shakes the model from the base upward, which mimics the behavior of a seismic event. Within this base excitation, response spectrum data consisting of time versus acceleration from the 1940 El Centro earthquake of magnitude 6.9 was imported into the load definition. Since the response spectrum was of acceleration, the corresponding option was selected within the base excitation and a value of $1 \frac{m}{s^2}$ was defined for the x-coordinate; this is done to specify the direction in which the software is to excite the structure; only one coordinate can be excited per run of the simulation. Therefore subsequent runs of this simulation involved changing the excitation definition to the y and z directions. The frequency was run before solving the study in each case to ensure the model would be adequately excited by the imported response spectrum.

### 6.2.2 Mass Participation

As previously stated in section 4.3.2, the effective mass participation factor needs to meet a threshold of 0.8 or 80% in the direction of excitation once the frequency has been run on the model. This ensures that the model is being adequately excited in the specified direction; enough modes need to be included in the study to meet this threshold. Several runs of this simulation involved adjusting the number of modes (simply called "frequencies" in Solidworks) to get close to this threshold in each excitation direction. The number of modes ranged from 15 for the initial study to 300. The cumulative mass participation factor using the El Centro response spectrum, excitation in the x-direction, and 300 modes is shown in Figure XX below as a representation of what this looks like in the software. The cumulative effective mass participation factor was close to the threshold of 0.8 as seen below.

| Mode No. | Freq (Hertz) ▼ | X direction | Y direction | Z direction |
|---|---|---|---|---|
| 278 | 301.38 | 2.3091e-06 | 0.00035923 | 5.2223e-08 |
| 279 | 302.83 | 1.97e-05 | 0.00010693 | 1.6798e-07 |
| 280 | 304.25 | 0.0033552 | 0.00057907 | 1.305e-06 |
| 281 | 307.06 | 0.00042735 | 4.4525e-06 | 0.00012452 |
| 282 | 307.39 | 3.6647e-05 | 1.2244e-05 | 0.00047317 |
| 283 | 311.22 | 0.001422 | 7.0908e-06 | 3.054e-07 |
| 284 | 311.59 | 0.0024766 | 6.7699e-07 | 4.0464e-06 |
| 285 | 313.1 | 1.7361e-05 | 4.3415e-05 | 7.1225e-06 |
| 286 | 314.14 | 5.3145e-06 | 7.7398e-07 | 0.0002018 |
| 287 | 315.21 | 2.7409e-05 | 3.9282e-07 | 3.8351e-05 |
| 288 | 315.47 | 2.6604e-07 | 2.807e-07 | 1.612e-05 |
| 289 | 316.77 | 0.00011061 | 3.7778e-08 | 4.7219e-08 |
| 290 | 318.26 | 0.00038461 | 0.00021468 | 1.1834e-06 |
| 291 | 318.88 | 7.3491e-07 | 8.1468e-07 | 0.00042521 |
| 292 | 322.37 | 0.0060528 | 4.8311e-05 | 1.0748e-05 |
| 293 | 322.64 | 0.001606 | 9.3806e-06 | 2.3681e-05 |
| 294 | 328.59 | 2.9865e-06 | 1.3865e-06 | 0.00011783 |
| 295 | 329.33 | 0.00026459 | 6.0444e-05 | 3.2045e-06 |
| 296 | 329.83 | 6.7772e-07 | 6.045e-07 | 3.3436e-05 |
| 297 | 330.91 | 0.0011516 | 2.2997e-05 | 2.6255e-10 |
| 298 | 332.76 | 0.00031776 | 6.9831e-05 | 1.9108e-07 |
| 299 | 334.76 | 9.7582e-08 | 1.6609e-10 | 9.9423e-07 |
| 300 | 335.78 | 2.5649e-08 | 2.7508e-09 | 1.1131e-05 |
| | | Sum X = 0.75414 | Sum Y = 0.96524 | Sum Z = 0.97714 |

**Figure XX. Cumulative Effective Mass Participation Factor in Solidworks.** For excitation in the X-Direction, the cumulative mass participation factor can be seen to be close to the threshold of 0.8 when 300 modes are defined in the study with the El Centro data defined within the base excitation.

## 6.1.5 General Simulation Tips for the Current Steel Angle Model :

Simulation guides and Solidworks documentation provided several helpful tips that were used to workaround simulation errors. These tips have been described in detail in section 4.3.1 of the literature review above. Some particular tips were also developed to successfully simulate on the current steel angle model are listed below to provide some additional guidance or solutions to commonly encountered errors.

1. Generate mesh on all parts manually BEFORE running the full study and ensure that a mesh has been generated on each part. This will help ensure that members do not disappear in the simulation results.
2. Mesh size will need to be adjusted manually as opposed to generating an automatic mesh on the model. A relatively fine mesh size within the simulation study will need to be defined for the L-channels; 15mm was found to generate a mesh on all L-channels.

3. Generate a curvature based mesh on parts with a failed mesh through the manual mesh generation options in Solidworks.
4. Simplification is necessary and highly recommended. Local contact sets provide a simplified means of simulating on the model without having to include connection hardware. The results for stress and displacement have almost insignificant differences according to simulation guides with less errors to work around and more reasonable computation times. As opposed to the global bonded contact which is default in Solidworks, local bonded contact sets at the corresponding edges of bolt holes with no penetration contacts between the interfacing parts are recommended.
5. Use the contact visualization plot tool to make sure that all members are connected together with contact sets defined as intended. This can eliminate issues that could cause the solver to fail or produce unrealistic results with the parts flying off.
6. If a "Solver Failed" error message shows up, there is likely a meshing error. Go back to the meshing step and ensure that a mesh has been generated on all parts being included in the model.
7. It may be necessary to enable the large displacement option in study properties for more accurate results. Instead of applying the maximum load at once as done in a typical study, the large displacement model ups the load in increments up to the specified value and records the results at each load step.
8. For the linear dynamic study used for the seismic simulations, disable the setting labeled "soft spring to stabilize model" in the study properties, which can be accessed by left-clicking the study name in the study tree. This will prevent final results from looking like nothing is happening in the simulation and solver errors.
9. When importing a response spectrum into the base excitation within the linear dynamic study, ensure that the proper type of excitation is selected that corresponds to the type of data being used. In other words, if the data is of acceleration, define the excitation direction (x, y, or z) as an acceleration. The other options available are velocity and displacement. Excitation can only be defined in one direction (x, y or z) at a time.

## 7. Discussion of Results

### 7.1 Simulation Results on HSS Model

Regions of high stress on the trussing with values near $1.327 \times 10^8 \frac{N}{m^2}$ are shown in green in Figure 30. These areas of high stress are in the proximity of connections to the purlins and the brackets as seen in Figure 30, which is in agreement with the expected load path from panels to purlin to truss during uplift. For the critical wind loading pressure of 55psf, all elements of the canopy meet a factor of safety of two against yield, as shown in Figure 10 of Appendix D.

Several runs of the simulation with the pressure on the underside of the panels changed to match the corresponding ASCE wind pressure were run to calculate reactions at the interface between the brackets and bridges on the guideway. These reactions increase in an exponential pattern as seen in the plot for force in the y-direction in Figure 26, which corresponds to the direction of uplift. All reactions increased with wind speed; maximum values for these reactions corresponded to the maximum wind speed of 150mph with values of 8,780N for the reaction force in the y-direction and 335N.m reaction moment around the

Z-axis, seen in Table 4. This means that a complete load path from the panels to the purlins to trussing to the guideway is formed since the loads are transferred throughout the structure to the brackets to resist uplift; this is in accordance with the proper transfer of loading specified for roof mounted arrays. However, this also necessitates changes to cross-sections of critical components such as the brackets to achieve a higher factor of safety for greater reliability.
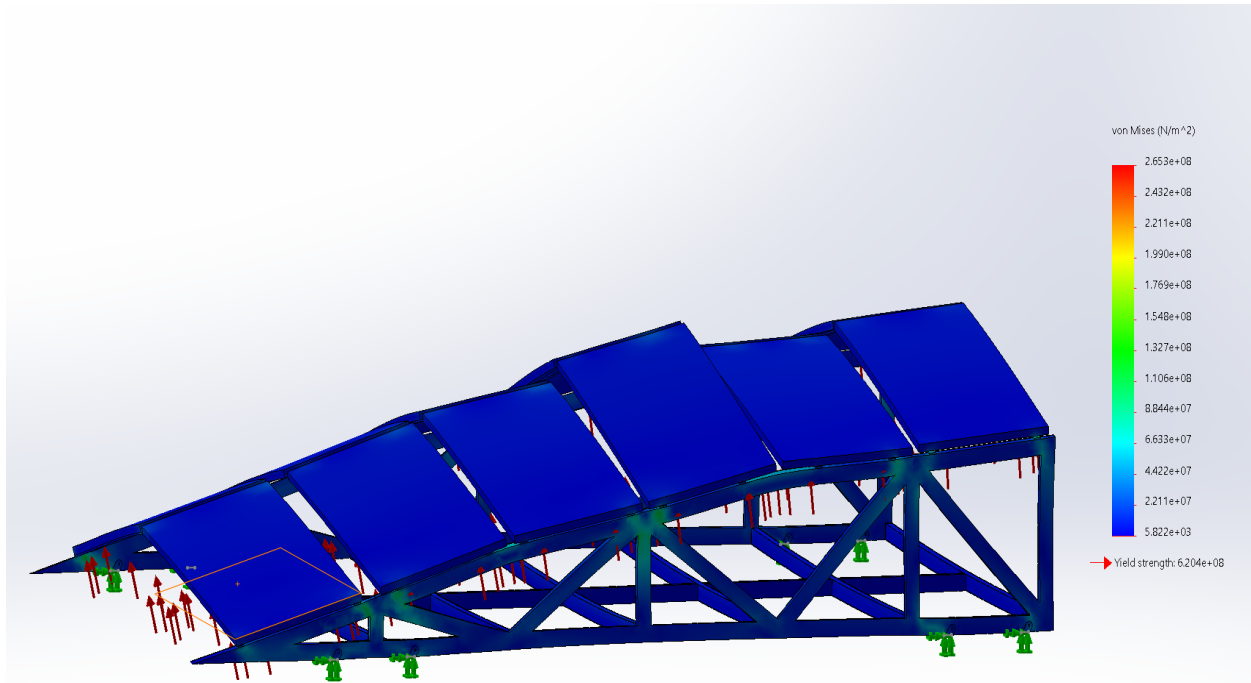


**Figure 30. Stress contour of the HSS canopy for the critical 55psf wind loading.** Regions of higher stress (shown in green) appear where the purlin connects to the side trusses and near the brackets fixing the mounting to the guideway.

| Wind Speed (mph) | Fx (N) | Fy (N) | Fz (N) | Mx (N.m) | My (N.m) | Mz (N.m) |
|---|---|---|---|---|---|---|
| 20 | 123 | 148 | 61.8 | 4.46 | 4.28 | 5.66 |
| 40 | 493 | 591 | 248 | 17.8 | 17.2 | 22.6 |
| 60 | 1110 | 1330 | 556 | 40.2 | 38.6 | 50.9 |
| 80 | 1970 | 2370 | 989 | 71.3 | 68.8 | 90.5 |
| 100 | 3080 | 3700 | 2960 | 112 | 107 | 141 |
| 120 | 4440 | 5320 | 2230 | 160 | 155 | 203 |
| 140 | 6040 | 7240 | 3020 | 219 | 210 | 277 |
| 150 | 7320 | 8780 | 3660 | 263 | 255 | 335 |

**Table 6: Maximum Reactions Across the Brackets at Connections to Guideway Bridges for Increasing Wind Speed**. Reactions at the center point of the face of the brackets in contact with bridges on the guideway for wind speeds ranging from 20-150mph acting on the canopy. 150mph is the maximum wind speed in the United States specified by ASCE, corresponding to the worst case uplift pressure of 55psf. Plots of the minimum, maximum, and average forces across the brackets are included in Appendix C.
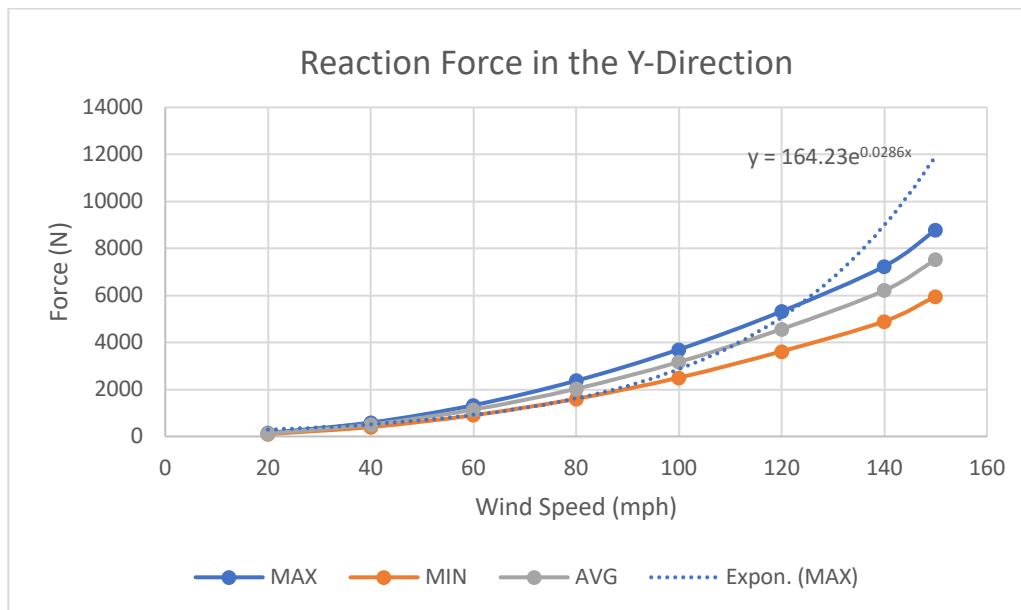


**Figure 31. Reaction Forces in the Y-Direction (Direction of Uplift)**. Reaction forces on the underside of the brackets increase in a nearly exponential pattern as indicated by the dotted trendline. Plots of other reaction forces are included in Appendix C.

## 7.2 Wind Loading Simulations on the Current Steel Angle Model

In the initial simple globally bonded simulations, stress concentrations appeared at central regions of the members instead of at the actual bolted connections. Views of the stresses on a representative section of the trussing from the globally bonded study are shown in <mark>Figure XX</mark>; stress concentrations appear offset from the actual connection points. This can be attributed to the way the software interprets this type of contact set. Global bonding makes the software assume that the parts are essentially glued together across their entire intersecting faces, so the load is transferred to a less rigid central region of the angle member away from the connection point and higher stresses correspondingly appear there.
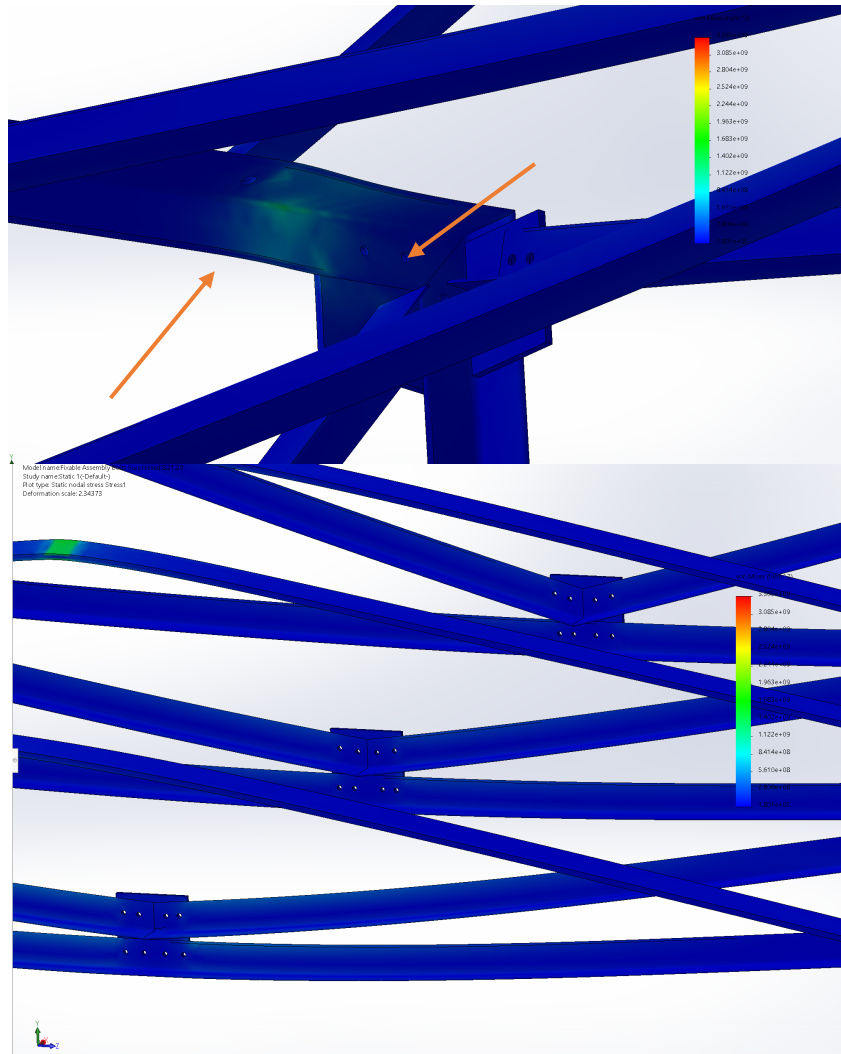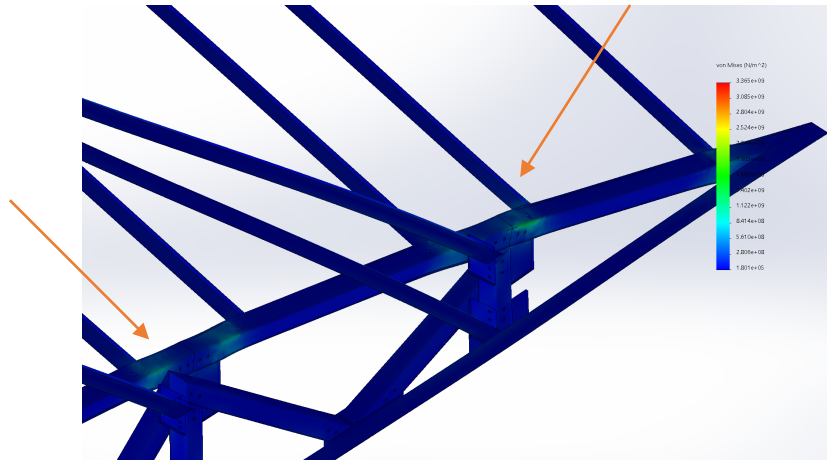
Figure XX. Resulting stresses on the Racking with the Globally Bonded Contact Definition. As indicated by the regions of neon green on the angle members indicated by the orange arrows, stresses appear offset from the connection points with the globally bonded contact definition.

In subsequent refinements to the simulation, local contact sets were defined at each bolt hole to more closely mimic bolted connections as recommended by the simulation guide. Bonded contact sets between the corresponding edges of each bolt hole were defined to reduce the geometry the software assumed was bonded together; rather than an entire face of a member bonded to a gusset plate, only the corresponding bolt holes were bonded together. No penetration contact sets were also defined at each bolt hole to ensure that the model did not assume that the geometries were allowed to deform into each other; rigid interfaces between each part were required to more closely mimic the actual bolted connections.

Results for the 55psf uplift loading case with the refined contact sets shows stress concentrations in the vicinity of the bolt holes, which is more aligned with expected results. General views of the stress and displacement contours are shown in Figure XX of Appendix D. Maximum displacements appeared at the middle of the simplified Z-purlins. The regions of high stress appear at the bolting sites of the Z-purlin and translate downward to the bolted connections between the steel angle members of the truss as seen in Figure XX below. Stress concentrations also appear at connections between the diagonal bracing and the lateral base members, as shown in Figure XX.
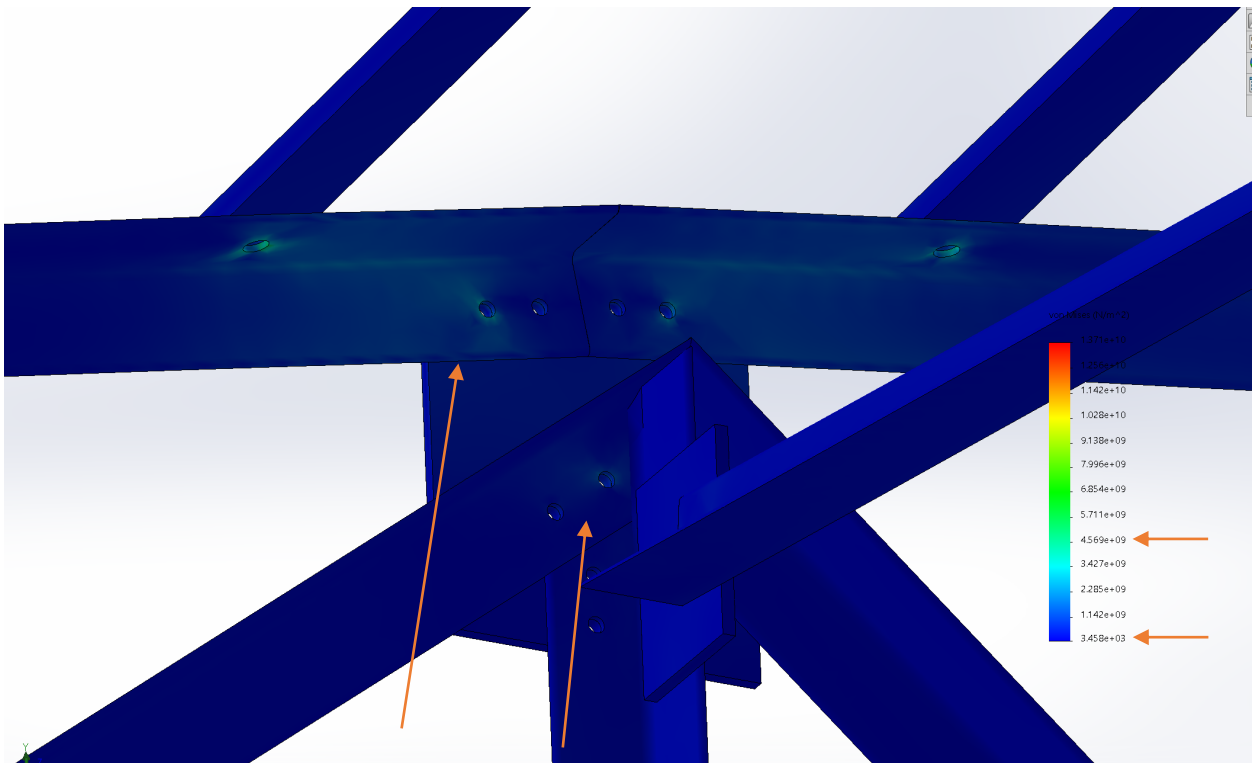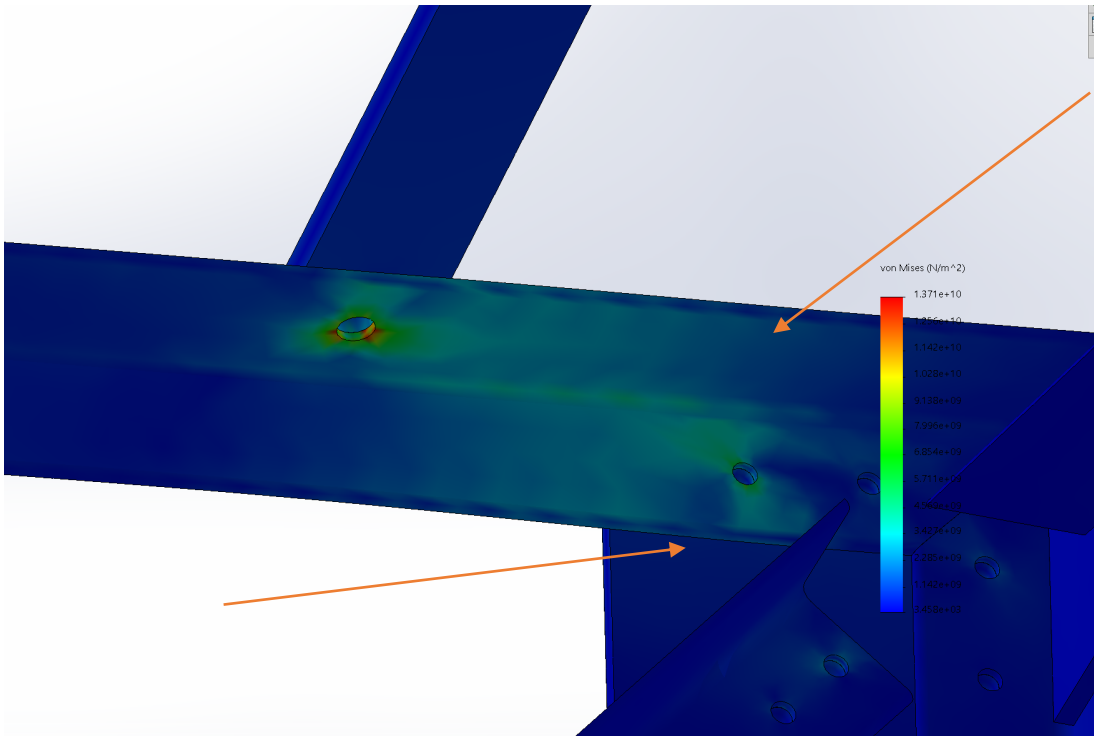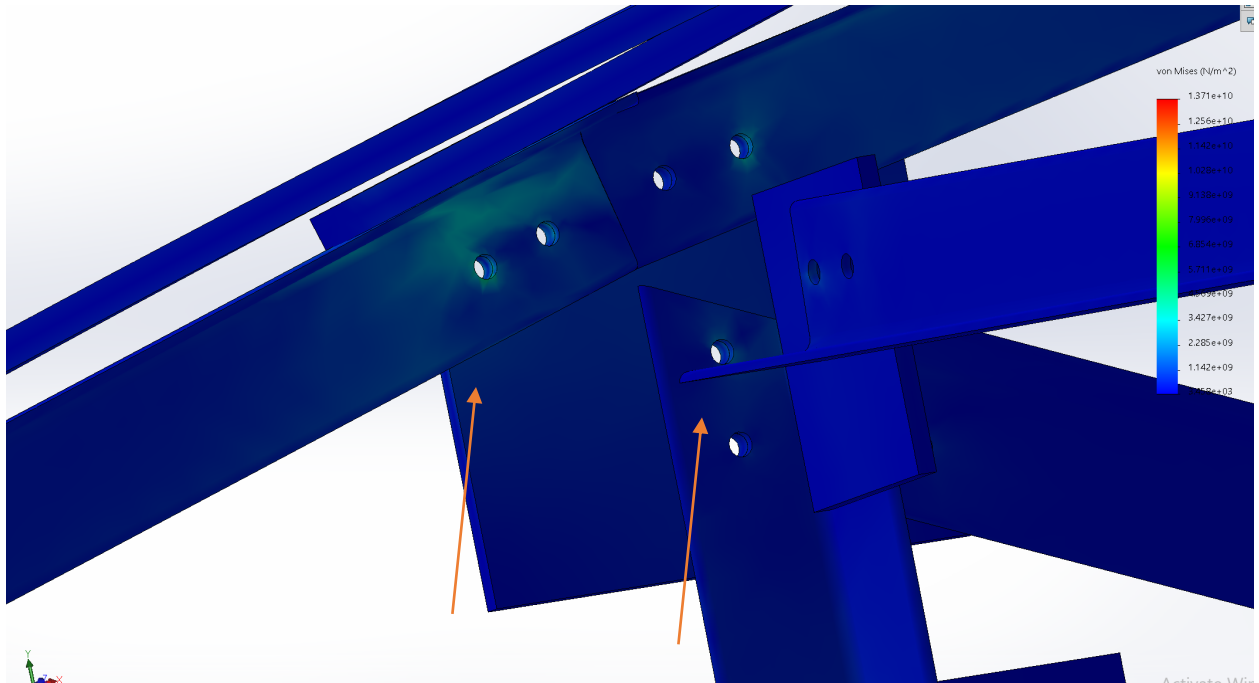
Figure XX. Stresses with the Refined Local Contact Sets from Purlins to Side Trusses. Stress concentrations appear at the bolt holes rather than offset from the connection points as in the globally bonded study. These stress concentrations appear near the connections to the Z-purlin and move down to the connections between the angle members as shown in the figures above.



Stresses with Globally Bonded Contact Set
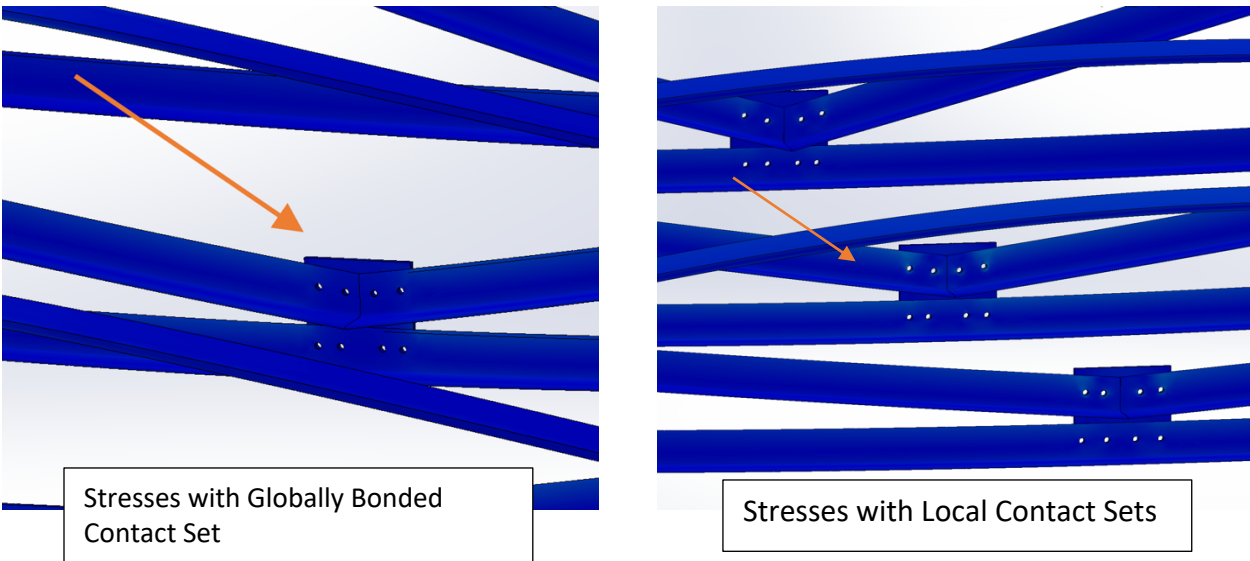
Stresses with Local Contact Sets

Figure XX. Stresses with Refined Local Contact Sets at Connections between the Diagonal Bracing and the Lateral Base Members. Stress concentrations now also appear at connections between the diagonal bracing and base members as shown on the right; these stress concentrations were not seen in previous results from the globally bonded study as shown on the left.

The maximum stress for the uplift simulation was $1.371 * 10^{10}$ $\frac{N}{m^2}$ and appears at a bolt hole between the upper chord of the truss and the lower-most Z-purlin as seen in the first image of <mark>Figure XX</mark> above; this may be due to a singularity in the mesh since the connections between other purlins and the truss and with the same loading do not exhibit this maximum stress value. The other stress concentrations shown in neon green at connections throughout the model are close to $4.569 * 10^{9}$ $\frac{N}{m^2}$ in value. A contour of the factor of safety against yield was defined within the results of the same study and is shown in Figure XX below. The contour appears to indicate factors of safety against yield well above the required value of two throughout the model indicated by the medium grey color as shown in Figure XX. However, to verify these factor of safety results simple hand calculations were carried out with the stress values seen throughout a majority of the model indicated in dark blue of $3.458 * 10^{3}$ $\frac{N}{m^2}$ and of $4.569 * 10^{9}$ $\frac{N}{m^2}$ seen at the neon green stress concentrations using the yield strength for A36 steel angle detailed in Table 1. The model has high values of factor of safety for the regions indicated in dark blue and comfortably surpasses the threshold value of 2. However, the factor of safety is quite low using the concentrated stress value, as indicated in the calculation on the next page. Therefore, these calculations indicate that the factor of safety contour produced by the simulation results are misleading. A larger size of the angle members will need to be implemented to achieve the desired factor of safety.
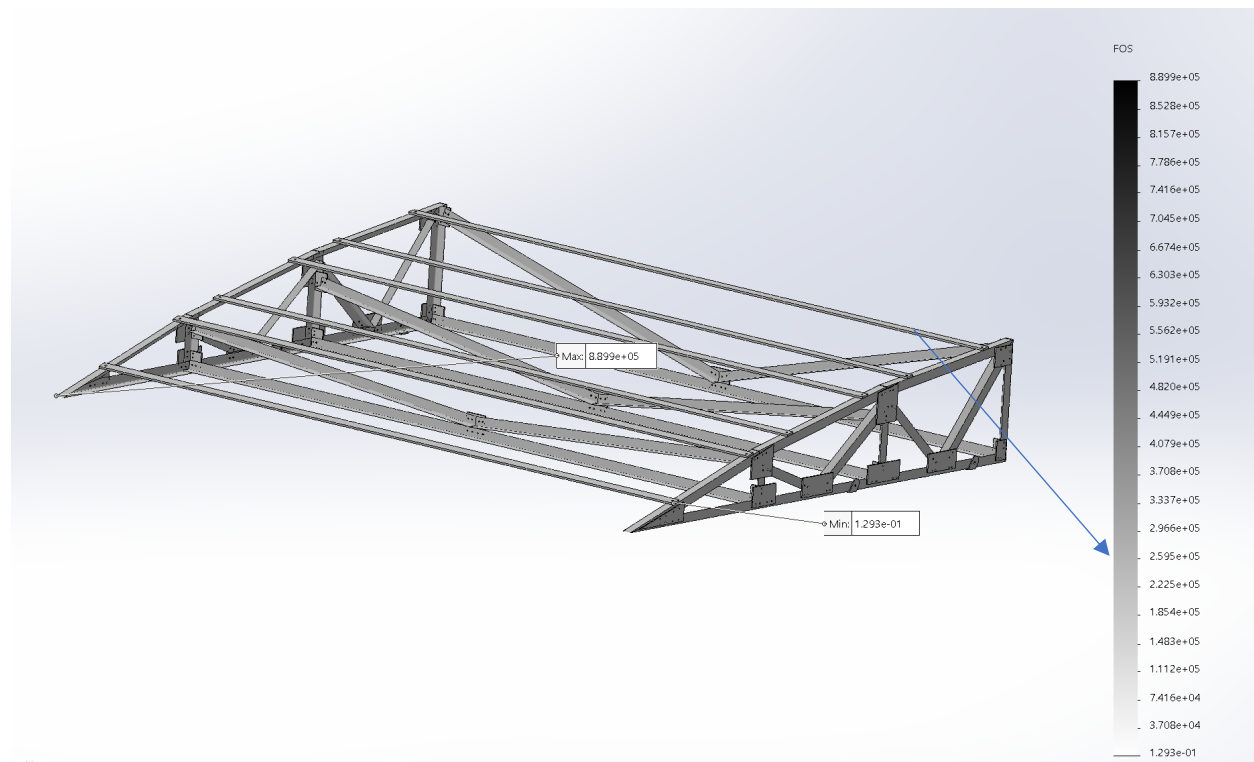


Figure XX. Factor of Safety Against Yield Contour for the 55psf Loading Case. A contour of the factor of safety against yield was defined within the results for the simulation with local contact sets used to assess the structure's behavior under this loading. The minimum value corresponds to

the maximum stress at the edge of the bolt hole shown in the first image of <mark>Figure XX</mark> above, which is thought to be attributable to a singularity in the mesh. The rest of the model appears to have a FOS of $2.595 * 10^5$ against yield as indicated by the blue arrow.

$$FOS_{yield} = \frac{Yield\ Strength}{Working\ Stress}$$

For the regions in dark blue:

$$FOS_{yield} = \frac{250 * 10^6\ Pa}{3.55 * 10^3\ Pa}$$

$$FOS_{yield} = 7.04 * 10^4$$

For the regions in neon green (stress concentrations):

$$FOS_{yield} = \frac{250 * 10^6\ Pa}{4.57 * 10^9\ Pa}$$

$$FOS_{yield} = 5.47 * 10^{-3}$$

The simulation was also conducted with the equivalent loads from 55psf of uplift on the solar panels modified to act in the opposite direction on the purlins to assess the viability of the structure under compressive loads. General views of the stresses and corresponding displacements for this study are shown in Figure XX of Appendix D. Maximum displacements were near the center of the simplified Z-purlin. Stress concentrations appear in similar patterns to the uplift loading case at connections throughout the trussing as shown in Figure XX.
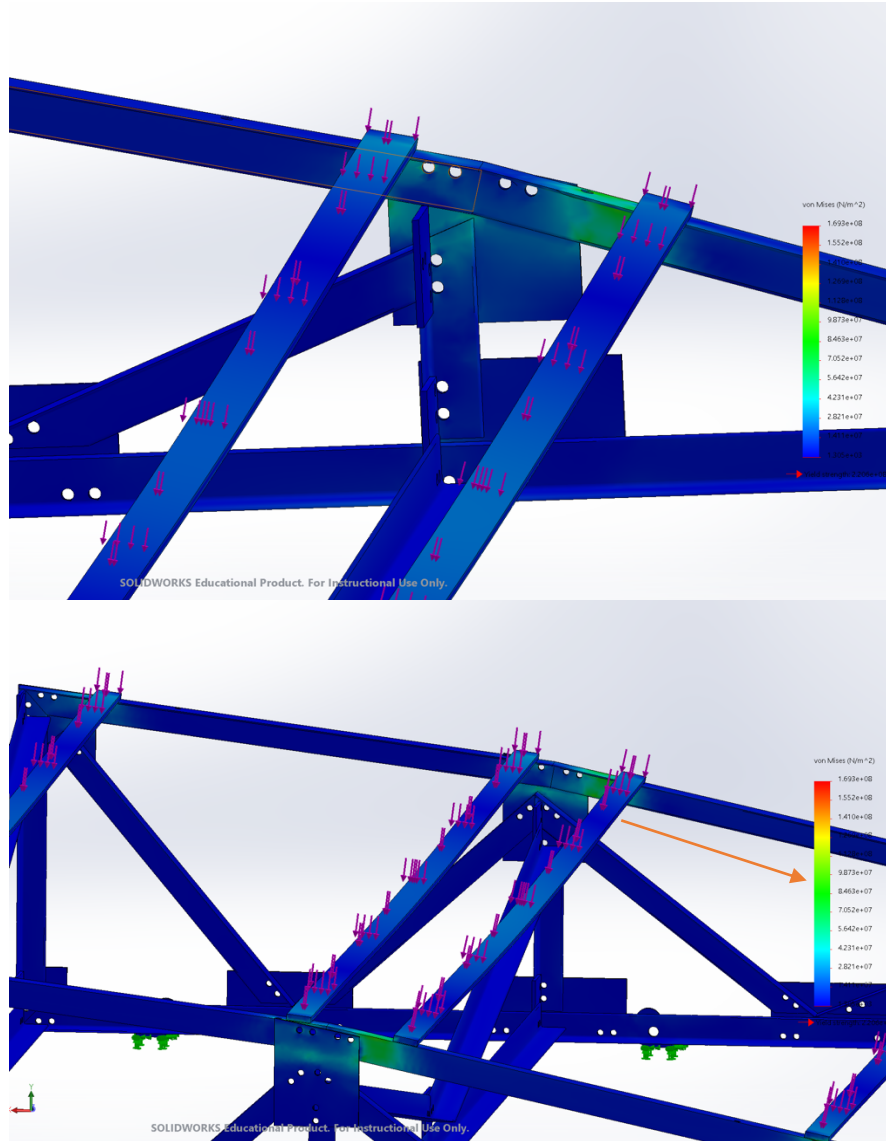
Figure XX. Stress Concentrations at Connections for the Compression Loading Case. Stress concentrations for the 55psf compression loading case also appear at the connections between the members in similar patterns to the uplift loading case. These are in the $10^7$ order of magnitude as indicated by the arrow. General views of the stress and displacement contours are included in Appendix D.

## 7.3 Seismic Simulations Results for the Current Steel Angle Model

The results of the seismic simulation indicate that the structure is capable of withstanding seismic excitation corresponding to a magnitude 6.9 earthquake as detailed in section 6. Representative

stress and displacement contours with the excitation defined in the Z-direction are shown in Figure XX below. Additional result contours can be found in Appendix D.
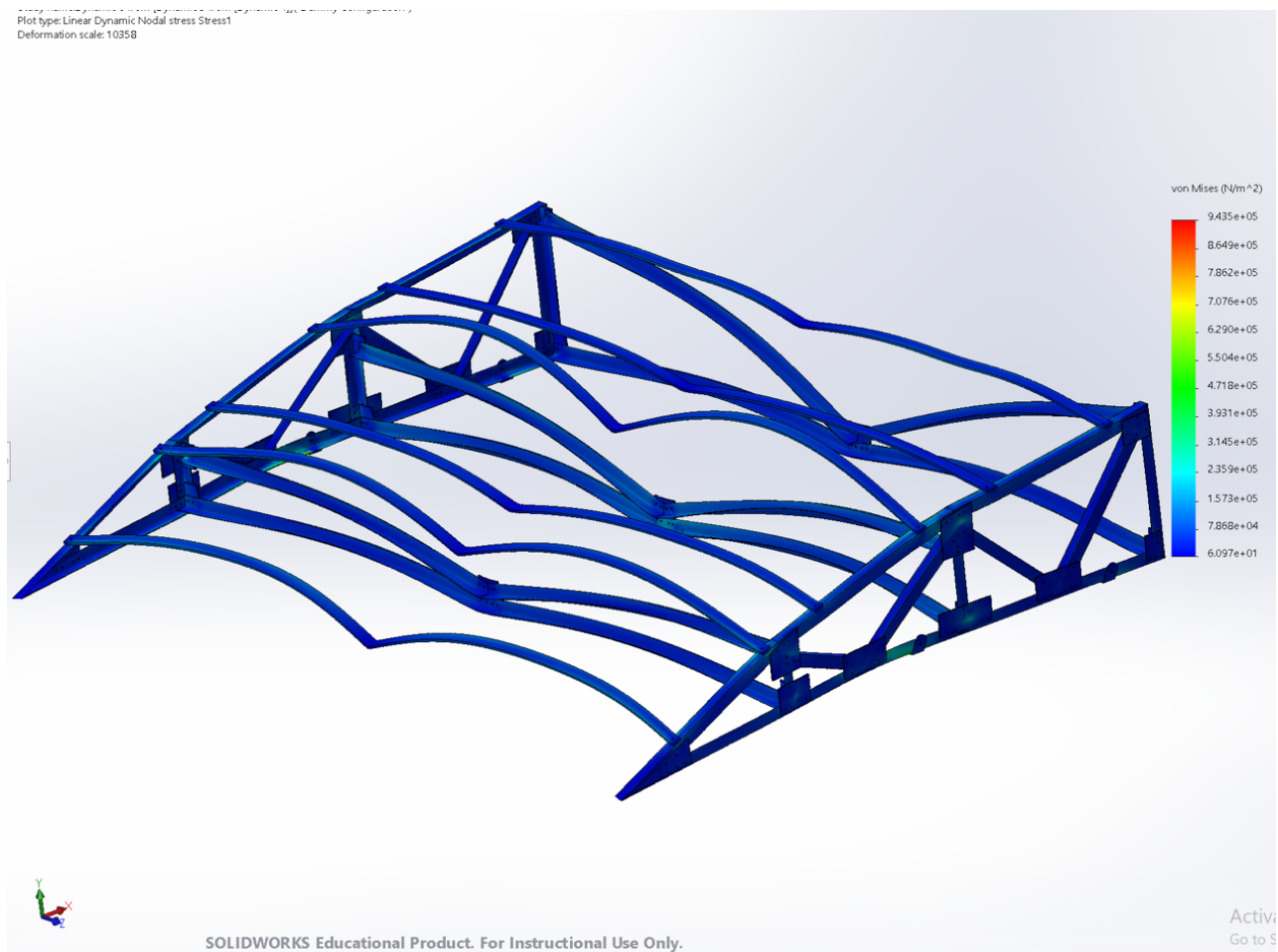
**Figure XX. General Stress Distribution on Model with Excitation Defined in the Z-direction.** A view of the resultant stress distribution in the model for excitation in the Z-direction with the response spectrum for the magnitude 6.9 El Centro earthquake. Stress concentrations appear at the connection points and are in the $10^5$ order of magnitude.
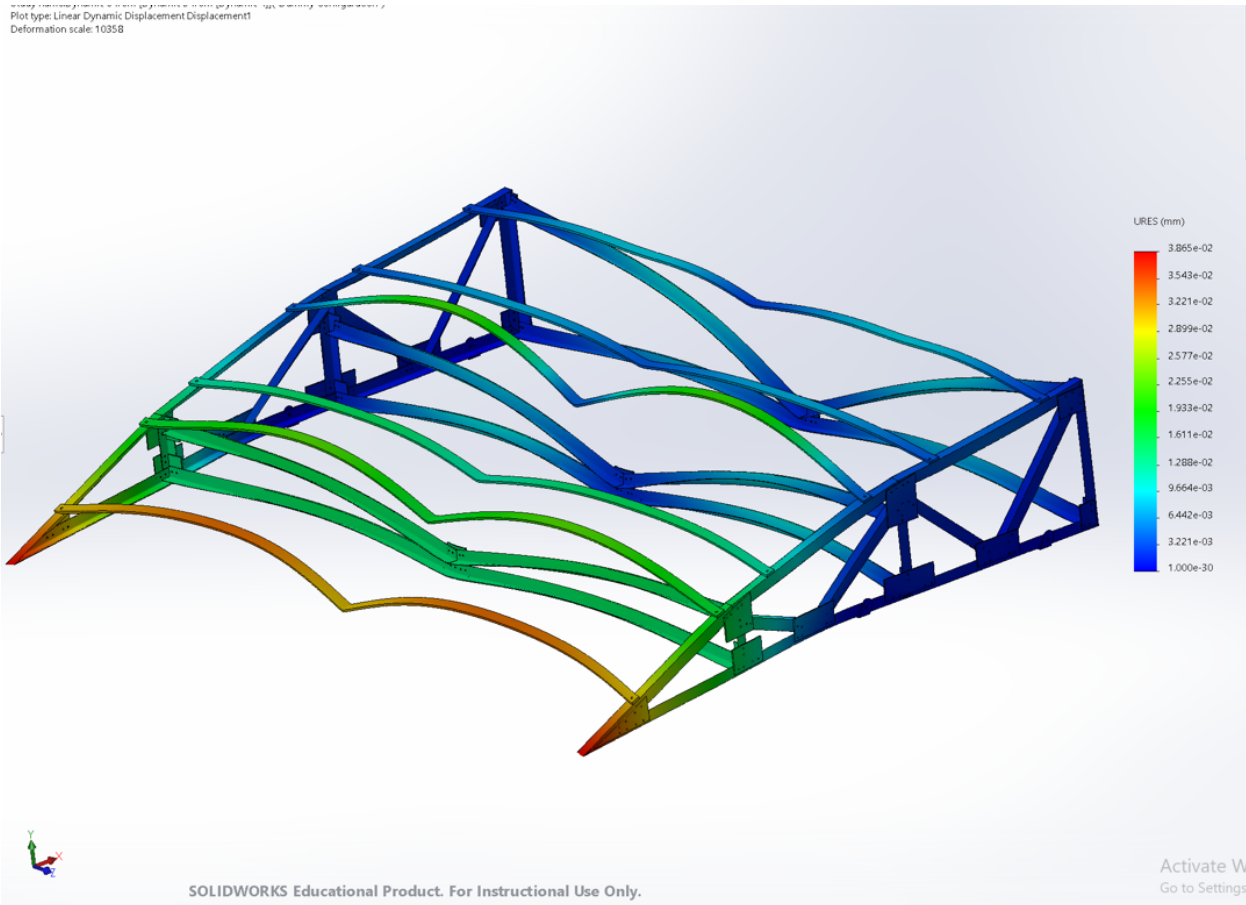
**Figure XX. Displacement Distribution with Excitation Defined in the Z-direction.** A view of the resultant stress distribution in the model for excitation in the Z-direction with the response spectrum for the magnitude 6.9 El Centro earthquake. Maximum displacements occur at the middle of the Z-purlin and at the front edge of the canopy of close to of $3 * 10^{-2}$ $mm$.

## 8. Conclusions and Recommendations for Future Work

In conclusion, the current design for solar mounting made of A36 steel angle is considered viable with modification. This design does meet several central requirements stipulated for the canopy including the capability to mount directly onto the Superway's guideway, install in a streamlined manner using bolts, allows for efficient panel installation, provides accessibility for maintenance of individual modules, and facilitate rainwater harvesting. Material use is minimized without sacrificing structural reliability through the use of steel angle sections to construct the trussing foundation, which also helps minimize aesthetic intrusiveness and provides durability against insects and other environmental conditions.

Although a majority of the length of each member appears to exceed the factor of safety of two for both the 55psf uplift and compression loading cases, connection points do not meet this factor of safety due to high stress concentrations at these locations. To satisfy the factor of safety

61

requirement, future iterations of the design can be modified with the trussing constructed from dimensionally larger A36 L-channels of greater thickness, which will reduce the working stress concentrations and therefore increase the factor of safety. Another consideration is that 55psf of wind loading may not be the best design load to consider for the Superway's solar canopy that will be located in San Jose, which will likely see maximum wind loads of 24psf as calculated using the same ASCE methodology. In other words, designing the canopy to withstand 55psf is possible, but may prove impractical with the canopy mounted on top of the guideway. Tradeoffs between the design strength and practicality for this application will need to be considered; a bulkier racking structure that does satisfy the strength requirements may not meet other important requirements including aesthetics, mountable on top of the guideway with the guideway as the primary supporting structure, and cost requirements. An independently supported canopy may be required instead.

Several recommendations for future work have been identified. As mentioned above, working stresses at the connection points in the trussing can be reduced by modifying the current members to dimensionally larger and thicker steel angle members that may help the model satisfy the factor of safety for the 55psf wind loading cases at these locations. Furthermore, the dimensions of the current members may be adjusted to more whole values by modifying the dimensions of adjacent members to meet at the gusset plates without mitered edges; this will make the design more practical to manufacture. There is also more headway to be made with the simulations used to assess the model. Although the connections in the simulation results presented in this report very closely mimic the behavior of bolted connections, simulation results with the actual bolts, washers, and nuts present will provide a second layer of confirmation that the proposed hardware will be able to reliably hold the model up. When a simulation is successfully run with the connection hardware present, Solidworks is capable of classifying the bolts and other hardware into two separate folders by ones that can withstand the loadings and the ones that cannot. Next, an adaptation of the canopy for curved sections of guideway will also need to be designed; a potential way of accommodating curves may be possible by angling the units of trussing along the curvature of the guideway, which can then support purlins to mount modules on. Lastly, though the model has been assessed with the response spectrum for a magnitude 6.9 earthquake, it may be conservative to repeat the simulations with the response spectra for a higher magnitude earthquake to ensure structural reliability under more extreme seismic conditions.

## 8. References

Axinte, E., Văsieş, G., Teleman, E. C., Roşea, V. E., & Axinte, A. O. (2015). INCLUDING SOLAR PANELS ON PARKING AREAS IN THE SUSTAINABLE DEVELOPMENT CONCEPT. WIND EFFECTS. *Environmental Engineering & Management Journal (EEMJ)*, *14*(9).

Baetu, G., Teleman, C. E., Axinte, E., & Rosca, V. E. (2013). Numerical Simulation of Wind Action on a Solar Panels Array for Different Wind Directions. *Buletinul Institutului Politehnic din lasi. Sectia Constructii, Arhitectura*, *59*(4), 9.

Cano, J., Tamizhmani, G., Madakannan, C., & Macia, N. (2014). Photovoltaic modules: Effect of tilt angle on soiling. *2014 IEEE 40th Photovoltaic Specialist Conference, PVSC 2014,* doi:10.1109/PVSC.2014.6925610

Design of steel footbridges . Retrieved from https://www.steelconstruction.info/Design_of_steel_footbridges

Fabian, L., Furman, B. Ph.D., Ellis, S., Muller P., & Swenson R. (2014). *Automated transit networks (ATN): A review of the state of the industry and prospects for the future.* ().Mineta Transportation Institute. Retrieved from https://transweb.sjsu.edu/sites/default/files/1227-automated-transit-networks.pdf

Futran, n.d.

Furman, B. (July 10, 2016). The Spartan Superway: A Solar-Powered Automated Transportation Network. Paper presented at the *ASES National Solar Conference 2016,* 1-10.

Genmounts | Renewable Energy Holdings, 97 River Road 2 Floor, Flemington, N. 0., & T: 908-788-7750 | F: 908-837-9021.*Genmounts vector 1.0 (1 column) post driven installation manual*

Griggs, F. (2015, July 1,). The warren truss ., 1-2. Retrieved from https://www.structuremag.org/?p=8715

Hbahn21. (2020). Retrieved from https://h-bahn.info/en/technology/vehicles-h-bahn/

Hickey, K. (2018). Understanding differences in welding steel vs. aluminium. Retrieved from https://www.ahssinsights.org/news/understanding-differences-in-welding-steel-vs-aluminium/

Hollow sections for structural and mechanical application. (2013). Retrieved from https://www.tatasteeleurope.com/file_source/StaticFiles/Business_Units/Corus_Tubes/Tubes/TST01_Overview_Brochure_NH_update.pdf

Maffei, J., Telleen, K., Ward, R., Kopp, G. A., & Schellenberg, A. (2014). Wind design practice and recommendations for solar arrays on low-slope roofs. *Journal of Structural Engineering*, *140*(2), 04013040.
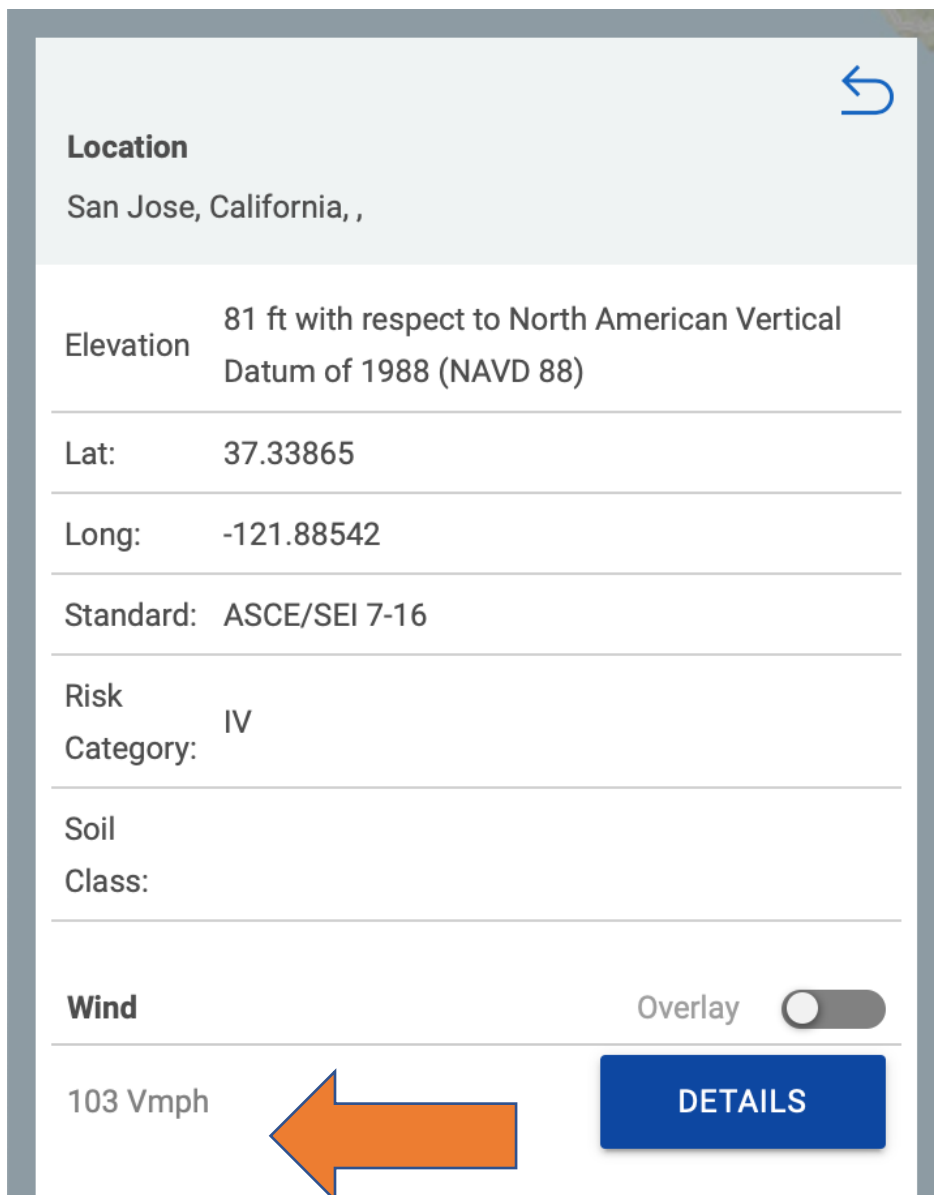
Matasci, S. (2018). What is the average solar panel size and weight? Retrieved from https://news.energysage.com/average-solar-panel-size-weight/

Mechatron.PV - clamp . Retrieved from https://mechatron.eu/products/hardware/clamp/

Nitzko, M., Geis, S., Rothfuchs, K., Schaller, S., Baumann, N., Lagaly, C., & Foster, S. (2011). *System for mounting an elevated solar installation* . Germany:

Perfection Architectural Systems. (2013). Solar panel support systems . Retrieved from http://www.perfectionarch.com/products/solar-framing.php

Powers Solar Frames.Powers super purlins . Retrieved from https://powerssolarframes.com/tech/flyers/0916/Powers%20Super%20Purlin%20090916.pdf

*Prefabricated steel bridge systems: Final report* . (2018). Retrieved from https://www.fhwa.dot.gov/bridge/prefab/psbsreport03.cfm

QuadPod long span canopy . Retrieved from https://questrenewables.com/products/surface-lot/

Messenger, R.A., & Ventre, Jerry. (2003). Mechanical considerations . *Photovoltaic systems engineering* (pp. 159-195) CRC Press.

Shademan, M., & Hangan, H. (2009, June). Wind loading on solar panels at different inclination angles. In *11th Americas Conference on Wind Engineering* (pp. 1-9).

Stathopoulos, T., Xypnitou, E., & Zisis, I. (2013). Wind-Induced Loads on Rooftop and Ground Photovoltaic Panel Systems. In *Proceedings of the Twelfth Americas Conference on Wind Engineering* (pp. 16-20).

STEEL BUILDINGS IN EUROPE
Single-Storey Steel Buildings
Part 5: Detailed design of trusses. (2008). In Arcelor Mittal, Peiner, Traeger & Corus (Eds.), (pp. 1-19) CTICM and SCI, Steel Alliance.

Steels, general properties . (2020). Retrieved from http://www.matweb.com/search/datasheet.aspx?MatGUID=034970339dd14349a8297d2c83134649

Truss bridges . (2019). Retrieved from https://www.ncdot.gov/initiatives-policies/Transportation/bridges/historic-bridges/bridge-types/Pages/truss.aspx

Trusses . Retrieved from https://www.steelconstruction.info/Trusses

Wind loads: General requirements . (2016). *ASCE 7-16 minimum design loads and associated criteria for buildings and other structures* (pp. 245-387)

**Appendices**

**Appendix A: ASCE Wind Loading Calculation**

The calculation of wind design pressures below is conducted using procedures specified in ASCE 7-16 *Minimum Design Loads and Associated Criteria for Buildings and Other Structures.*

1. **Determining Wind Speed for San Jose using ASCE Online Hazard Tool.** The risk category selected was IV for essential facilities, considering a transportation network such as the Superway a critical need. The standard selected was ASCE 7-16, resulting in a maximum wind speed of 103mph as indicated below.



**Figure 1: Determination of Maximum Wind Velocity in ASCE Online Hazard Tool (Maps of Wind Speed, from ("Wind loads: General requirements," 2016)).**

## 2. Calculation of Velocity Pressure involves Equation 1:

$$q = 0.00256(K_z)(K_{zt})(K_d)(V^2)(I) \qquad (1)$$

Where

$K_z$ is the velocity pressure coefficient at a height z
$K_{zt}$ is the topographical factor
$K_d$ is the wind directionality factor
$V$ is the basic wind speed in mph
$I$ is the importance factor

The following sections describe the calculation of each coefficient.

$\underline{K_z \text{ is the velocity pressure coefficient at a height z:}}$

The elevation z of the solar racking was calculated as the sum of the elevation of the guideway and the height of the guideway (1m):

$$z = \text{elevation of guideway} + \text{height of guideway} \qquad (2)$$
$$z = 20 + 3.28$$
$$z = 23.28ft$$

For $15ft \leq z \leq z_g$ :

$K_z = 2.01(\frac{z}{z_g})^{\frac{2}{\alpha}}$ where $Z_g$ and $\alpha$ are determined from Table 26.11-1 for Terrain Exposure:

Table 26.11-1 Terrain Exposure Constants

| | | | | | | | | | | |
|---|---|---|---|---|---|---|---|---|---|---|
| | | | | Customary Units | | | | | | |
| Exposure | $\alpha$ | $z_g$ (ft) | $\hat{\alpha}$ | $\hat{b}$ | $\bar{\alpha}$ | $\bar{b}$ | $c$ | $\ell$ (ft) | $\bar{\in}$ | $z_{min}$ (ft)$^a$ |
| B | 7.0 | 1,200 | 1/70 | 0.84 | 1/4.0 | 0.45 | 0.30 | 320 | 1/3.0 | 30 |
| C | 9.5 | 900 | 1/9.5 | 1.00 | 1/6.5 | 0.65 | 0.20 | 500 | 1/5.0 | 15 |
| D | 11.5 | 700 | 1/11.5 | 1.07 | 1/9.0 | 0.80 | 0.15 | 650 | 1/8.0 | 7 |

**Figure 2:** (Terrain Exposure Coefficients from ("Wind Loads: General Requirements", 2016))

Exposure Type B is appropriate since the Superway will be located in an urban setting.

Substituting 1200 for $Z_g$, 7.0 for $\alpha$, and 23 for $z$:

$$K_z = 0.649$$

$K_{zt}$ is the topographical factor that accounts for wind speed up over hills and ridges:
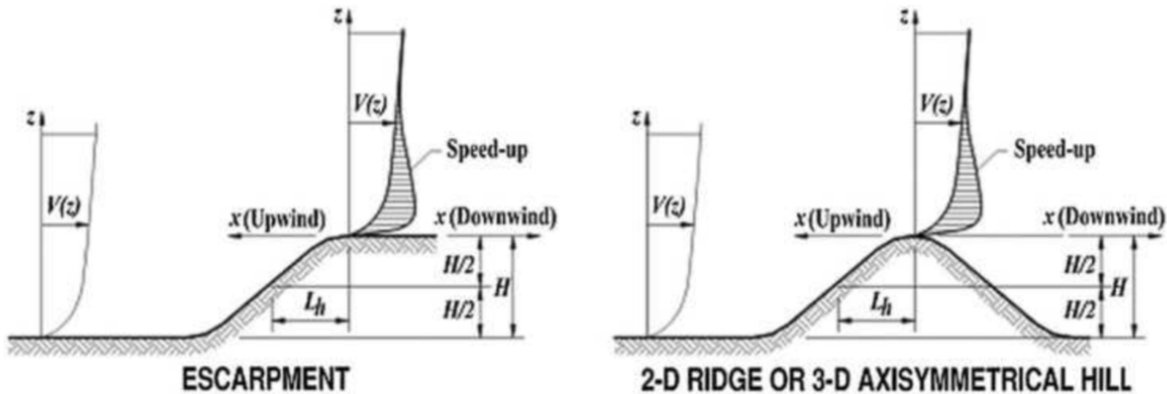


**Figure 3: (Topographical Factors, from ("Wind loads: General requirements," 2016))**

The section of guideway for which this solar racking is being designed is assumed to be on flat ground in an area with no escarpments, ridges, or hills. If the contrary is true, specific geographic dimensions of the feature would be needed to complete this calculation. With this assumption, $K_{zt} = 1$.

$K_d$ is the wind directionality factor

Table 26.6-1 Wind Directionality Factor, $K_d$

| Structure Type | Directionality Factor $K_d$ |
|---|---|
| **Buildings** | |
| Main Wind Force Resisting System | 0.85 |
| Components and Cladding | 0.85 |
| **Arched Roofs** | 0.85 |
| **Circular Domes** | $1.0^a$ |
| **Chimneys, Tanks, and Similar Structures** | |
| Square | 0.90 |
| Hexagonal | 0.95 |
| Octagonal | $1.0^a$ |
| Round | $1.0^a$ |
| **Solid Freestanding Walls, Roof Top Equipment, and Solid Freestanding and Attached Signs** | 0.85 |
| **Open Signs and Single-Plane Open Frames** | 0.85 |
| **Trussed Towers** | |
| Triangular, square, or rectangular | 0.85 |
| All other cross sections | 0.95 |

[a]Directionality factor $K_d = 0.95$ shall be permitted for round or octagonal structures with nonaxisymmetric structural systems.

**Figure 4: (Wind Directionality Factor, from ("Wind loads: General requirements," 2016))**

The best approximation of the canopy's profile is an arched roof. Therefore $K_d = 0.85$.

_I is the importance factor_

$I$ is taken as 1 for this application since a transportation system is not an emergency facility such as a hospital, fire department, etc. $I = 1$

Using these values the velocity pressure $q$ is calculated as:

$$q = 0.00256(K_z)(K_{zt})(K_d)(V^2)(I)$$

$$q = 0.00256(0.649)(1.0)(0.85)(103^2)(1)$$

$$q = 14.98psf = 717.4 \ \frac{N}{m^2}$$

3. **Using the resulting value for the velocity pressure $q$, the design wind pressure is determined using Equation 3:**
$$p = q_h GC_{rn} \qquad (3)$$

Where the net pressure coefficient is given by Equation 4:

$$GC_{rn} = (\gamma_p)(\gamma_c)(\gamma_e)(GC_{rn})_{nom} \qquad (4)$$

Where

$\gamma_p = \min{(1.2, 0.9 + \frac{h_{pt}}{h})}$
$\gamma_c = \max{(0.6 + 0.06L_p, 0.8)}$
$\gamma_e = 1.5$ uplift loads on panels that are exposed and within a distance of $1.5(L_p)$ from an end row at an exposed edge of the array
$(GC_{rn})_{nom}$ = nominal net pressure coefficient for rooftop solar panels determined from Fig. 5 below.

Definitions (illustrated in Figure 5 below):

$h$: mean roof height of building or other structure
$h_1$: height of solar panel above roof at lower edge of panel
$h_2$: height of solar panel above roof at upper edge of panel
$h_{pt}$: mean parapet height above adjacent roof surface
$L_p$: panel chord length

Geometrical assumptions made to proceed with the calculation for the Superway's canopy:

$h = z$ = elevation of upper surface of guideway = 23.28ft
$h_1$ = height of lowest edge of panel at lower end of array slope
$h_2$ = height of highest edge of panel at upper end of array slope
$h_{pt}$ = mean height of racking above guideway surface = $\frac{42.5" + 0"}{2}$ = 21.25" = 1.77$ft$
$L_p$ = commercial panel width = 39" = 3.25$ft$
$\gamma_e$ = 1.5 for all panels in the array

Using the definitions of $\gamma_p$, $\gamma_c$, and $\gamma_e$ above with the respective variables values substituted in:

$\gamma_p$ = 0.976
$\gamma_c$ = 0.8
$\gamma_e$ = 1.5

For $(GC_{rn})_{nom}$:

Location 3 at the edge was selected in the Building Roof Plan in Figure 5 (indicated by red arrow) to mimic the exposed conditions of the Superway's array and to design for maximal pressures that account for turbulence from flow separation.

The plot of Normalized Wind Area vs. Nominal Net Pressure Coefficient on the right is used since the total slope of the array is approximately 15 degrees. The total normalized wind area of the 12 panel array is calculated as 253.5 $ft^2$. Using these values, the value of $(GC_{rn})_{nom}$ indicated by the red dot in Figure 5:
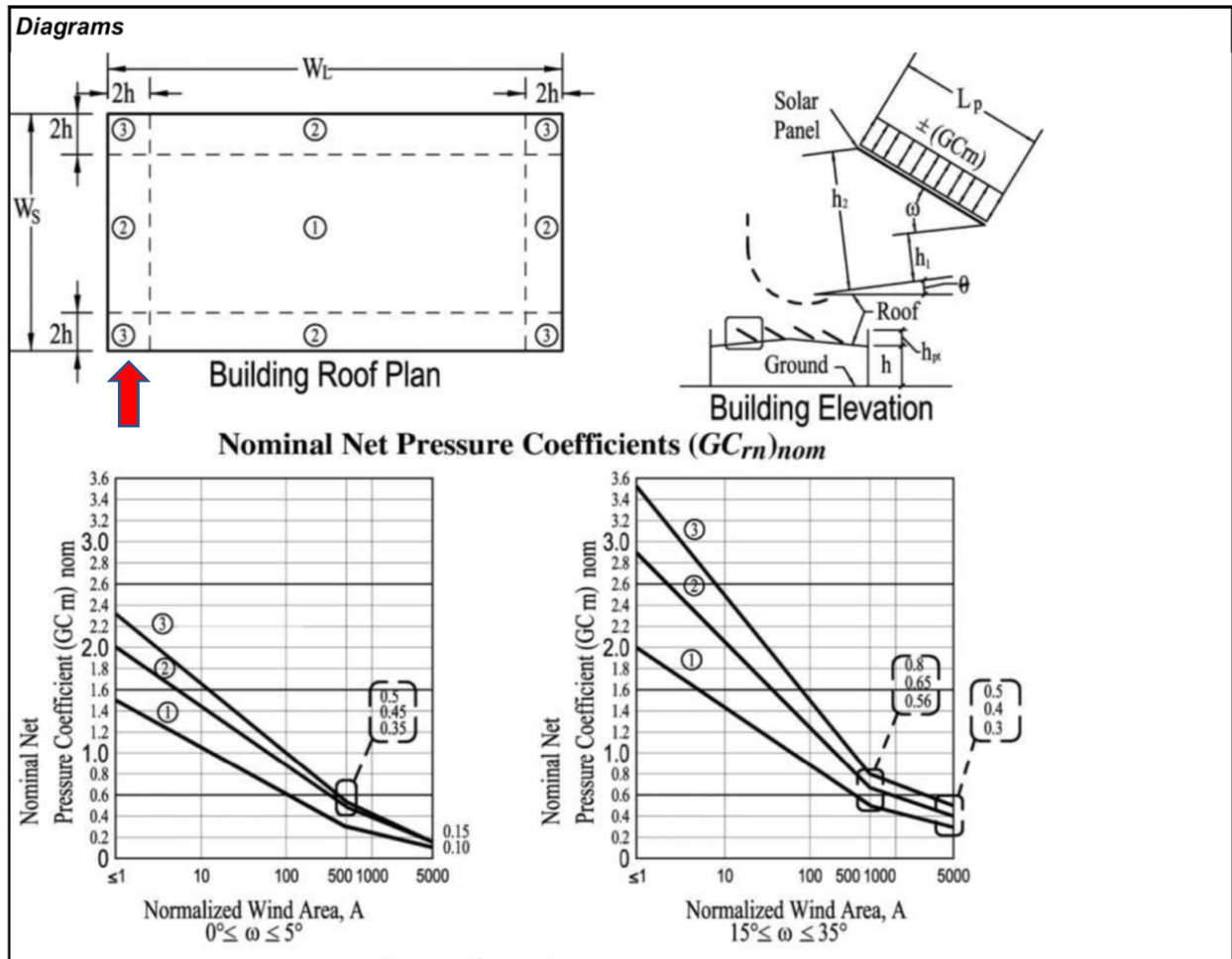
$$(GC_{rn})_{nom} \sim 1.4$$

**Figure 5: (Nominal Net Pressure Coefficient, from ("Wind loads: General requirements," 2016))**

Substituting these values to finally calculate $GC_{rn}$ using Equation 4:

$$GC_{rn} = (\gamma_p)(\gamma_c)(\gamma_e)(GC_{rn})_{nom}$$
$$GC_{rn} = (0.976)(0.8)(1.5)(1.4)$$
$$GC_{rn} = 1.639$$

4. **Finally calculating the design pressure using Equation 3:**

$$p = q_h GC_{rn}$$
$$p = (14.98)(1.639)$$
$$p = 24.56 psf \ or \ 1,176 \frac{N}{m^2}$$

**Appendix B: Statics Calculation**

For the next step in analyzing the mounting structure, Messenger and Ventre state that with these wind loads, the equations of static equilibrium are used to compute the forces acting on the structural members (Messenger and Ventre, 2003). For the purposes of the subsequent static analysis, the worst case ASCE pressure of 55psf was applied instead of the value calculated in Appendix A to evaluate the design in accordance with common industry practice.

Using the 55psf as the worst case uplift pressure, the total load on the array is calculated using its total area:

$$Total\ Load = (55psf)(253.5ft^2)$$
$$Total\ Load = 13{,}942.5lb$$

Divided over the 12 panels, the uplift load on each panel is 1,161.9lb.
4 clamps are required for each panel; therefore the uplift resisted by each clamp is 290.5lb.
Each purlin has 4 clamps mounted to it, and the loads resisted by the clamps are approximated to be point loads on the purlins as shown in Figure 6:
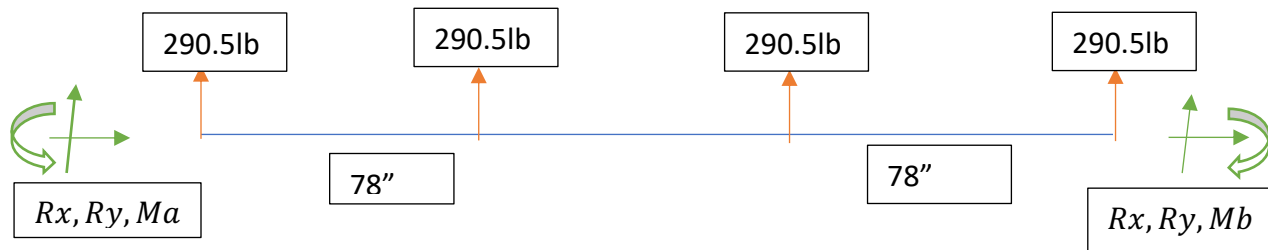


**Figure 6:** Uplift Loads on Purlin and Reactions at Ends. Uplift loads on the purlin from the clamps holding the panels are approximated as point loads.

Modeling the purlin as a simple fixed beam, the equations of static equilibrium were used to obtain the reaction forces and moments at the ends of the purlin at attachment points to the trussing as indicated by the green arrows in Figure 6.

$$\sum F_x = 0\ ; R_x = 0$$

$$\sum F_y = 0;\ R_y = -580.94lb$$

$$\sum M_A = 0;\ M_B = -11{,}037.82\ lb.ft$$
$$M_A = 11{,}037.82\ lb.ft$$

Next, the reactions at the ends of the purlin also act on the truss since they are attached together. The shape of the truss was simplified to a triangle. A side view of the truss and loads is shown in Figure 7 below. The assumptions of an ideal truss including that the weights of the members could be neglected, members are connected only at their ends, loads act at the joints, and members connected by frictionless pins so that only axial loads are transferred were assumed to hold.
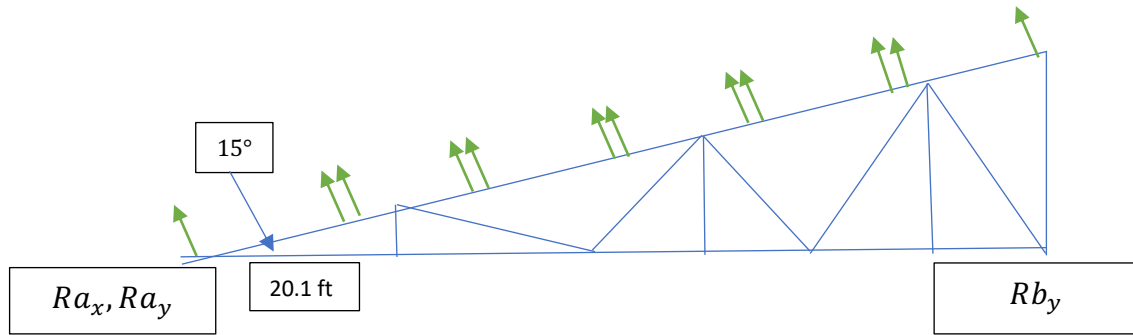


Figure 7: Loads on truss from purlin ends. Each green arrow represents $R_y = 580.94lb$ acting on the upper surface of the truss.

For calculation purposes, an ideal truss was assumed. Loads are assumed to act at the joints of an ideal truss, which support no moments since they are considered pinned joints (with only tensile or compressive forces). Therefore, the reactions were approximated as $2R_y$ applied at the joints of the truss. These forces were then broken into x and y components using trigonometric relationships. Next, the equations of static equilibrium are used again to determine the reactions at the ends of the base of the truss. A pinned fixture was assigned at point A and a roller fixture was assigned at point B to avoid a statically indeterminate truss:

$$\sum M_A = 0; \; Rb_y = -3,592 \; lb$$

$$\sum F_x = 0 \; ; \; Ra_x = -1,804lb$$

$$\sum F_y = 0; \; Ra_y - 3,142lb$$

Joint A of the truss was selected for analysis using the method of joints. Its two joints (blue arrows) are labeled AH and AI :
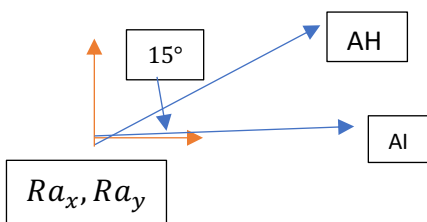
Using the equations of static equilibrium applied at this joint:

$$\Sigma F_y = 0; \ 12{,}141 lb = AH$$
$$\Sigma F_x = 0; \ -9{,}923 lb = AI$$

Next using the cross sectional dimensions of a member the normal stress is calculated for member AH:
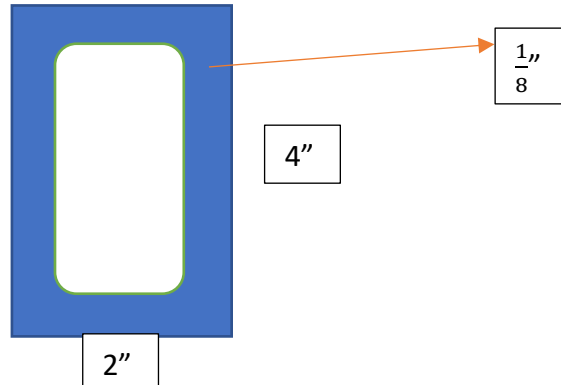


Figure 8: Dimensions of cross-sectional area of a member of the truss.

The equation for normal stress is Equation 5. Substituting the area of the region in blue and the resultant force in AH into Equation 5 converted to Newtons, the resulting value of stress in this member is:

$$\sigma = \frac{F}{A} \qquad (5)$$

$$A = 0.734375 in^2 = 0.00047379 \ m^2$$

$$\sigma = 1.14 \times 10^8 \ \frac{N}{m^2}$$

Since the second and current iteration of the racking's trussing is constructed using equal-leg steel angle members, the calculation above was redone with the modified cross sectional area as shown in Figure 9.
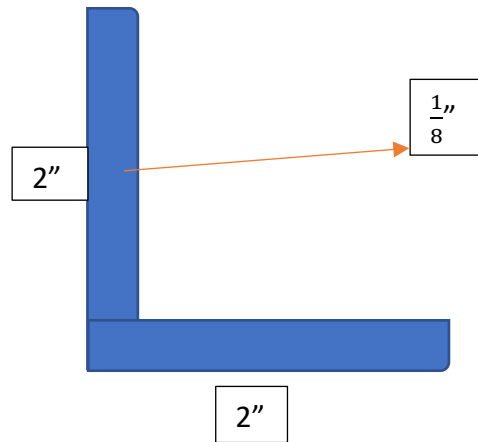


Figure 9: Dimensions of cross-sectional area of a member of the truss constructed of steel angle.

$$\sigma = \frac{F}{A} \qquad (5)$$

$$A = 0.484 in^2 = 0.0003123 \ m^2$$

$$\sigma = 1.73 \times 10^8 \ \frac{N}{m^2}$$

APPENDIX C & D: **Type out calculations in notebook** as mentioned on Page 13-15 of literature review! Change Labels As necessary for Appendix

**Appendix C: Plots of Reactions on the Guideway at Various Wind Speeds.**
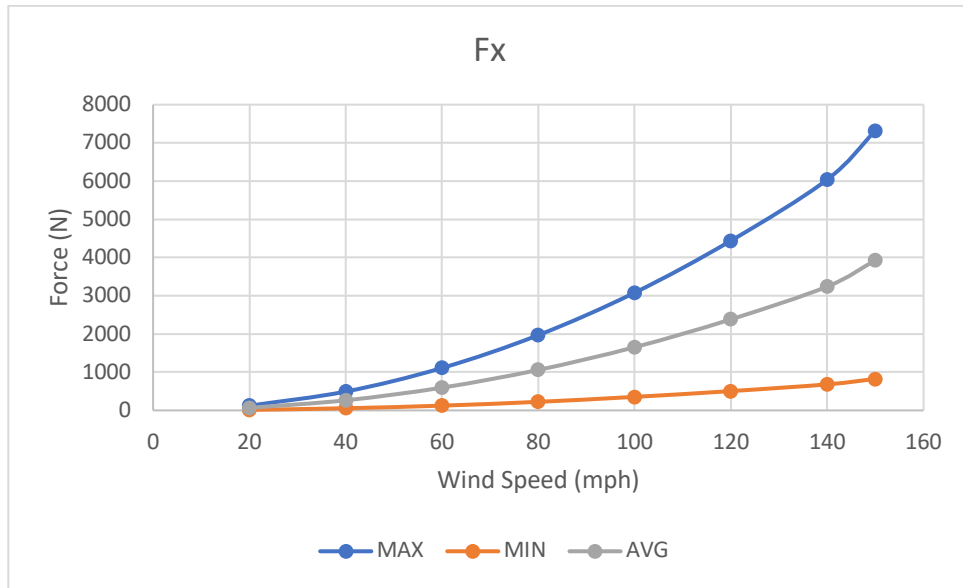


Figure 9: Plot of reactions in the x-direction on the brackets for increasing wind speed.
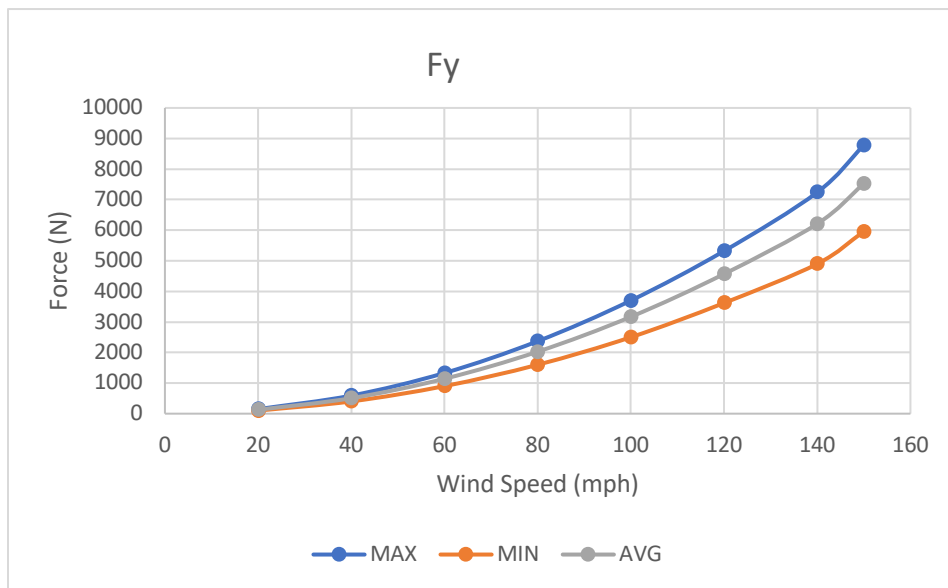


Figure 10: Plot of reactions in the y-direction on the brackets for increasing wind speed.
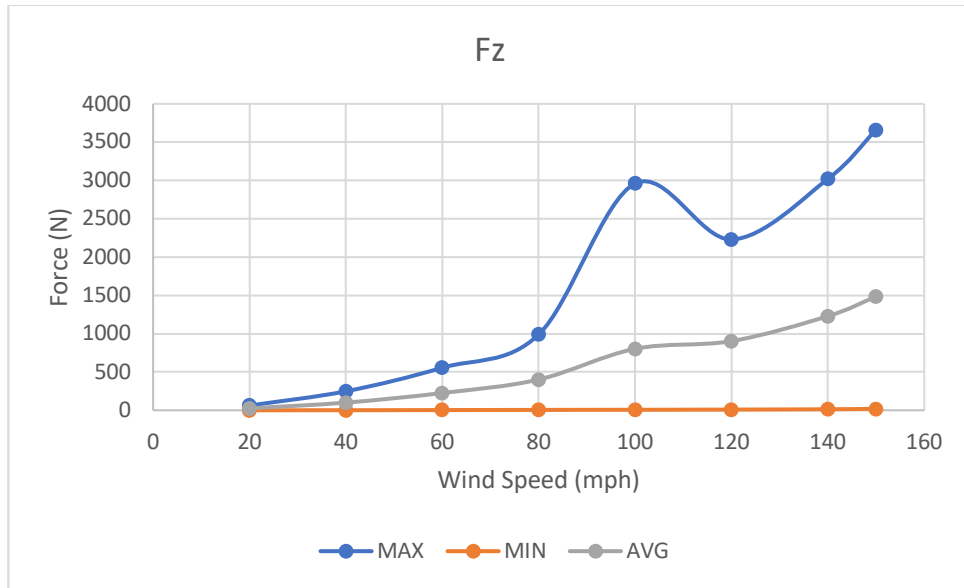
75

Figure 11: Plot of reactions in the z-direction on the brackets for increasing wind speed.
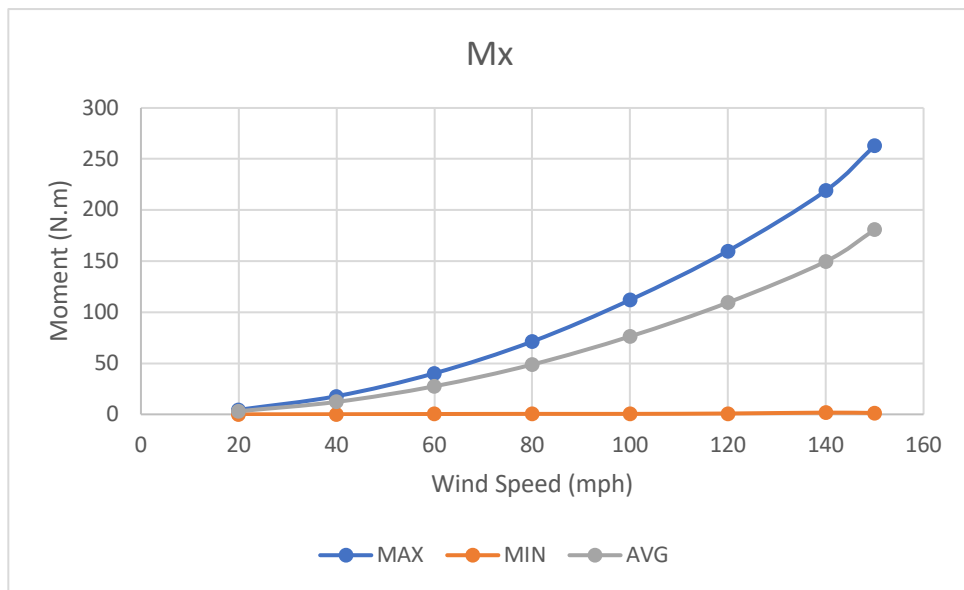


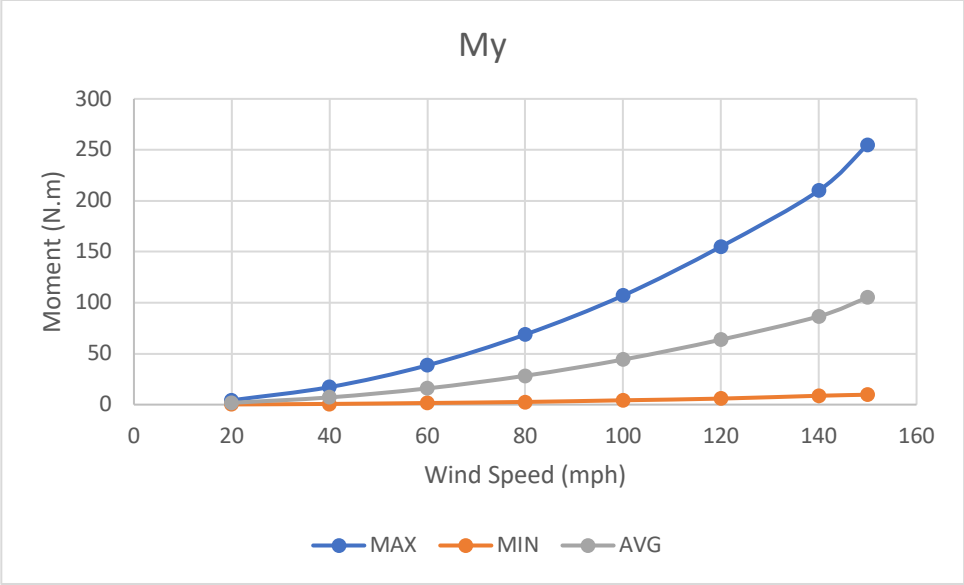Figure 12: Plot of reaction moments around the x-axis on the brackets for increasing wind speed.

Figure 13: Plot of reaction moments around the y-axis on the brackets for increasing wind speed.
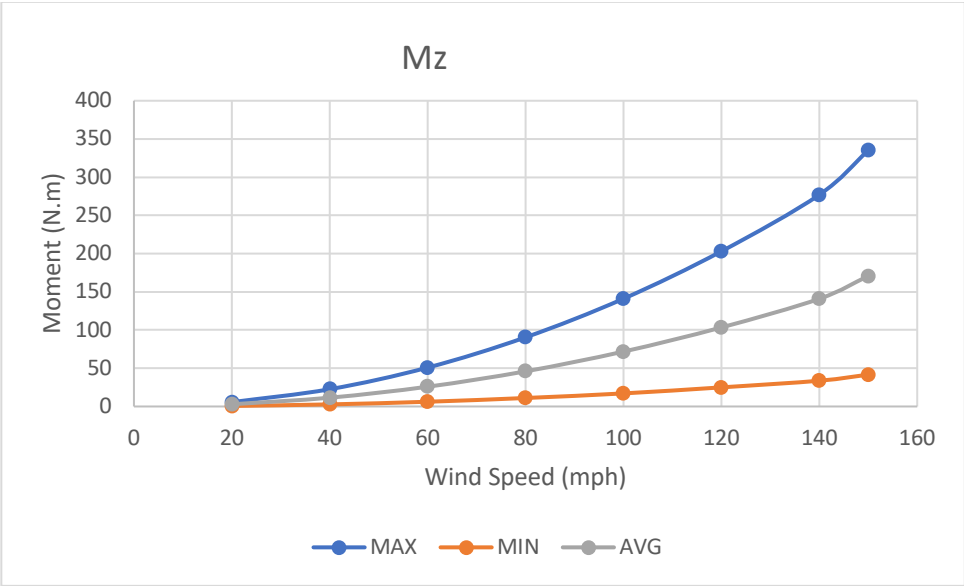


Figure 14: Plot of reaction moments around the z-axis on the brackets for increasing wind speed.

# Appendix D. Additional Convergence Plots for Stress and Displacement for the Uplift and Compression Wind Loading Studies with the Global Convergence Criterion Defined for Strain Energy Change
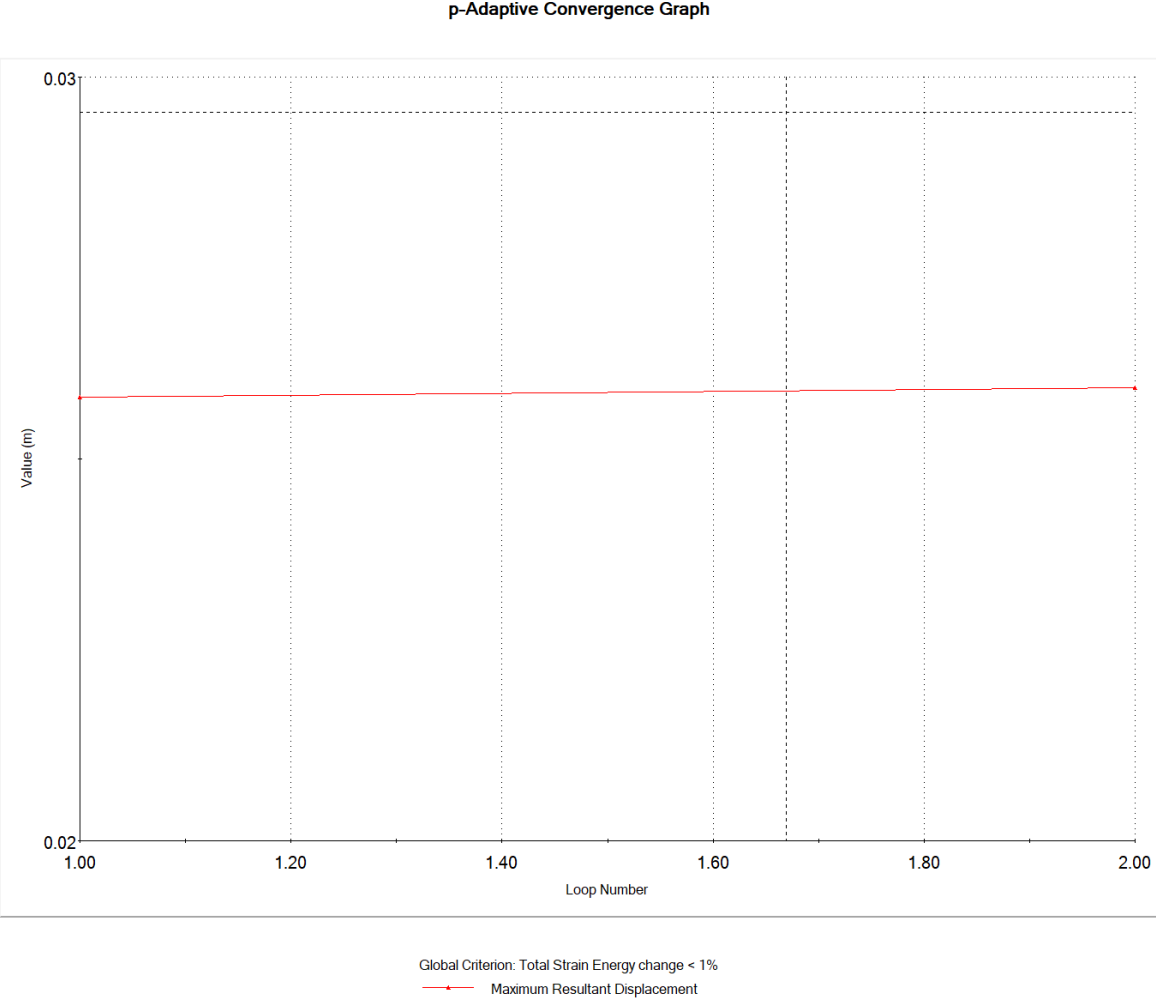
**55psf Uplift**



**Figure XX. Displacement Convergence Plot for the 55psf Uplift Loading Case.** The plot shows the change in displacement for each loop conducted using the p-adaptive simulation study in Solidworks defined to run until a total strain energy change of less than 1% was achieved.

**p-Adaptive Convergence Graph**
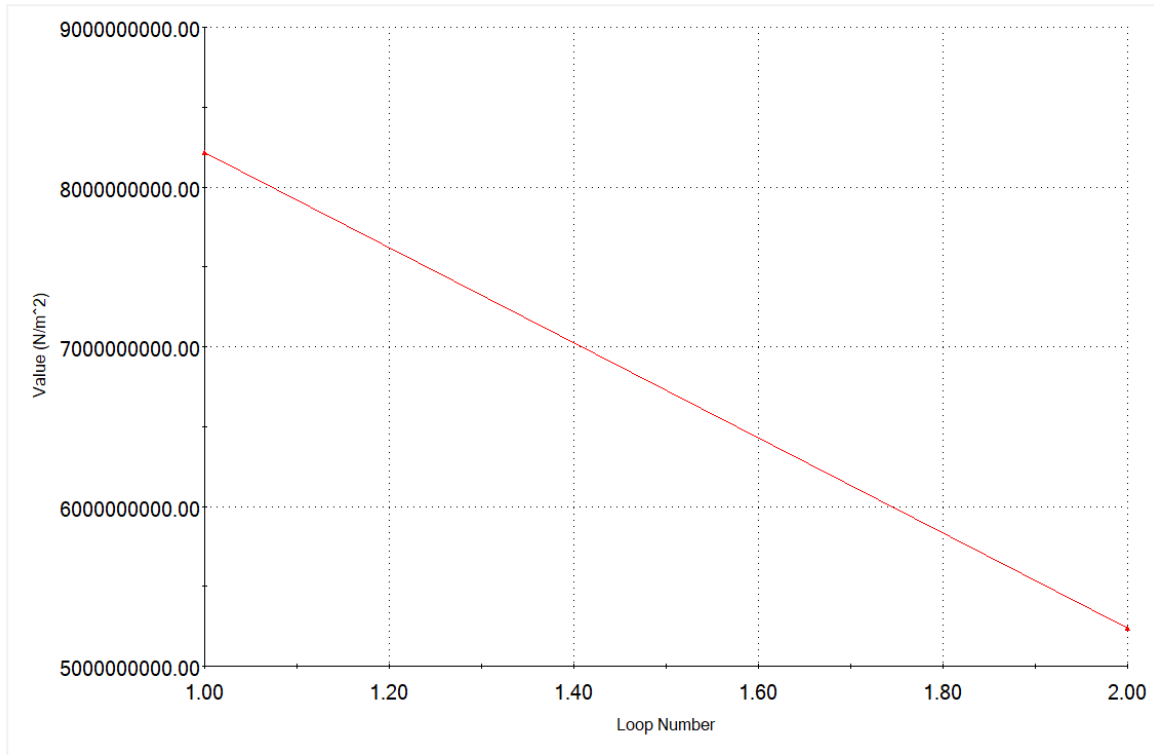


Global Criterion: Total Strain Energy change < 1%
— Maximum von Mises Stress

1.53233, 9.2023e+09

**Figure XX. Von Mises Stress Convergence Plot for the 55psf Uplift Loading Case.** The plot shows the change in stress for each loop conducted using the p-adaptive simulation study in Solidworks defined to run unti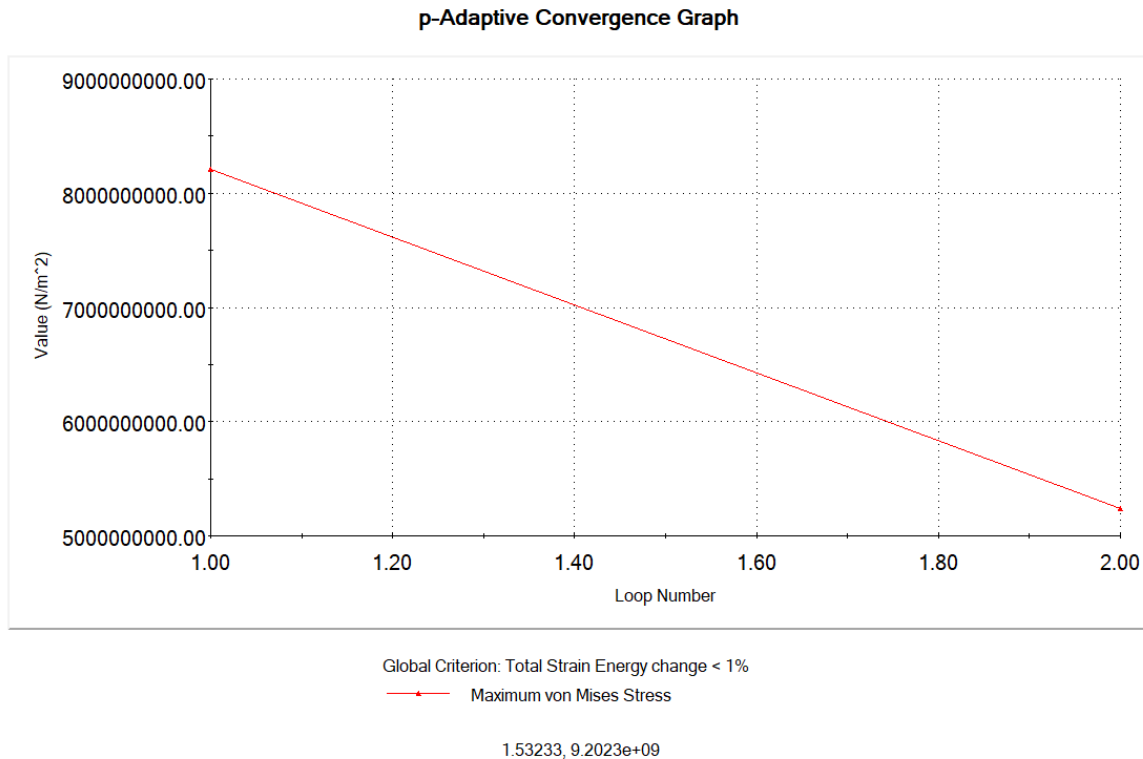l a total strain energy change of less than 1% was achieved (strain energy vs. Loop number plots are included Section 6.1.3).

**55psf Compression**



Figure XX. Displacement Convergence Plot for the 55psf Compression Loading Case. The plot shows the change in displacement for each loop conducted using the p-adaptive simulation study in Solidworks defined to run until a total strain energy change of less than 1% was achieved.
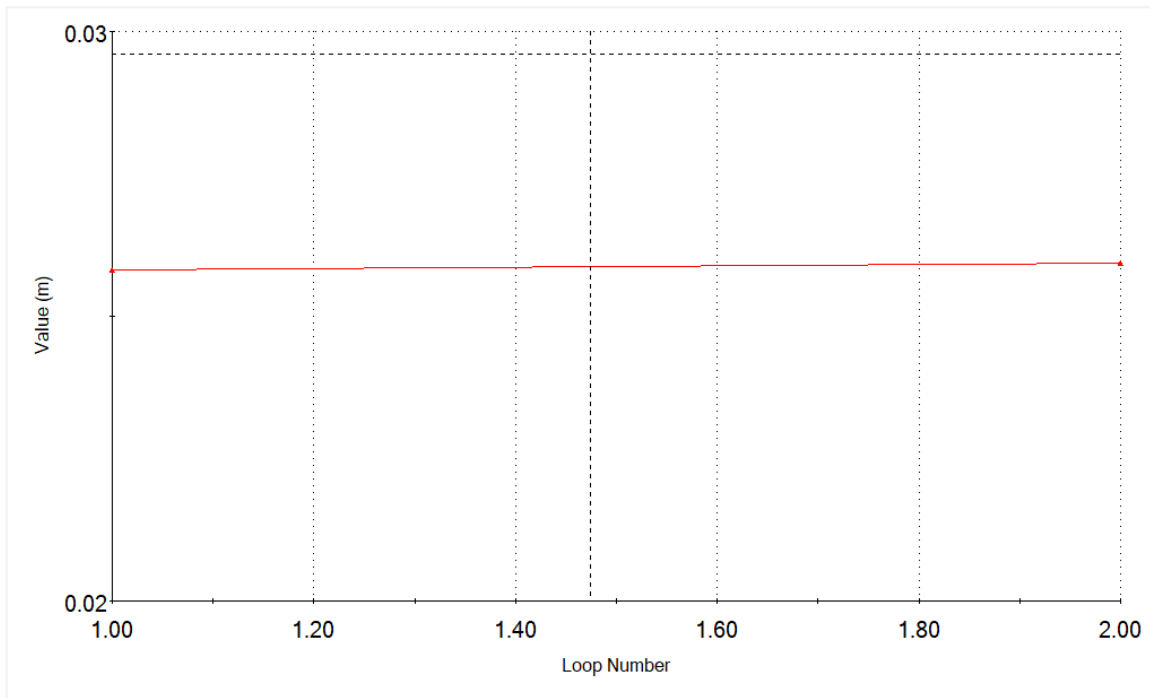
**Figure XX. Von Mises Stress Convergence Plot for the 55psf Compression Loading Case.**
The plot shows the change in stress for each loop conducted using the p-adaptive simulation study in Solidworks defined to run until a total strain energy change of less than 1% was achieved.

**Appendix E: Stress, Displacement, and Factor of Safety Contours for Wind Loading Simulations**
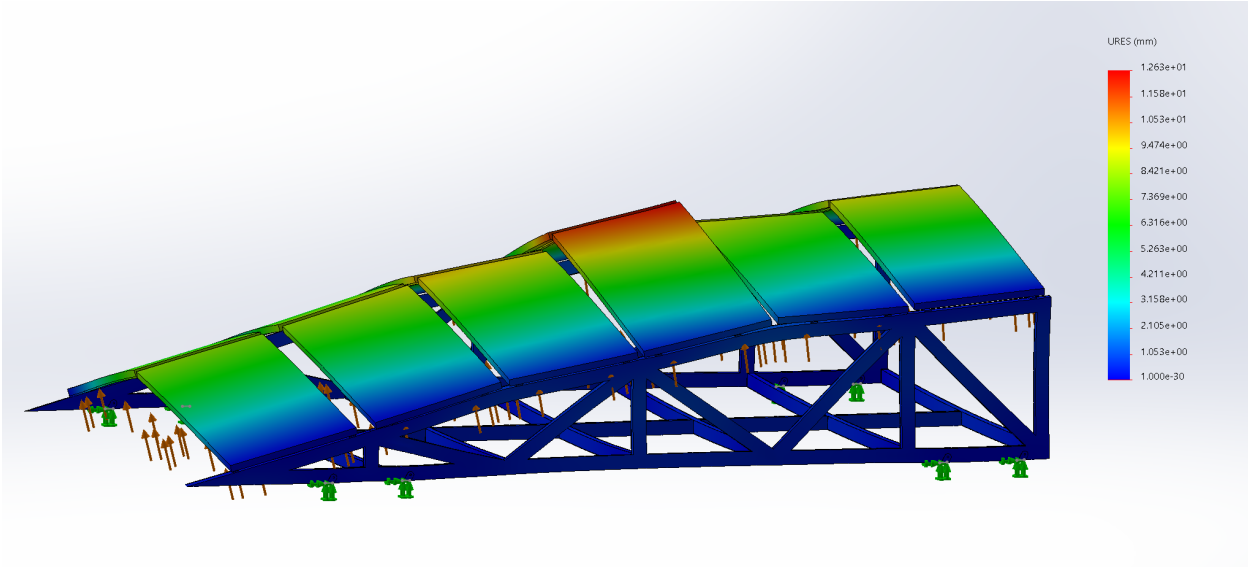


Figure 9. Displacement Contour for the HSS Racking for the critical 55psf loading case. A maximum displacement of 12mm occurs at the middle of the central purlin.
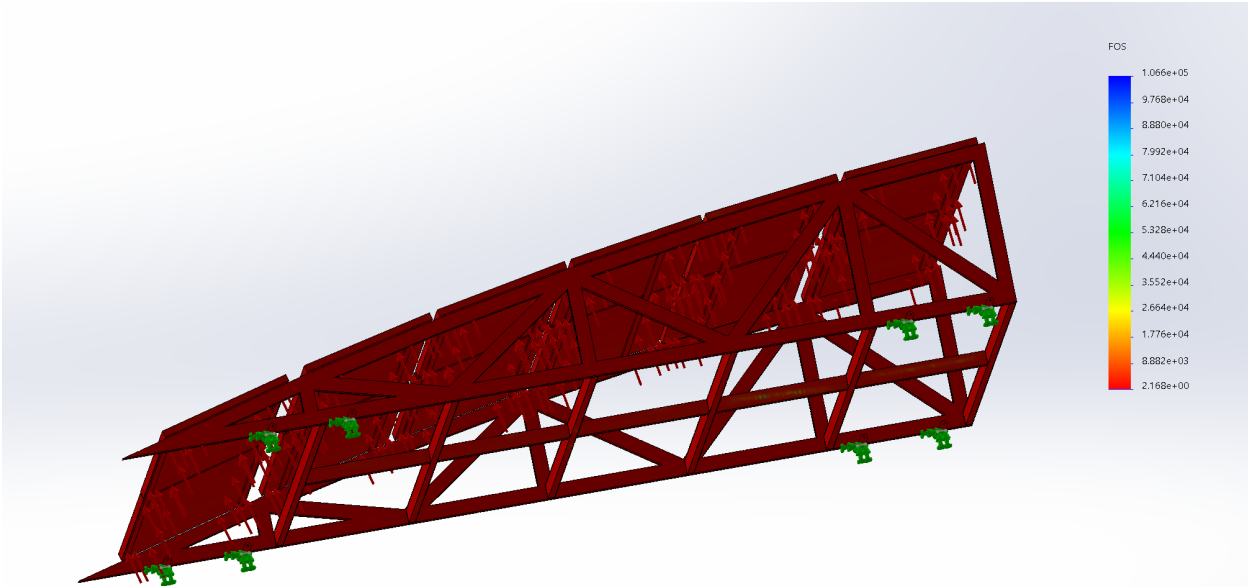


Figure 10. Contour of factor of safety against yield for the HSS model. All components meet a factor of safety of 2 for the critical 55psf loading case.

**Figure XX. Overall Stresses and Displacements for the Steel Angle Model under 55psf Uplift loading case.** A general view of the stress distribution is shown in the top figure and the corresponding displacement contour is shown in the bottom figure. Maximum displacements occur at the middle of the simplified Z-purlin.
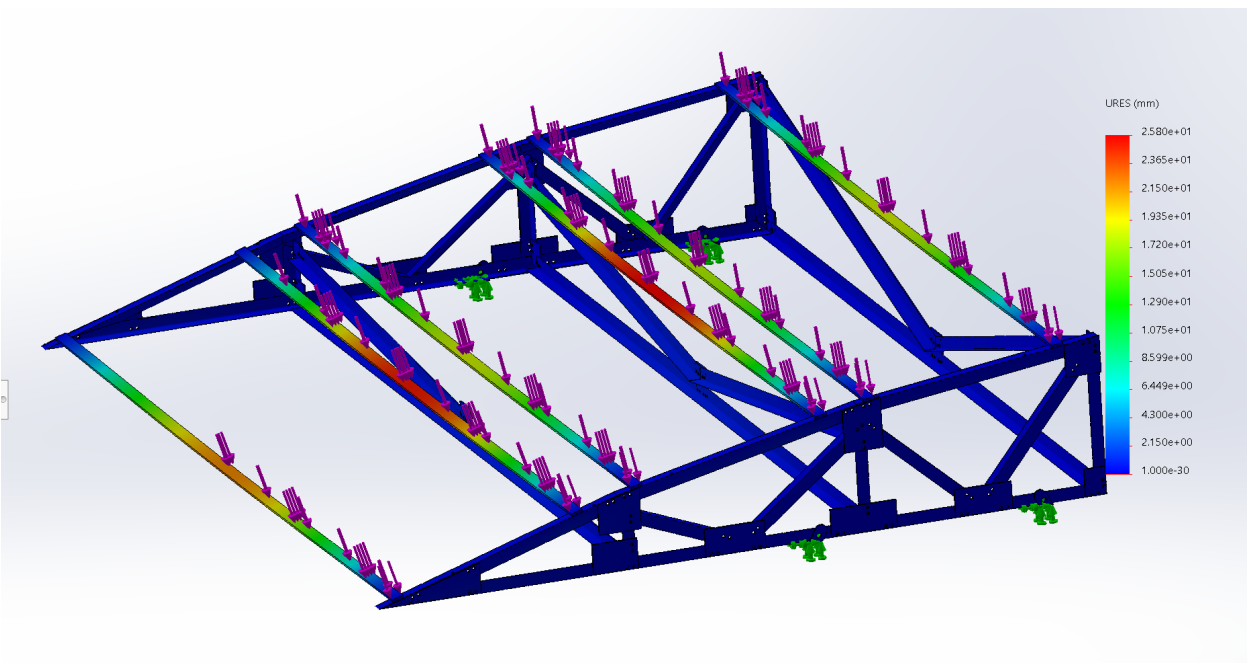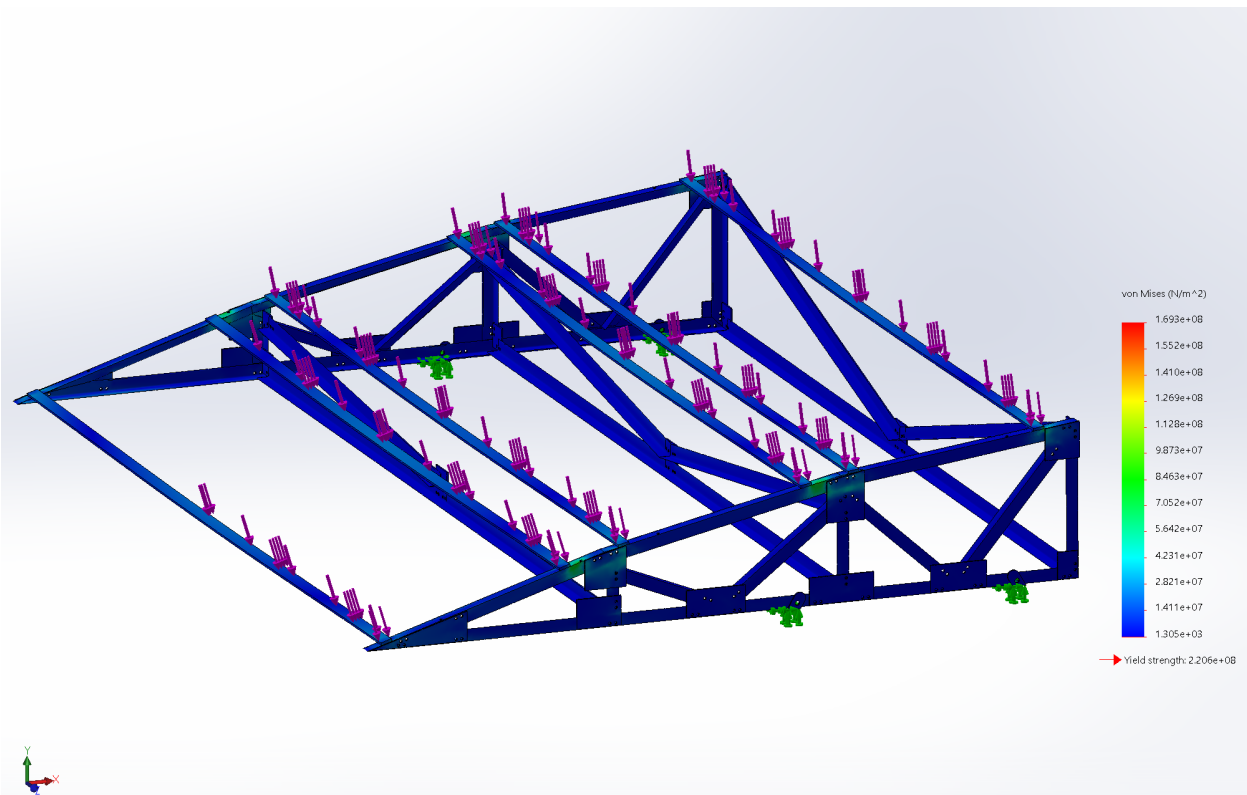
**Figure XX. Overall Stresses and Displacements for the Steel Angle Model under 55psf Compression loading case.** A general view of the stress distribution is shown in the top figure and the corresponding displacement contour is shown in the bottom figure.

**Appendix F: Seismic Simulation Contours**



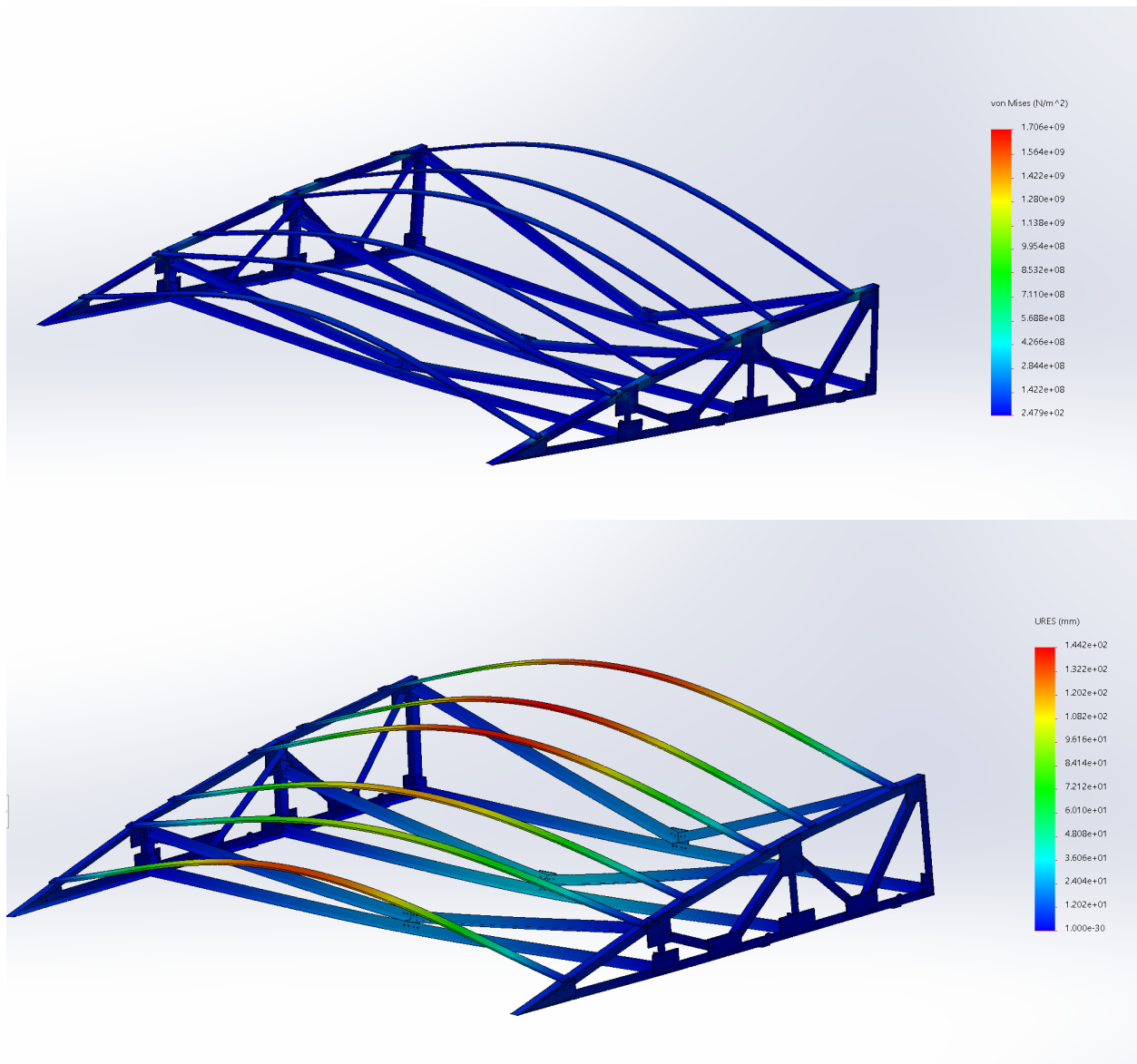**Figure XX. General Stress Distribution on Model with Excitation Defined in the X-direction.** A view of the resultant stress distribution in the model for excitation in the X-direction with the response spectrum for the magnitude 6.9 El Centro earthquake. Stress concentrations appear at the connection points and are in the $10^6$ order of magnitude.

**Figure XX. Displacement Distribution with Excitation Defined in the X-direction.** A view of the resultant displacement distribution in the model for excitation in the X-direction with the response spectrum for the magnitude 6.9 El Centro earthquake. Maximum displacements occur at the middle of the Z-purlin of $8.069 * 10^{-1} mm$.
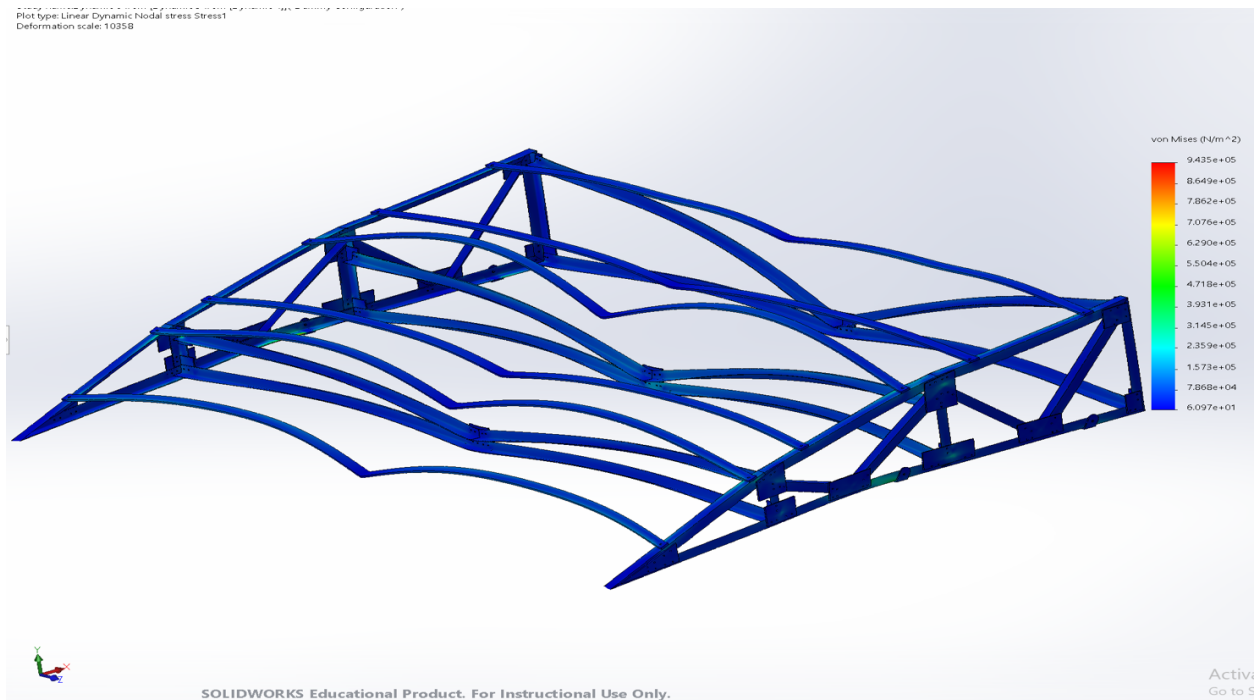
86

**Figure XX. General Stress Distribution on Model with Excitation Defined in the Z-direction.** A view of the resultant stress distribution in the model for excitation in the Z-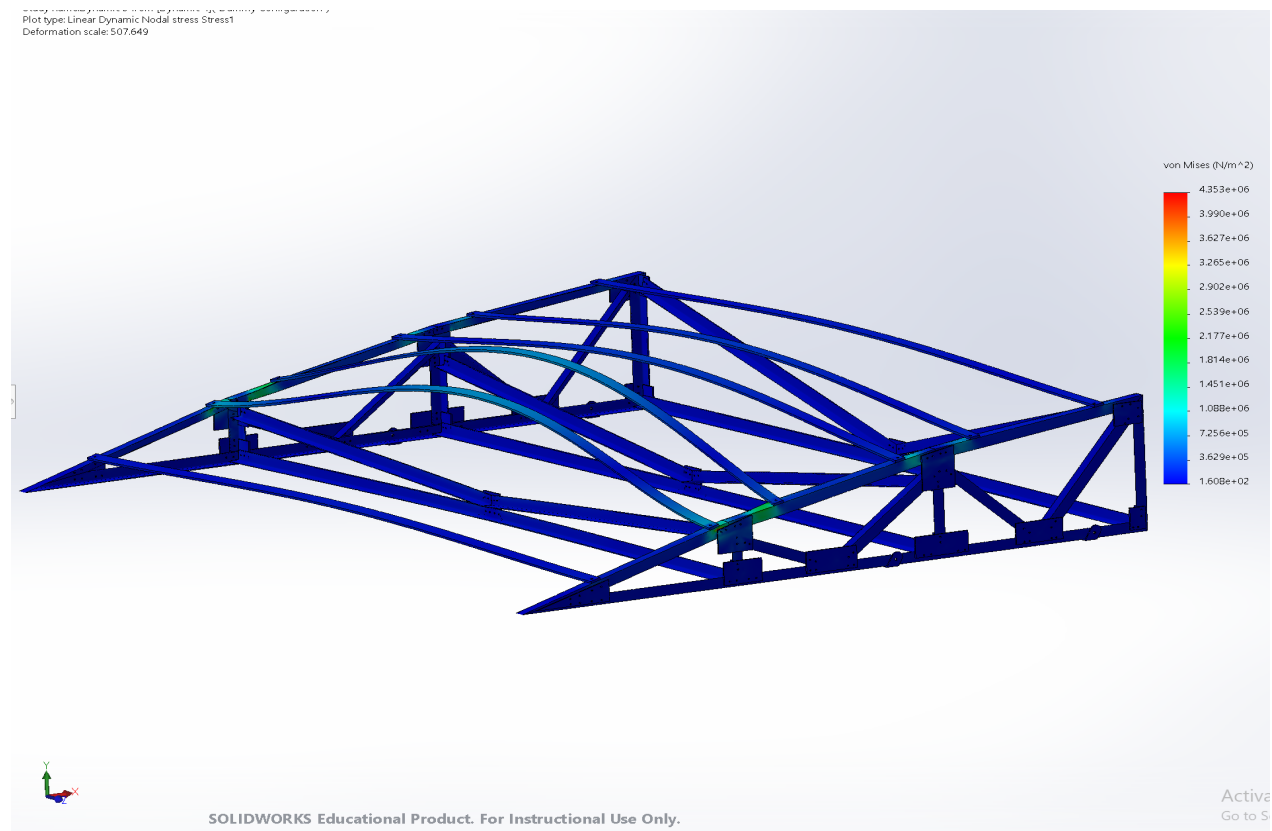direction with the response spectrum for the magnitude 6.9 El Centro earthquake. Stress concentrations appear at the connection points and are in the $10^5$ order of magnitude.
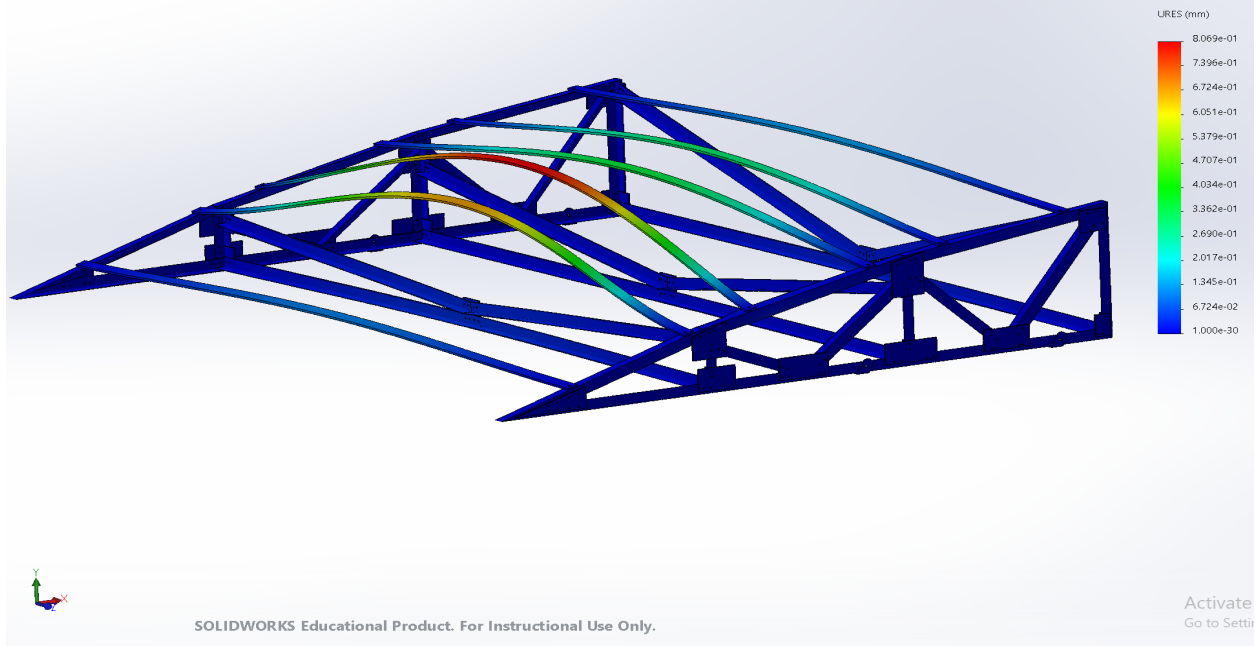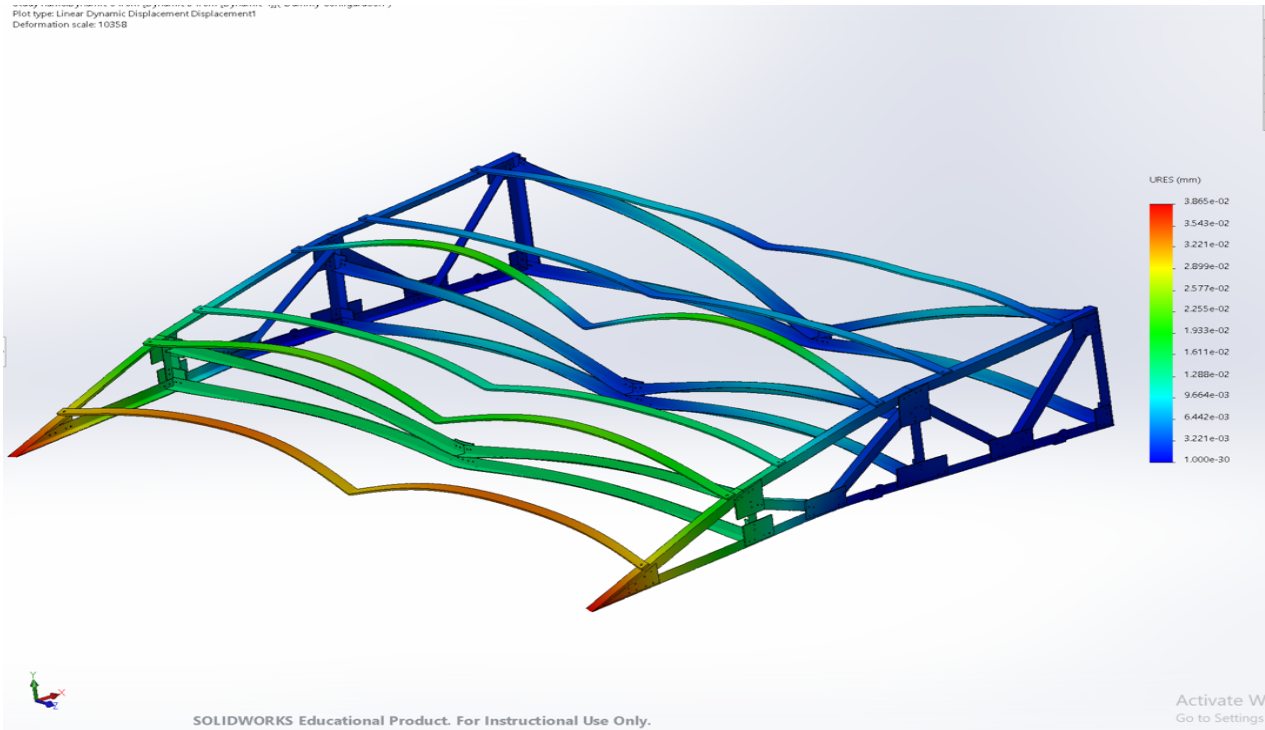


**Figure XX. Displacement Distribution with Excitation Defined in the Z-direction.** A view of the resultant stress distribution in the model for excitation in the Z-direction with the response spectrum for the magnitude 6.9 El Centro earthquake. Maximum displacements occur at the middle of the Z-purlin of $2.9 * 10^{-2} \, mm$.

**Appendix G. Calculations for Minimum Bolt Size and Plate Thickness**

Following the procedure defined by the Steel Institute for Bolted Connections with geometrical approximations made between analogous structures from the diagrams provided and the racking design, values for the minimum plate thickness and bolt size were determined.
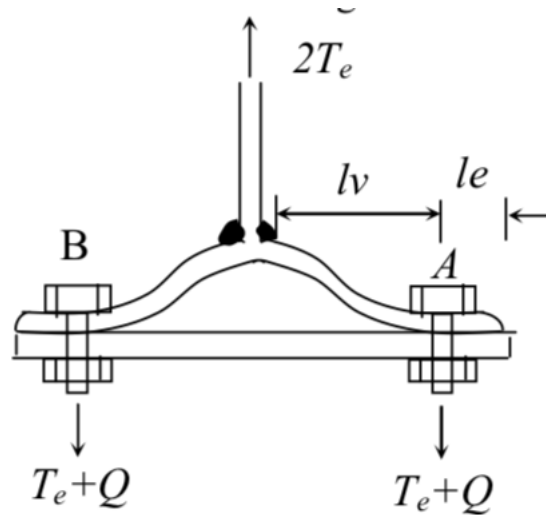


Figure XX. Diagram of physical parameters used to determine the requirements of a bolted connection based on a procedure specified by the Steel Institute.

$T_e$ = External tensile force acting on racking
$l_v$ = distance from centerline of bolt to where $T_e$ acts
$M_p$ = plastic moment capacity of the plate
$f_y = \beta * T_e$ (where $\beta = 2$ for pre-loaded bolt)
$w$ = effective width between flanges of each pair of bolts
$l_e$ = the distance from the centerline of a bolt to the end of a plate

$$M_p = \frac{T_e * l_v}{2}$$

$T_e = 581lb$ obtained from the statics calculation in Appendix B for the reaction from the purlins onto the side trusses in the Y-direction.

$l_v = 6.1$in obtained from the model; the maximum distance from the center of a bolt hole on the side truss to the attachment point of a Z-purlin on the upper chord of the truss.

The resulting value for $M_p$ is
$M_p = 1,772$ lb.

The minimum thickness for the plate is calculated using the formula

$$t_{min} = \sqrt{\frac{1.1 * 4 * M_p}{f_y * w}}$$

$w = 6$in to be conservative; determined based on the minimum of all dimensional distances between each pair of flanges on each member of the side trussing; the shortest value was used since this would lead to a higher required value for $t_{min}$

The resulting value for $t_{min}$ is 0.33in. Since the largest standard size of thickness of steel plate available from various manufacturers is 0.25in, this dimension was used in the model of the gusset plates instead of the calculated value.

The tension in the bolt cannot exceed its tensile capacity. The total tension in the bolt is taken as the sum of $T_e$ as defined above and Q, the prying force.

$$Q = \frac{M_p}{l_e}$$

$l_e = 1.6in$ corresponding to minimum distance from a hole to the end of a plate in the model at the lower pointed edge of the canopy

$Q = 1,108lb$

Therefore the tensile capacity of the selected bolt needs to exceed $T_e + Q$,

$T_e + Q = 581 + 1,108 = 1,690lb$

The prescribed factor of safety for bolts is 8.5

$8.5 * 1,690lb = 14,365lb$

Therefore, the required tensile strength of the selected bolt needs to be $14,365lb$.

Next, to select a bolt that will not require holes that will takeover the 2" by 2" dimension of the steel angle member but meet the required load requirement, Grade 10.9 M12 bolts are selected from the chart on bolt tensile strengths below:

| Thread d (mm) | Pitch P (mm) (in) | Nominal Stress Area A~s,nom~ (mm²) (in2) | Property Class | | | | | | | | |
|---|---|---|---|---|---|---|---|---|---|---|---|
| | | | 4.6 | 4.8 | 5.6 | 5.8 | 6.8 | 8.8 | 9.8 | 10.9 | 12.9 |
| | | | Minimum Ultimate Tensile Load - F~m,min~ (N) (kgf, lbf) | | | | | | | | |
| M3 | 0.50 | 5.03 | 2010 | 2110 | 2510 | 2620 | 3020 | 4020 | 4530 | 5230 | 6140 |
| M3.5 | 0.60 | 6.78 | 2710 | 2850 | 3390 | 3530 | 4070 | 5420 | 6100 | 7050 | 8270 |
| M4 | 0.70 | 8.78 | 3510 | 3690 | 4390 | 4570 | 5270 | 7020 | 7900 | 9130 | 10700 |
| M5 | 0.80 | 14.2 | 5680 | 5960 | 7100 | 7380 | 8520 | 11350 | 12800 | 14800 | 17300 |
| M6 | 1.00 | 20.1 | 8040 | 8440 | 10000 | 10400 | 12100 | 16100 | 18100 | 20900 | 24500 |
| M7 | 1.00 | 28.9 | 11600 | 12100 | 14400 | 15000 | 17300 | 23100 | 26000 | 30100 | 35300 |
| M8 | 1.25 | 36.6 | 14600 | 15400 | 18300 | 19000 | 22000 | 29200 | 32900 | 38100 | 44600 |
| M10 | 1.50 | 58.0 | 23200 | 24400 | 29000 | 30200 | 34800 | 46400 | 52200 | 60300 | 70800 |
| M12 | 1.75 | 84.3 | 33700 | 35400 | 42200 | 43800 | 50600 | 67400[d] | 75200 | 87700 | 103000 |
| M14 | 2.00 | 115 | 46000 | 48300 | 57500 | 59800 | 69000 | 92000[d] | 104000 | 120000 | 140000 |
| M16 | 2.00 | 157 | 62800 | 65900 | 78500 | 81600 | 94000 | 125000[d] | 141000 | 163000 | 192000 |
| M18 | 2.50 | 192 | 76800 | 80600 | 96000 | 99800 | 115000 | 159000 | | 200000 | 234000 |
| M20 | 2.50 | 245 | 98000 | 103000 | 122000 | 127000 | 147000 | 203000 | | 250000 | 299000 |
| M22 | 2.50 | 303 | 121000 | 127000 | 152000 | 158000 | 182000 | 252000 | | 315000 | 370000 |
| M24 | 3.00 | 353 | 141000 | 148000 | 176000 | 184000 | 212000 | 293000 | | 367000 | 431000 |
| M27 | 3.00 | 459 | 184000 | 193000 | 230000 | 239000 | 275000 | 381000 | | 477000 | 560000 |
| M30 | 3.50 | 561 | 224000 | 236000 | 280000 | 292000 | 337000 | 466000 | | 583000 | 684000 |
| M33 | 3.50 | 694 | 278000 | 292000 | 347000 | 361000 | 416000 | 576000 | | 722000 | 847000 |
| M36 | 4.00 | 817 | 327000 | 343000 | 408000 | 425000 | 490000 | 678000 | | 850000 | 997000 |
| M39 | 4.00 | 976 | 390000 | 410000 | 488000 | 508000 | 586000 | 810000 | | 1020000 | 1200000 |

Converted to pounds the tensile strength of a Grade 10.9 M12 bolt is

$$87.7 \ kN * 224.8085 = 19{,}715 lb$$

Therefore, this bolt conservatively satisfies the strength required for the hardware at the connections between the various members of the racking.

**Appendix H. Calculations to Determine the Minimum Spacing between Bolts and Minimum Required Space from the Edge of the Steel Angle Members**


Make sure to Reference *Specification for the Design of Light Gage Cold-Formed Steel Structures*

Spacing (distance) between bolts and distance from the center of any bolt to the end or boundary of connecting member shall not be less than $1\frac{1}{2}d$ or $\frac{P}{f_b t}$...

The required spacing between bolts and the distance from the center of a bolt to the end of a member were determined using the following methodology from *Specification for the Design of Light Gage Cold-Formed Steel Structures.*

The spacing (distance) between bolts and the distance from the center of any bolt to the end of boundary of a connecting member shall not be *less* than $1\frac{1}{2}d$ or $\frac{P}{f_b t}$

Where

d = diameter of bolt, in inches
P = force transmitted by bolt, lb
t = thickness of thinnest connected sheet, in
$f_b$ = basic design stress, psi

- Since M12 bolts were sized for this application in Appendix G above, d = 12mm or 0.472in.
- P is assigned a value of 581lb using the calculated vertical reaction force from a purlin onto the trussing from <mark>Appendix B</mark>
- t is assigned a value of 0.125in or 0.104ft, which is the thickness of the steel angle members and less than the thickness of the gusset plates
- $f_b$ is calculated using the formula for stress $\frac{F}{A} = \sigma$
  - A is taken as the cross-sectional area of a steel angle member: $0.0035\ ft^2$ using the calculated value from Appendix B
  - F is assigned a value of 581lb.
  - The calculated value for stress is therefore $\sigma = \frac{581lb}{0.0035ft^2} = f_b = 166,000psf$


The resultant values for $1\frac{1}{2}d$ or $\frac{P}{f_b t}$ are


$$\frac{P}{f_b t} = \frac{581lb}{166,000\ (0.104ft)} = 0.033ft\ or\ 0.396in$$


$$1\frac{1}{2}d = 0.71in$$

The minimum spacing between the bolts and between a bolt and the edge of a member then becomes the greater of $1\frac{1}{2}d$ and $\frac{P}{f_b t}$, which in this case is 0.71in. Therefore values greater than 0.71in are considered usable. To stay conservative in the actual design, facilitate ease of dimensioning, and to facilitate manufacturability, adjacent bolt holes were spaced at 1in the model and all bolt holes closer to the edge of a member were placed at a distance of 0.95in from the edge.

## Appendix I. Chart Specifying the Preload Values for Grade 10.9 M12 Bolts

As recommended in the simulation guide written by Reuss, the maximum preload value specified for a bolt should be chosen to prevent joint separation due to overload conditions, shear, and thread loosening.

| Thread | Coefficient Friction | Preload (N) Property class to ISO 898/1 | | | Tightening Torque (Nm)Property Class | | |
|---|---|---|---|---|---|---|---|
| | | 8.8 | 10.9 | 12.9 | 8.8 | 10.9 | 12.9 |
| M8 x 1 | 0.100 | 19500 | 27500 | 33000 | 22 | 30 | 36 |
| | 0.125 | 18600 | 26200 | 31500 | 25 | 35 | 42 |
| | 0.140 | 18100 | 25500 | 30600 | 27 | 38 | 45 |
| M10 x 1.25 | 0.100 | 30500 | 42900 | 51500 | 42 | 59 | 71 |
| | 0.125 | 29110 | 40900 | 49100 | 49 | 68 | 82 |
| | 0.140 | 28300 | 39800 | 47700 | 52 | 73 | 88 |
| M12 x 1.25 | 0.100 | 46600 | 65500 | 78500 | 76 | 105 | 130 |
| | 0.125 | 44600 | 62500 | 75000 | 88 | 125 | 150 |
| | 0.140 | 43300 | 6100 | 7300 | 95 | 135 | 160 |